On the

Fatigue Analysis of Wind Turbines

Herbert J. Sutherland
Sandia National Laboratories
Albuquerque, New Mexico 87185-0708

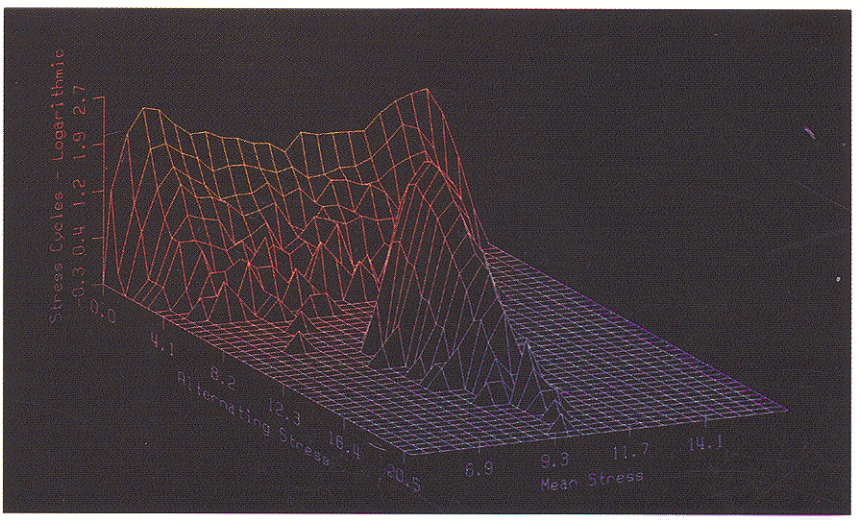

Prepared by
Sandia National Laboratories
Albuquerque, New Mexico 87185 and Livermore, California 94550

Sandia is a multiprogram laboratory operated by Sandia Corporation, a Lockheed Martin Company, for the United States Department of Energy under contract DE-AC04-94AL85000.

Approved for public release; further dissemination unlimited.

SAND99-0089
Unlimited Release
Printed June 1999

Sandia National Laboratories

Issued by Sandia National Laboratories, operated for the United States Department of Energy by Sandia Corporation.

NOTICE: This report was prepared as an account of work sponsored by an agency of the United States Government. Neither the United States Government, nor any agency thereof, nor any of their employees, nor any of their contractors, subcontractors, or their employees, make any warranty, express or implied, or assume any legal liability or responsibility for the accuracy, completeness, or usefulness of any information, apparatus, product, or process disclosed, or represent that its use would not infringe privately owned rights. Reference herein to any specific commercial product, process, or service by trade name, trademark, manufacturer, or otherwise, does not necessarily constitute or imply its endorsement, recommendation, or favoring by the United States Government, any agency thereof, or any of their contractors or subcontractors. The views and opinions expressed herein do not necessarily state or reflect those of the United States Government, any agency thereof, or any of their contractors.

Printed in the United States of America. This report has been reproduced directly from the best available copy.

Available to DOE and DOE contractors from
Office of Scientific and Technical Information
P.O. Box 62
Oak Ridge, TN 37831

Prices available from (703) 605-6000
Web site: http://www.ntis.gov/ordering.htm

Available to the public from
National Technical Information Service
U.S. Department of Commerce
5285 Port Royal Rd
Springfield, VA 22161

NTIS price codes
Printed copy: A07
Microfiche copy: A01

SAND99-0089
Unlimited Release
Printed June 1999

On the Fatigue Analysis of Wind Turbines

by

Herbert J. Sutherland
Sandia National Laboratories
P.O. Box 5800
Albuquerque, New Mexico 87185-0708

Abstract

Modern wind turbines are fatigue critical machines that are typically used to produce electrical power from the wind. Operational experiences with these large rotating machines indicated that their components (primarily blades and blade joints) were failing at unexpectedly high rates, which led the wind turbine community to develop fatigue analysis capabilities for wind turbines. Our ability to analyze the fatigue behavior of wind turbine components has matured to the point that the prediction of service lifetime is becoming an essential part of the design process. In this review paper, I summarize the technology and describe the "best practices" for the fatigue analysis of a wind turbine component. The paper focuses on U.S. technology, but cites European references that provide important insights into the fatigue analysis of wind turbines.

Acknowledgments

In this article, I have drawn upon the work of many researchers. I wish to express my appreciation to them and to the many others who have made significant contributions to the understanding of fatigue in wind turbines. Due to space limitations, I have not listed all of the references pertaining to my subject. Rather, I have tried to hit the high points and provide readers with sufficient information to expand their reading list, as they deem necessary.

The author also wishes to offer particular thanks to a group of his technical associates who have reviewed this article, in whole or in part. Their constructive criticism has greatly enhanced this review article. Thanks to Henry Dodd, Craig Hansen, Don Lobitz, John Mandell, Kurt Metzinger, Walt Musial and Paul Veers.

Table of Contents

page

1. Introduction 1

2. General Fatigue Nomenclature 3

3. Damage Rule Formulation 5

3.1. Miner's Rule 5
3.2. Linear Crack Propagation Models 7
3.3. Summary 8

4. Load Spectra 9

4.1. Analysis of Time Series Data 10
4.1.1. Rainflow Counting Algorithm 10
4.1.1.1. Peak-Valley Sequence 11
4.1.1.2. Digital Sampling 11
4.1.1.3. Range Filter 11
4.1.1.4. Residual Cycles 12
4.1.1.5. Cycle Count Matrix 12
4.1.2. Typical Rainflow Counting Example 13
4.2. Analysis of Spectral Data 14
4.2.1. FFT Analysis 14
4.2.1.1. Random Phase 15
4.2.1.2. Amplitude Variations 15
4.2.2. Typical Frequency Spectra Examples 16
4.3. Analytical Descriptions of Normal-Operation Load Spectra 18
4.3.1. Narrow-Band Gaussian Formulation 19
4.3.2. Exponential Formulation 20
4.3.3. Generalized Curve Fitting Techniques 20
4.3.3.1. Weibull Distribution 20
4.3.3.2. Higher Order Fits 21
4.3.4. Low-Amplitude Truncation 22
4.3.5. Load Parameters 23
4.3.6. Cycle Rate 23
4.4. Representative Samples 24
4.4.1. Minimum Data Requirements 24
4.4.2. Inflow Parameters 26
4.4.3. Scaling and Extrapolating Representative Samples 28
4.5. General Topics 29
4.5.1. Load Spectra Derived from Inflow Parameters 29
4.5.2. Structural Analyses 29

4.5.3. Bin Size 30
4.5.4. Mean Value Bins 30
4.5.5. Counting Cycles 31
4.5.6. Equivalent Fatigue Load 32
4.6. Total Load Spectrum 33
4.6.1. Transient Events 33
4.6.2. Transition Cycles 33
4.6.3. Comment 34
4.6.4. Summation of Load States 34
4.6.5. Partial Safety Factors 34
4.7. Off-Axis Analysis 34
4.7.1. Geometric Load Parameters 35
4.7.2. Typical Variations in Off-Axis Load Spectra 36
4.8. Specialized Load Spectra for Testing 37
4.8.1. Variable Amplitude Test Spectrum 37
4.8.1.1. WISPER 37
4.8.1.2. U.S. Wind Farm Spectrum 38
4.8.2. Load Spectra for Gears 39

5. Material Properties 41

5.1. Characterization of Fatigue Properties 42
5.1.1. Goodman Diagram 42
5.1.2. General Characterizations of Fatigue Behavior 43
5.1.2.1. Curve Fitting S-N Data 43
5.1.2.2. Goodman Fit for Mean Stress 45
5.1.2.3. Crack Propagation Model 45
5.2. Wood 46
5.2.1. General Properties 46
5.2.1.1. Mechanical Properties 46
5.2.1.2. Grading 47
5.2.2. Laminated Wood 47
5.2.2.1. Moisture Content 48
5.2.2.2. Attachments 48
5.2.3. Laminated Douglas Fir 48
5.2.3.1. Moisture Content 48
5.2.3.2. Fatigue Properties 49
5.2.3.3. Goodman Diagram 51
5.2.4. Other Wood Laminates 51
5.3. Metals 51
5.3.1. Steel 52
5.3.2. Aluminum 52
5.3.2.1. S-N Data Base 52
5.3.2.2. Spectral Loading 53
5.3.2.3. Linear Crack Propagation Data Base 54

5.3.3. Gears 55
5.4. Fiberglass Composites 55
5.4.1. Databases 56
5.4.1.1. DOE/MSU 56
5.4.1.2. European Database 56
5.4.2. Trend Analysis 56
5.4.3. General Data Trends 57
5.4.3.1. Fabric Architecture 58
5.4.3.2. Fiber Content 60
5.4.3.3. Normalization 61
5.4.3.4. Matrix Material 61
5.4.4. Modulus Changes 61
5.4.5. Predicting Service Lifetimes 63
5.4.5.1. Industrial Materials 63
5.4.5.2. Database Comparison 63
5.4.6. Spectral Loading 64
5.4.6.1. WISPER vs. WISPERX 65
5.4.6.2. Predicted Service Lifetime 65
5.4.7. Structural Details 66
5.4.7.1. Ply Drops 66
5.4.7.2. Locally Higher Fiber Content 68
5.4.7.3. Transverse Cracks 68
5.4.7.4. Environmental Effects 68
5.4.7.5. Equilibrium Moisture Content 69
5.4.7.6. Matrix Degradation 69
5.4.7.7. Property Degradation 70
5.4.7.8. EN-WISPER Spectrum 70
5.4.7.9. Effects of the Environment 71
5.4.8. Comments 71
5.5. Fatigue Limit Design 72
5.6. Partial Safety Factors 72

6. Inflow 75

6.1. Annual Average Wind Speed 75
6.1.1. Formulation 75
6.1.2. Typical Distributions 75
6.2. Inflow Characteristics 76
6.2.1.1. Turbulence 76
6.2.1.2. Vertical Shear 77
6.2.1.3. Additional Inflow Parameters 77
6.2.1.4. Reynolds Stresses 78
6.2.1.5. Summary 79

7. Solution Techniques 81

7.1. Closed Form Solution 81
7.1.1. Basic Assumptions 81
7.1.1.1. Annual Wind Speed Distribution 81
7.1.1.2. Cyclic Stress 81
7.1.1.3. Material Behavior 82
7.1.1.4. Damage Rule 82
7.1.1.5. Run Time 82
7.1.2. Solution 82
7.2. Numerical Solutions 83
7.2.1. The LIFE Duo of Fatigue Analysis Codes 83
7.2.1.1. Numerical Formulation 83
7.2.1.2. Input Variables 84
7.2.2. The ASYM Code 85
7.2.3. Gear Codes 86

8. Special Topics 87

8.1. Reliability Analysis 87
8.1.1. The Farow Code 87
8.1.2. Economic Implications 87
8.2. Analysis of Bonded Joints 88
8.2.1. The Bonded Joint 88
8.2.2. Tubular Lap Joints 89
8.2.2.1. Axial Loads 90
8.2.2.2. Bending Loads 92
8.2.2.3. Geometric Considerations 94
8.2.2.4. Contraction of the Adhesive During Cure 96
8.2.3. Bolted Studs 96
8.2.4. Adhesives 98
8.2.5. Comments 98
8.3. Nondestructive Testing 99
8.4. Full Scale Testing 100

9. Concluding Remarks 101

10. References 103

11. Appendices 121

Appendix A The Weibull Distribution 121
A.1. Generalized Distribution 121
A.2. Special Distributions 122
A.2.1. Rayleigh 122
A.2.2. Exponential 123
A.3. Time Series Relationships 123
Appendix B Turbine Data 125

B.1. Sandia/DOE 34-m VAWT Test Bed 125
B.2. Northern Power Systems 100kW Turbine 125
B.3. Micon 126

List of Tables

page

Table I. Specialized Values for the Forman Crack Growth Model..... 46

Table II. Typical Mechanical Property Ratios for Laminated Douglas Fir..... 49

Table III. Predicted and Measured Percent Decrease in Longitudinal Modulus due to Cracking of the ±45 Plies. 62

Table IV. Knock-Down Factors for Selected Structural Details in Tension and Compression for Approximately 70% 0° Materials. 67

Table V. Idealized Annual Climatological Cycle for the Dutch Environment. 71

Table VI. Accelerated Climatological Cycle for the Dutch Environment..... 71

List of Figures

page

Figure 1. The Stress-Strain Hysteresis Loop for a Fatigue Cycle 3
Figure 2. The Fatigue Cycle 3
Figure 3. The Fatigue Cycle at Various R-Values 4
Figure 4. Extrapolated Peak in a Typical Time Series 11
Figure 5. Typical Cycle Count Matrix for the Edgewise Bending Stress for the NPS 100 kW Turbine 13
a. Range and Mean Spectra for the Cycle Count Matrix 13
b. Range Spectra for the Cycle Count Matrix 13
Figure 6. Typical Cycle Count Matrix for the Flapwise Bending Stress for the NPS 100 kW Turbine 13
a. Range and Mean Spectra for the Cycle Count Matrix 13
b. Range Spectra for the Cycle Count Matrix 13
Figure 7. Amplitude Spectrum for the Root Flap Bending Stress for the NPS Turbine 16
a. Flapwise Bending Stress 16
b. Edgewise Bending Stress 16
Figure 8. Semi-Log Plot of the Cycle Count Distribution Obtained Using an FFT Analysis of the NPS Turbine 16
a. Flapwise Bending Stress 16
b. Edgewise Bending Stress 16
Figure 9. Comparison of the Alternating Stress Cycle Count Distributions for the NPS Turbine 17
Figure 10. Measured and Synthesized Flatwise Cycle Count Distributions for 34-m Test Bed VAWT 17
a. Amplitude Spectrum for Flatwise Bending Stress 17
b. Flatwise Alternating Stress Distribution 17
Figure 11. Comparison of the Rainflow Counted Cycle Count Distribution and the Narrow-Band Gaussian Model for the Sandia 34-m Test Bed. 19
a. Semi-Log Plot of the Cycle Count Distributions 19
b. Weibull Plot of the Cycle Count Distributions 19
Figure 12. Semi-Log Plot of the Cycle Count Distribution on the NPS Turbine 22
a. Flapwise Bending Stress 22
b. Edgewise Bending Stress 22
Figure 13. Comparison of the Rainflow Counted Cycle Count Distribution and the Generalized Gaussian Model for the Sandia 34-m Test Bed 22
a. Semi-Log Plot of the Cycle Count Distributions 22
b. Weibull Plot of the Cycle Count Distributions 22
Figure 14. Comparison of the Measured and Predicted RMS Flatwise Stresses for the Test Bed for Variable Speed Operation 23
Figure 15. Normalized Damage Trajectory for a Micon 65/13 Turbine 25

Figure 16. Damage Density Functions for the NPS 100kW Turbine 26
a. Flapwise Fatigue Load Spectrum..... 26
b. Damage Density Function for Welded (m ≅ 3) Materials..... 26
c. Damage Density Function for Composite (m ≅ 10) Blade Materials..... 26
Figure 17. Effect of Segmented Data on the Prediction of Service Lifetimes..... 31
Figure 18. Geometric Parameters for an Elliptical Root Section 35
Figure 19. Cycle Count Matrices for a Range of Bending Stress Directions..... 36
a. Bending Stress at 0° 36
b. Bending Stress at 45° 36
c. Bending Stress at 90° 36
d. Bending Stress at -30°..... 36
e. Bending Stress at -45°..... 36
f. Bending Stress at -60°..... 36
Figure 20. Cumulative 2-Month Reference Alternating Load Spectrum..... 39
Figure 21. High and Low Turbulence Torque Spectrum for the Micon 65..... 39
Figure 22. Time-at-Torque Histogram for the Micon 65 40
a. Linear Histogram 40
b. Weibull Plot 40
Figure 23. Schematic S-N Diagram for Various Fatigue Critical Structures..... 41
Figure 24. Typical Symmetric Goodman Diagram..... 42
Figure 25. S-N Diagram for Douglas Fir/Epoxy Laminate..... 49
Figure 26. Goodman Diagram at 107 Cycles for Douglas Fir/Epoxy Laminate 51
Figure 27. Normalized S-N Diagram for 6063-T5 Aluminum..... 53
Figure 28. Fracture Mechanics Characterization for Aluminum Alloys 54
Figure 29. Crack Growth in an Aluminum Blade..... 54
Figure 30. S-N Diagram for Carbonized Steel Gears 55
Figure 31. Extremes of Normalized S-N Tensile Fatigue Data for Fiberglass Laminates, R=0.1..... 57
Figure 32. Extremes of Normalized S-N Compressive Fatigue Data for Fiberglass Laminates, R = 10..... 58
Figure 33. Extremes of Normalized S-N Reverse Fatigue Data for Fiberglass Laminates, R = -1 58
Figure 34. Extremes of Normalized S-N Fatigue Data for a Single Family of Fiberglass Laminates with 72% 0° Plies and 28% ±45° Plies, R = 0.1..... 58
Figure 35. Dry Fabric Samples..... 59
Figure 36. Fatigue Sensitivity Coefficient for Fiberglass Laminates as a Function of Fiber Content, at R = 0.1 60
a. Fatigue Sensitivity Coefficient for Various Fiber Contents in Fiberglass 60
b. Fatigue Sensitivity Coefficient for Unidirectional Fiberglass Laminates..... 60
Figure 37. Effect of Matrix Material on Tensile Fatigue in a 61
Figure 38. Reduction of Tensile Modulus in a Fiberglass Laminate with 0° and ±45° Plies Damaged in Tensile Fatigue 62

Figure 39. Goodman Diagrams for Fiberglass Composites 63
a. Goodman Diagram based on the MSU/DOE Database 63
b. Goodman Diagram Based on the FACT Database 63
Figure 40. S-N Diagram for a Fiberglass Laminate with 0° and ±45° Plies, under WISPER Loading Conditions..... 65
Figure 41. Typical Ply Drop Configurations 66
a. External Ply Drop 66
b. Internal Ply Drop..... 66
Figure 42. S-N Diagram for a Fiberglass Laminate with 0° and ±45° Plies, under Wet and Dry Environment Conditions. 70
Figure 43. Weibull Probability Density Functions for Various Shape Factors..... 75
Figure 44. Variation of Low Wind Speed Start/Stop Cycles with Cut-In Power 85
Figure 45. Variation of Annual Energy Production with Cut-In Power 86
Figure 46. Variation of Service Lifetime with Cut-In Power..... 86
Figure 47. A Typical Lap Joint..... 89
a. Corner of a Lap Joint 89
b. Shear Stress in a Lap Joint 89
Figure 48. Geometry of the Tubular Lap Joint..... 90
Figure 49. Stress Distribution in Cylindrical Lap Joint Under Tensile Loads 91
a. Von Mises Stress Distribution 91
b. Radial (Peel) Stress Distribution..... 91
Figure 50. S-N Fatigue Data for an Aluminum-to-Fiberglass Bonded Joint..... 91
Figure 51. Tubular Lap Joint Under Bending Loads 92
a. Tubular Lap Joint..... 92
b. C-Scan of the Debond Failure Regions 92
Figure 52. 3-D Finite Element Mesh of a Circular Bond Joint..... 92
Figure 53. Composite Peel Stress Distribution Along the Top of the Joint (0° Circumferential Position)..... 93
Figure 54. Partial Finite Element Meshes with Varying Adhesive Geometries..... 93
a. Truncated Adhesive 93
b. Dab of Adhesive..... 93
c. Dollop of Adhesive 93
Figure 55. Normalized Shear Stress Distribution Along the Joint..... 94
Figure 56. Schematic of the Joint Geometries 95
Figure 57. Composite Peel Stress with a Dollop of Adhesive and a Tapered Adherend for an Axial Compressive Load 95
Figure 58. Composite Peel Stress due to Adhesive Contraction..... 96
Figure 59. Typical Metal Stud Design. 97
Figure 60. Fatigue Behavior of a Typical Metal Stud Bonded into a Wood Laminate 97
Figure 61. The Sandia 34-m Test Bed Turbine 125
Figure 62. The Northern Power Systems 100 kW Turbine 126

1. INTRODUCTION

Somewhat over two decades ago, utility grade wind turbines were designed using static and quasi-static analyses. At best, these rather simple analyses led to over-designed turbines, and at worst, they led to premature failures. The latter is exemplified by high failure rates observed in the early California wind farms. We, as designers, soon realized that wind turbines were *fatigue critical machines*; namely, the design of many of their components is dictated by fatigue considerations. And, not only is this machine fatigue critical, its unique load spectrum greatly exceeds our previous experience. This realization led to a large quantity of research that has now matured to the extent that state-of-the-art designs can include detailed fatigue analyses of the wind turbine.

The intent of this paper is to review these developments and to describe the "best practices" for the fatigue analysis of wind turbine components. The paper focuses on U.S. technology but cites European references that provide important insights. Most major sections are introduced with a "tutorial" section that describes basic concepts and defines pertinent terms. In all cases, an extended reference list is provided. Illustrative examples are included, as warranted. The author assumes that the reader is acquainted with the general architecture of modern wind turbines and the general concepts of their design. These concepts have been described in many previous publications. The reader can draw upon several references that examine the history of wind turbines [1, 2] and their design [3-7].

To facilitate this discussion, the first major section of the paper uses the Palmgren-Miner linear damage rule [8], commonly called Miner's Rule, to formulate the fatigue analysis of wind turbines. This damage rule is currently used throughout the industry, and it is a good starting point to begin our discussions. After a general introduction to this rule, the rule is specialized to the analysis of wind turbines. In the form used for the analysis of wind turbine components, the rule requires three main classes of input data: the load spectra, material properties, and inflow characterization. Each of these components is discussed in a major section of the paper. The final major section of the paper pulls these components back together into the evaluation of service lifetime for a wind turbine component. Specific examples from various wind turbines are used throughout the paper to illustrate important points and to provide the reader with the details of typical fatigue calculations for wind turbines.

2. GENERAL FATIGUE NOMENCLATURE

As illustrated in Fig. 1, the fatigue cycle is a closed stress-strain hysteresis loop in the stress-strain time series of a solid material. For illustrative purposes, the cycle is usually depicted as a sinusoid, see Fig. 2. The maximum stress, σ_{max}, is the largest algebraic value of the stress in the stress cycle (commonly called the peak) and the minimum stress, σ_{min}, is the least (commonly called the valley). *Tensile stresses are taken to be positive and compressive stresses are taken to be negative.*

The *mean stress*, σ_m, is the algebraic average of σ_{max} and σ_{min}:

$$s_m = \frac{s_{max} + s_{min}}{2} \quad . \qquad (1)$$

The *range* of the stress cycle, σ_r, is defined to be:

$$s_r = \left| s_{max} - s_{min} \right| \quad , \qquad (2)$$

and the *amplitude* of the stress cycle, σ_a, equals half of the range and is given by:

$$s_a = \left| \frac{s_{max} - s_{min}}{2} \right| = \frac{s_r}{2} \quad . \qquad (3)$$

The R ratio is the ratio of σ_{min} to σ_{max}, namely,

$$R = \frac{s_{min}}{s_{max}} \quad . \qquad (4)$$

The fatigue cycle for various mean stresses and R values is depicted in Fig. 3.

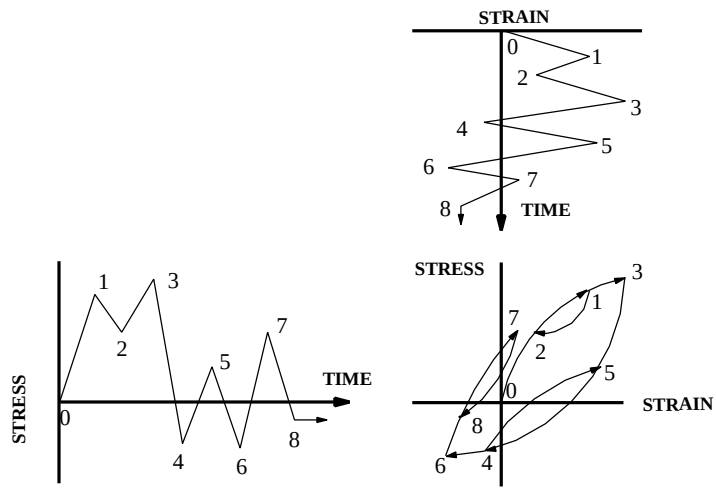

Figure 1. The Stress-Strain Hysteresis Loop for a Fatigue Cycle.

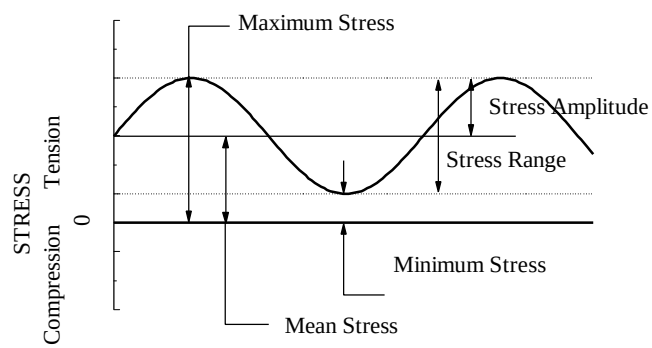

Figure 2. The Fatigue Cycle.

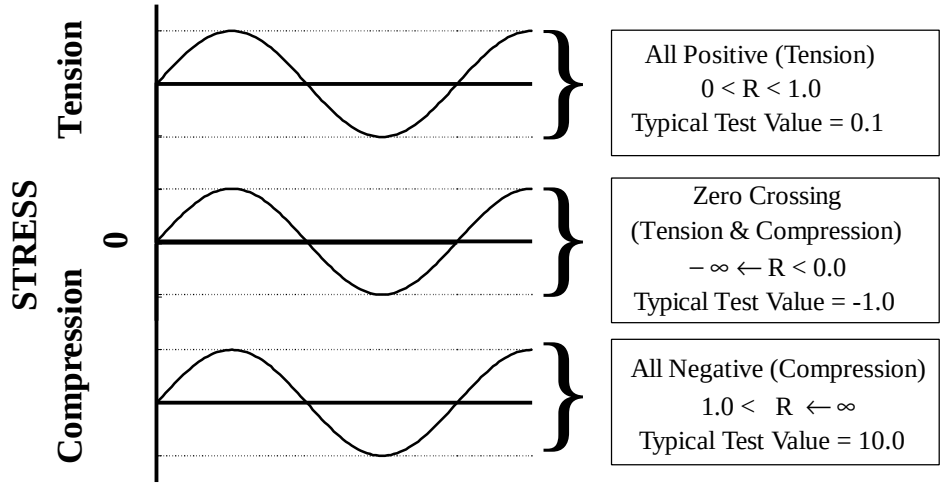

Figure 3. The Fatigue Cycle at Various R-Values.

3. DAMAGE RULE FORMULATION

General fatigue analysis has been discussed in an exceptionally large number of textbooks, reference manuals and technical papers. The ones that I have found to be particularly useful are listed in Refs. 9 through 14. These references provide both a general introduction and detailed analysis techniques for the fatigue analysis of common structures. They provide a common starting point for fatigue analysis of wind turbines. Fatigue analyses that have been specialized to the prediction of service lifetimes for wind turbines are discussed in Refs. 4, 6, 15 and 16.

3.1. Miner's Rule

The recognized standard [17] for the fatigue analysis of wind turbines is the *Palmgren-Miner linear damage rule, i.e., Miner's Rule,* [8]. The damage law may be written in the following form:

$$\sum_{i}^{M} \frac{n_i}{N_i} = \frac{n_1}{N_1} + \frac{n_2}{N_2} + \frac{n_3}{N_3} + \ldots + \frac{n_M}{N_M} = D \quad , \tag{5}$$

where the total damage D is sustained by a structure that undergoes n_1 stress cycles at stress level σ_1, n_2 stress cycles at stress level σ_2, n_3 stress cycles at stress level σ_3 and so on, for all stress levels through the final level of M. N_i is the *number of cycles to failure* at stress level σ_i. The number of cycles n_i is usually taken to be the number of full cycles (closed hysteresis loops). But it can also be the number of reversals (two reversals for each full cycle) or the number of "cross-overs" (zero-crossings). And the stress level is usually taken to be the amplitude or range at a given R value or mean stress. *Thus, one must be cautious with cycle counts and stress levels. Always check the reference to ascertain the definition of the cycles used to characterize material data and fatigue loads.*

Miner's Rule assumes that structural failure will occur when the damage equals one. As discussed by Veers [18], the computed damage D at failure over a wide range of references varies between 0.79 and 1.53. When dealing with wind turbines, additional uncertainties arise from the variation in material properties and applied loads. *Thus, differences of a factor of 2 between damage predictions and measured lifetimes are not only common in wind turbine applications, they should be expected.*

Typically, the fatigue cycles imposed upon a structure are analyzed or measured over some fixed period of time. Thus, D, in Eq. 5, is usually expressed as the *damage rate* ΔD_t associated with the sample time t. If this damage rate is equal to average damage rate over the service lifetime of the component T (i.e., $\Delta D_t = \Delta D_T$), then the service lifetime of the structure T is the reciprocal of ΔD_t, namely:

$$T = \frac{1}{\Delta D_T} = \frac{1}{\Delta D_t} \quad . \tag{6}$$

Again, *Eq. 6 is predicated on the assumption that failure will occur when the damage equals one, and that the damage rate computed over time t is representative of the average damage rate imposed upon the structure during its service lifetime*. Namely, the number and distribution of fatigue cycles contained in the sample are essentially identical to the number and distribution over the structure's service lifetime.

The number of cycles to failure, N in Eq. 5, is a measure of the material's ability to endure stress cycles. This material property is typically described with an "S-N" curve. Actually, the S-N description of the fatigue characteristics for a given material is a family of curves that depends on both the mean (Eq. 1) and the range (Eq. 2) or amplitude (Eq. 3) of the stress cycle. The R variable (Eq. 4) is also used extensively in the description of S-N data, e.g., see Rice et al. [9].

If we assume that the fatigue cycles imposed upon the structure may be described by some function of σ_m and σ_a, then Eq. 5 can be written in integral form as:

$$D = \int_{-\infty}^{\infty}\int_{0}^{\infty} \frac{n(s_m, s_a)}{N(s_m, s_a)} \, ds_a \, ds_m \quad . \tag{7}$$

Alternate formulation of Eq. 7 could be written in terms of $n(\sigma_m, \sigma_r)$ or $n(\sigma_m, R)$. When counted over a specific period of time, the damage is typically cast as a damage rate ΔD_t, namely the damage D accumulated in time t. Rewriting Eq. 7 to include time dependence yields:

$$\Delta D_t = \frac{D}{t} = \int_{-} \int_{0} \frac{n_t(\sigma_m, \sigma_a)}{N(\sigma_m, \sigma_a)} \, d\sigma_a \, d\sigma_m \quad . \tag{8}$$

If the damage rate computed over time t is representative of the average damage rate accumulated by a component over its service lifetime, then the service lifetime T is the reciprocal of the damage rate computed over time t. Thus, the predicted service lifetime T, see Eq. 6, becomes:

$$\frac{1}{T} = \Delta D_t = \int_{-} \int_{0} \frac{n_t(\sigma_m, \sigma_a)}{N(\sigma_m, \sigma_a)} \, d\sigma_a \, d\sigma_m \quad . \tag{9}$$

For wind turbine applications, the cycle counts n(•) are typically taken to be an explicit function of the short-term average inflow velocity U (typically, U is based on a ten-minute average). Wind speed is chosen as an independent variable because most loads, performance parameters, and control algorithms are directly related to the short-term average velocity of the inflow. Using the probability density function p_U for the inflow velocity U, Eq. 9, may be written as:

$$\frac{1}{T} = \Delta D_t = \int_{0} p_U(u) \int_{-} \int_{0} \frac{n_t(\sigma_m, \sigma_a, U)}{N(\sigma_m, \sigma_a)} \, d\sigma_a \, d\sigma_m \, du \quad , \tag{10}$$

and if the turbine is only operated between a cut-in velocity of U_{in} and a cut-out velocity of U_{out}, then:

$$\frac{1}{T} = \Delta D_t = \int_{U_{in}}^{U_{out}} p_U(u) \int_{-} \int_{0} \frac{n_t(\sigma_m, \sigma_a, U)}{N(\sigma_m, \sigma_a)} d\sigma_a \, d\sigma_m \, du \quad . \tag{11}$$

The probability density function p_U is usually taken to be the annual wind speed distribution at the site of the wind turbine (see the discussion in section 6.2 "Inflow Characteristics" on p. 76). Equation 11 describes the damage incurred on the wind turbine during normal operation. Other terms, typically arising from transient events, are discussed in section 4.6 "Total Load Spectrum" on p. 33. This integral equation is typically changed to a finite summation for numerical analysis [19].

3.2. Linear Crack Propagation Models

In addition to a Miner's rule based damage analysis, linear crack propagation models [12, 13] have had successful applications to the analysis of wind turbine components. In this analysis technique, a crack subjected to N load cycles will grow from an initial length of a_o to a final length of a_f based on its crack growth rate of da/dn; namely,

$$a_f - a_o = \int_0^N \left(da/dn \right) dn \quad . \tag{12}$$

The growth rate is material dependent. Typical formulations characterize this behavior in terms of the stress intensity factor K, which has the form:

$$K = y(\ ) \, \sigma \sqrt{\pi a} \quad , \tag{13}$$

where y(•) is the shape factor that is a function of specimen geometry and crack length [14]. For very large bodies subjected to tensile stress, y(•) is a constant equal to 1.

In an equivalent relationship to that shown in Eq. 11, Eq. 12 may be expanded to the following:

$$\Delta a = \int_{U_{in}}^{U_{out}} p_U \int_{-} \int_{0} \frac{da\left[K_m, K_a, y(\ )\right]}{dn} n_t(\sigma_m, \sigma_a, U) \, d\sigma_a \, d\sigma_m \, dU \quad , \tag{14}$$

where K_m and K_a are stress intensity factors associated with the mean and alternating stress, respectively. This form is easily changed to a finite summation for numerical analysis, see Eq. 62 and Sutherland and Schluter [20].

3.3. Summary

Thus, three sets of information are required to estimate the service lifetime of a wind turbine: the fatigue load cycles on the turbine as a function of the inflow conditions, the S-N behavior or the linear crack growth of the material(s) being analyzed, and the annual wind speed distribution. The following three sections describe these inputs in detail and present typical examples. Where required, the examples have been obtained using the LIFE2 fatigue analysis code for wind turbines [21]. This numerical simulation technique is described in section 7.2.1 "The LIFE Duo of Fatigue Analysis Codes" on p. 83.

4. LOAD SPECTRA

As implied by the formulation presented in Eq. 11, the spectrum of fatigue loads on a wind turbine, i.e., $n(\sigma_m,\sigma_a,U)$, has a significant dependence on the operational state of the turbine. In Eq. 11, this dependency is described as a function of the inflow conditions. This characterization is rather simplistic in that the operation of the turbine is dependent on many variables, only one of which is the inflow velocity. To make the problem tractable, most analysts divide the operational states of the turbine into a series of (independent) operational states that describe the various sets of fatigue loads on the turbine. A typical division would be:

1) A series of operation states that describes the loads on the turbine during normal operation. In a typical formulation, these states are taken to be a function of the inflow velocity. The range of the inflow velocity is from the cut-in velocity U_{ci} of the turbine to its cut-out velocity U_{co}.
2) A series of "start/stop" operation states that describes the loads on the turbine during normal stops, emergency stops, etc.
3) A series of "buffeting" operational states that describes the loads on the turbine while it is stopped, but its blades and other structural components are being buffeted by the inflow.
4) Any additional operational states that impose significant fatigue loads on the structure that are not covered by the other three operational states.

This division of load cases falls within the *standard set of load cases that has been established by the International Electrotechnical Commission, IEC,* for the design of wind turbines [17, 22].

Once the load states are defined, each must be characterized through experimental and/or analytical investigations. However, as wind turbines are subjected to random input from the inflow, this task can be quite difficult. Typically, the analyst will obtain a representative sample of the loads imposed on the turbine during each state and then weight them by their expected rate of occurrence. In the above list, the first and third series of operational states are weighted by the probability density function for the annual wind speed distribution p_U (see Eq. 11) and the second state by the number of expected events in each one of its categories. *Typically, survival loads under extreme wind conditions are not included in the fatigue analyses.*

In each operational state, the object is to obtain a numerical or analytical description of the $n(\sigma_m,\sigma_a,U)$ function. This function may take the form of tabular data or it may be an analytical expression. The former is commonly called a cycle count matrix, that "bins" the fatigue cycles by their mean, amplitude, range R value and/or sequence [23]. The functional form of choice for the description of $n(\sigma_m,\sigma_a,U)$ depends on the damage rule chosen to predict service lifetimes, e.g., the linear damage rule cited in Eq. 11. The cycle count distribution is usually presented in one of three forms [24]:

1) range spectrum
2) range and mean spectrum

3) Markov matrix

These three representations are listed in increasing order of information. The range spectrum is simply a column of cycle counts, and the counts are placed in bins based upon their range, i.e., a one-dimensional function. The range and mean spectrum is a two-dimensional (2-D) matrix of the cycle counts that are placed in a two-dimensional array of bins based upon their range and mean, i.e., a two-dimensional function. The Markov matrix retains the peak and valley from each cycle and some information about their sequence. In the Markov "from-to" matrices, the sequence information is a probability function that describes which peak will follow a given valley and which valley will follow a given peak. For linear damage analysis, Eq. 11, the sequence of the fatigue cycles is not required. *Thus, characterization (1) or (2) is the characterization of choice for the typical fatigue analysis of a wind turbine.*

In this section of the paper, I describe the three primary methods for creating the $n(\sigma_m,\sigma_a,U)$ function: time series data, frequency domain spectral data and analytical expressions. Each of these methods may be obtained from experimental investigations and/or analytical simulations. After the major techniques have been discussed, I will discuss related topics that arise when conducting the fatigue analysis of wind turbines.

4.1. Analysis of Time Series Data

In many cases, the results of an experimental or an analytical investigation of the stress and strains produced in the turbine structure by the loads imposed upon it are plots that follow the stress (strain) as a function of time. These time series are typically generated from an experimental or analytical investigation of the turbine. Detailed discussions of the techniques used to obtain these time series are beyond the scope of this report. And, they have been discussed extensively in previous reports, e.g., Madsen [25] and Pedersen [26]. For the purposes of this report, I assume that the necessary time series are available for the fatigue analysis. A few precautions related to time series data are discussed in section 4.5 "General Topics" on p. 29.

4.1.1. Rainflow Counting Algorithm

Time series data, either derived from analytical simulations or from actual measurements, have been studied extensively by other researchers. The wind industry has drawn upon their techniques for converting time series into cycle count matrices. A number of numerical techniques are available from these previous studies. The technique typically used in the wind turbine industry is the rainflow counting algorithm presented in Downing and Socie [27]. A complete description of this algorithm is also provided in Rice et al. [9]. One adaptation of the technique to wind turbines is described in Sutherland and Schluter [28]. Wu and Kammula [29] have developed a real-time algorithm using rainflow-counting techniques that reduces memory requirements and speeds computations.

The implementation presented by Downing and Socie [27], requires both a pre and a post processor for its implementation into a form that is useful for analysis. This section discusses this

counting process from the input of a time series to the final output. Also, several questions that arise when this technique is used for the analysis of wind turbines are addressed.

4.1.1.1. Peak-Valley Sequence

The input to the rainflow counting algorithm is a simple series of peaks and valleys (troughs), i.e., local maxima and minima, that form hysteresis loops, see Fig. 1. To convert a time series to the appropriate list, a pre-processor searches for local extremes in the series and lists them in sequence [28]. Typically, the algorithm uses a change in slope as an indicator that the time series is going though a peak or valley. Only the magnitude of the peak or valley is then entered into the rainflow counting algorithm. The algorithm defines the first point in the time series to be the first entry in the peak-valley list.

4.1.1.2. Digital Sampling

Typically, the load time series that is being analyzed by the rainflow counter is based on a time series that has sampled digitally. Because there is no guarantee that the actual extreme value was sampled, see Fig. 4, a curve-fitting algorithm may be used to estimate the actual extreme. In a typical algorithm [28 and 30], a parabola is fit to the three data points that surround each local extreme. The correction for sampling errors is relatively small for the data rates typically used to sample loads data from wind turbines. Figure 4 illustrates the extremes predicted by this technique with typical data.

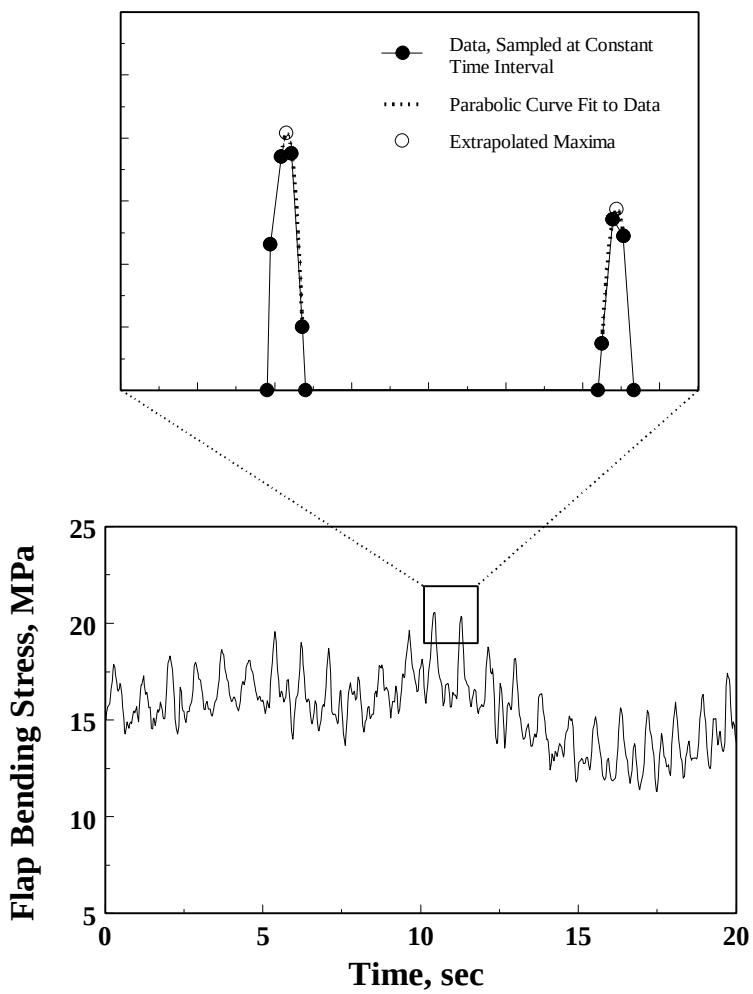

Figure 4. Extrapolated Peak in a Typical Time Series.

4.1.1.3. Range Filter

To avoid counting the many small cycles that result from numerical jitter in the time

series and/or to eliminate the many small cycles that do not contribute significantly to the damage of the wind turbine, a range filter is typically used. This filter requires that successive local extremes must differ by a minimum value, typically called the threshold, before they are considered to be extremes that should be retained by the filter. Various algorithms have been proposed for processing time series data. A useful one is the racetrack filter described by Veers et al. [30].

4.1.1.4. Residual Cycles

The rainflow counting algorithm proceeds by matching peaks and valleys to form closed hysteresis loops. When the algorithm reaches the end of time-series data record, a series of unmatched peaks and valleys remains unclosed and, therefore, are not counted by the algorithm. These so-called "half-cycles" typically include the largest peak and valley in the record and they may also include other large events. Thus, the potentially most damaging events (the largest cycles) contained in the time series are not counted by the classical formulation of the rainflow algorithm. If desired, the rainflow counting algorithm can be easily modified to include these half–cycles in the cycle count [28, 29].

Various researchers have proposed several techniques for handling these half-cycles in wind turbine applications. Some ignore them, some count them as half of a complete cycle (hence, their name), and others count them as full cycles. The latter is the most conservative approach. *However, the recommended practice, as stated in Madsen [25], is to treat all unclosed cycles as half cycles. This recommendation is currently being retained in the IEC standards [31].*

4.1.1.5. Cycle Count Matrix

The output of the rainflow counting algorithm is a characterization of the stress (strain) cycle by its maximum and its minimum value. The counting algorithm counts each cycle in its order of occurrence. The post-processor then puts this information into a form suitable for the fatigue analysis package.

The first task of the postprocessor is to convert this characterization of a fatigue cycle to that used by the fatigue analysis. As discussed above, the final data representation typically takes one of three forms: range spectra, range and mean spectra, and Markov matrices. Thus, the post-processor's first task is to convert the maximum/minimum representation of the data into one of these forms. The second task is to format the data for processing by the damage analysis. This step typically includes placing each cycle in the appropriate cycle-count bin[1] and writing that information to file. The output file can take many forms, depending on the analysis and numerical techniques being used to determine the damage. Thus, a specialized post-processor is usually required for each fatigue analysis technique.

[1] A fatigue cycle is added to a cycle count bin if its magnitude falls within the bounds of the bin. All cycle counts within a bin are assumed to have the same magnitude. This characteristic magnitude is a function of the end points of the bin. An example of a 2-D bining operation is shown in the next section of the paper.

4.1.2. Typical Rainflow Counting Example

A typical rainflow counted load spectrum is shown in Fig. 5 for the edgewise-bending stress and in Fig. 6 for the flapwise-bending stress. These data were collected from an NPS 100-kW turbine in Altamont Pass, California [32]. The data are for normal operating conditions with a mean inflow velocity of 11.0 m/s. As shown in Figs. 5a and 6a, the distribution of cycle counts that is obtained from the rainflow counting algorithm was post-processed into a 2-D matrix that places each cycle into a cycle count bin based upon its mean and range (or amplitude). In this form, a cycle count is added to bin (i,j) when

$$(\sigma_m)_{i-1} \quad (\sigma_m) \quad (\sigma_m)_i \quad , \tag{15}$$

$$(\sigma_a)_{j-1} \quad (\sigma_a) \quad (\sigma_a)_j \quad , \tag{16}$$

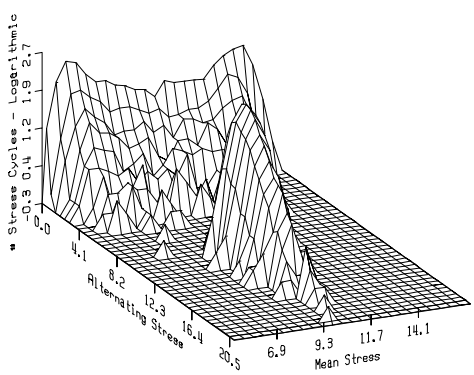

Figure 5a. Range and Mean Spectra for the Cycle Count Matrix.

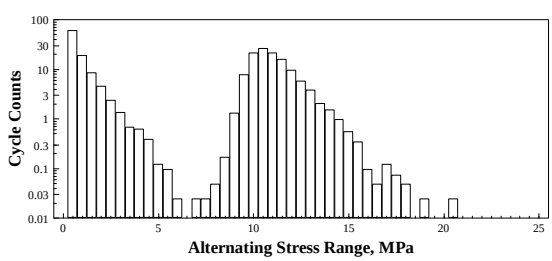

Figure 5b. Range Spectra for the Cycle Count Matrix.

Figure 5. Typical Cycle Count Matrix for the Edgewise Bending Stress for the NPS 100 kW Turbine.

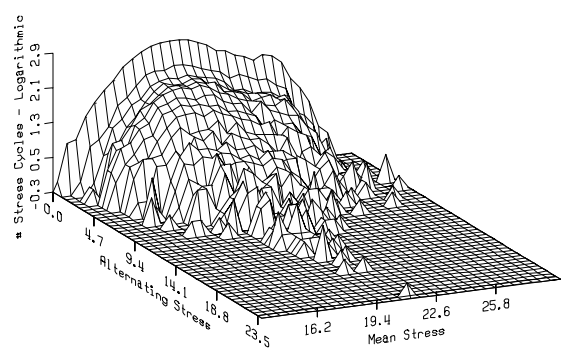

Figure 6a. Range and Mean Spectra for the Cycle Count Matrix.

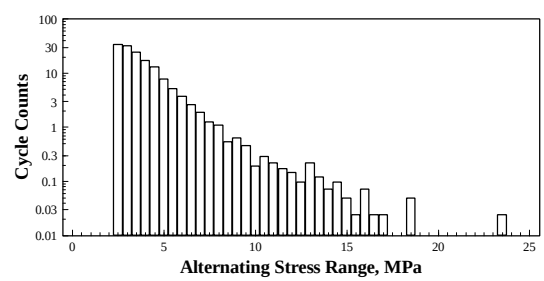

Figure 6b. Range Spectra for the Cycle Count Matrix.

Figure 6. Typical Cycle Count Matrix for the Flapwise Bending Stress for the NPS 100 kW Turbine.

where bin (i,j) has the a maximum mean stress of $(\sigma_m)_i$ and a maximum alternating stress (range) of $(\sigma_a)_j$ and the cycle being counted has a mean stress of (σ_m) and a range (or amplitude) of (σ_a). *The width of each of the bins in this matrix can significantly influence the fatigue calculations.* See the guidelines discussed in section 4.5 "General Topics" on p. 29.

The 2-D form for the cycle count matrix may be simplified to a 1-D form for analysis (as noted above) and/or for presentation of results. Figures 5b and 6b illustrate typical 1-D distributions of the range of the cycle counts. The 1-D distributions in these two figures are derived from the 2-D cycle count matrix by holding the range constant and summing over all means. In many analyses, the 1-D distribution is used, because the range of mean stresses is typically not important for wind turbine predictions. This observation is discussed in section 4.5.4 "Mean Value Bins" on p. 30

4.2. Analysis of Spectral Data

Typically the development of the cycle count function $n(\sigma_m,\sigma_a,U)$ from experimental or analytical data depends heavily on time series data. However, many structural analysis techniques yield frequency-domain stress spectra, and a large body of experimental loads (stress) data is reported in the frequency domain. To permit the fatigue analysis of this class of data, several approaches have been developed to obtain cycle counts from frequency spectra. In one technique, a series of computational algorithms based on Fourier analysis techniques has been developed [33, 34]. In another technique, rainflow ranges are theoretically estimated directly from the power spectral density (PSD) function for the turbine [35, 36]. Only the former technique will be discussed here.

4.2.1. FFT Analysis

The Fourier analysis technique developed by Sutherland [33, 34] uses an inverse Fast Fourier Transform (FFT) to transform the frequency spectrum to an equivalent time series suitable for cycle counting [37]. In this formulation, the input frequency spectrum is taken to be a uniform series of N components with frequency intervals of Δf. The spectrum is input as a series of positive amplitudes A_i and phase angles ϕ_i , i = 1, N. Most FFT algorithms are optimized for values of N that are a power of 2.

The inverse FFT algorithm converts the frequency spectrum into a time series of the form:

$$\sigma\left(t_j\right)\Big|_{j=1}^{2N} = FFT^{-1}\left\{\left[A\left(f_i\right),\phi\left(f_i\right)\right]\Big|_{i=1}^{N}\right\} \quad , \tag{17}$$

where the ith component of the amplitude spectrum corresponds to a frequency of

$$f_i = (i-1)\,\Delta f \quad , \text{where } i = 1, \ldots, N, \tag{18}$$

the jth component of the time series corresponds to a time of

$$t_j = (j-1)\,\Delta t \quad , \text{where } j = 1, \ldots, 2N, \tag{19}$$

and,

$$\Delta t = \frac{1}{2\,\mathrm{N}\,\Delta \mathrm{f}} \quad . \tag{20}$$

The output time series has a total time length T equal to

$$\mathrm{T} = 2\,\mathrm{N}\,\Delta t = \frac{1}{\Delta \mathrm{f}} \quad . \tag{21}$$

Thus, the final output of the algorithm is a time-series that may be counted using the rainflow counting algorithm cited above.

The edgewise blade spectrum for a HAWT typically shows a very strong deterministic signal that is the direct result of the gravity loads. This observation led Sutherland [33] to develop an alternate formulation of the FFT shown in Eq. 17 that permits large deterministic signals to be handled efficiently. This alternate formulation is not reproduced here.

4.2.1.1. Random Phase

The frequency spectrum of the operating loads on a wind turbine blade contains two classes of signals. The first is a deterministic or "steady" signal that is obtained by averaging the time series data as a function of the position of the rotor (the azimuth-average). The second signal in the spectrum is the random (non-deterministic) variation about the azimuth-average. These random components in the distribution imply that the synthesis of a time series from a frequency spectrum for wind turbines does not have a unique solution, as implied by Eqs. 17 through 21.

Akins [37, 38] handled the synthesis of both signals using the average amplitude spectrum with a random phase angle for each component. He concludes, however, that the synthesis process would be more realistic if the phase angles used in the synthesis process have both deterministic and random components. In particular, he notes that the phase angles for the azimuth-average components are essentially deterministic, and, therefore, the components of the spectra that correspond to the azimuth-average signal should have deterministic phase angles. And he further suggests that the remaining components be synthesized using random phase angles. Computationally, the non-uniqueness of the input phase angles in the frequency spectrum implies that much iteration is required to achieve a statistically meaningful result.

4.2.1.2. Amplitude Variations

The frequency spectra for typical wind turbines vary significantly about the average spectrum due to the random nature (both in time and in space) of the inflow. Two classes of variations are noted: the first is the random (non-deterministic) variation of the spectral amplitudes about their average at a constant average wind speed and the second is the variation of the time series with wind speed. The variation of the latter is typically handled by using multiple wind speed bins in the fatigue analysis, see the discussion above. But, the variation of the former must be handled

within each wind speed bin. Sutherland [33] presents one technique for handling this variation in amplitude. His technique is used in the example presented next.

4.2.2. Typical Frequency Spectra Examples

The frequency spectra for the NPS 100-kW turbine [32], are shown in Fig. 7. The spectrum for the flapwise bending stress is shown in Fig. 7a, and for the edgewise bending stress in Fig. 7b. The results of a rainflow count of the time series synthesized by the FFT analysis are shown as 2-D cycle count matrices in Fig. 8. A comparison of the measured and the synthesized cycle-count distributions is shown in Fig. 9. Similar results are presented in Fig. 10 for the 34-meter Test Bed

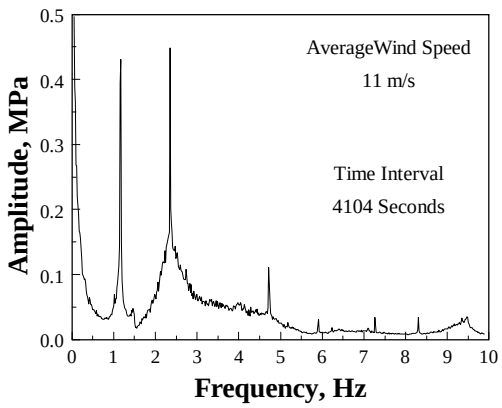

Figure 7a. Flapwise Bending Stress.

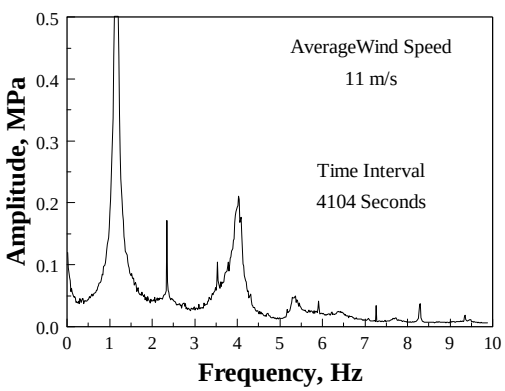

Figure 7b. Edgewise Bending Stress.

Figure 7. Amplitude Spectrum for the Root Flap Bending Stress for the NPS Turbine.

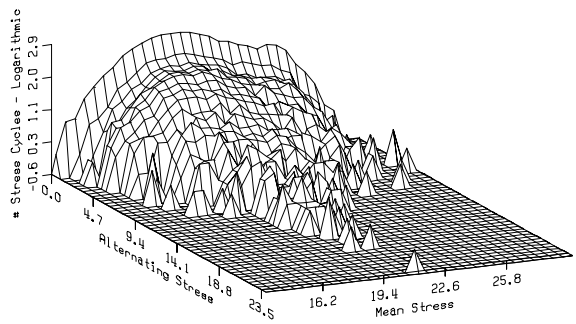

Figure 8a. Flapwise Bending Stress.

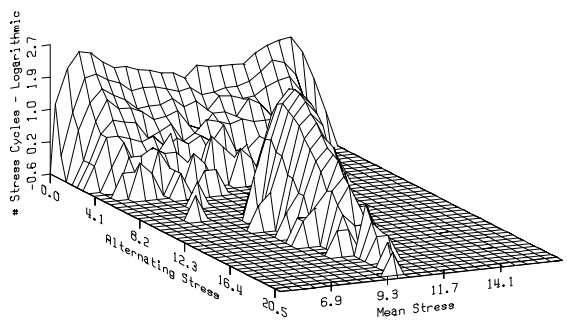

Figure 8b. Edgewise Bending Stress.

Figure 8. Semi-Log Plot of the Cycle Count Distribution Obtained Using an FFT Analysis of the NPS Turbine's Frequency Spectrum.

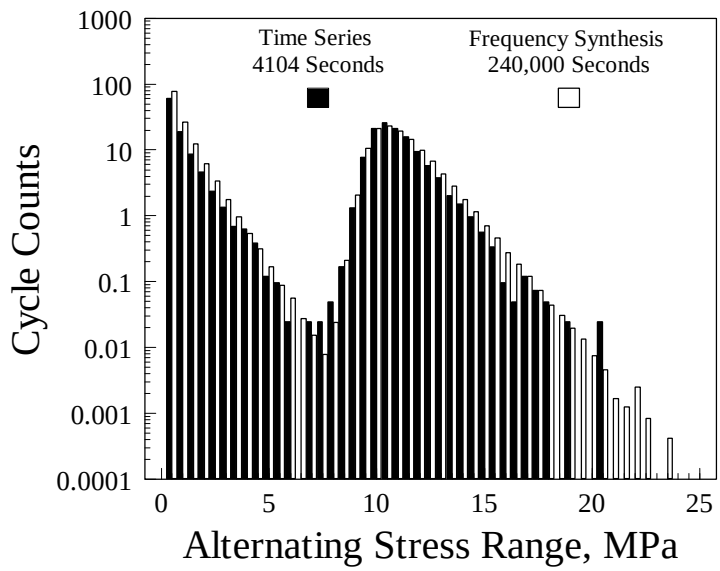

Figure 9. Comparison of the Alternating Stress Cycle Count Distributions for the NPS Turbine.

VAWT (vertical-axis wind turbine) in Bushland Texas [39].

As reported by Sutherland and Osgood [40], the synthesis process and rainflow counting requires many iterations to achieve a stable distribution of cycle counts. For each iteration, a different set of random phase angles is used for the non-deterministic components of the spectrum, while constant phase angles are used for the deterministic components. And, the amplitude spectrum was varied about its mean. A cycle count matrix is considered to be

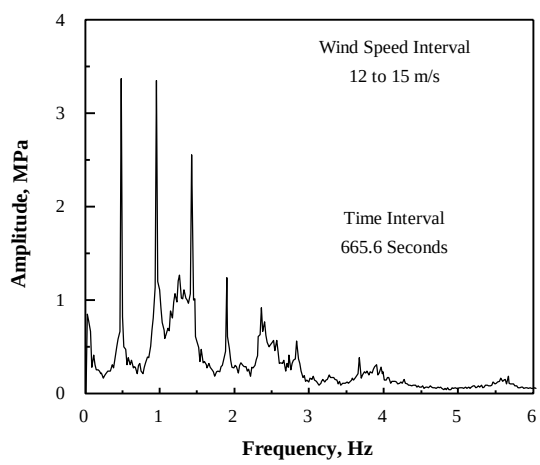

Figure 10a. Amplitude Spectrum for Flatwise Bending Stress.

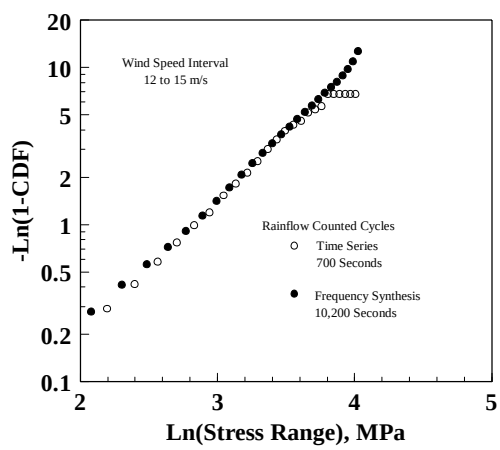

Figure 10b. Flatwise Alternating Stress Distribution.

Figure 10. Measured and Synthesized Flatwise Cycle Count Distributions for 34-m Test Bed VAWT.

stable if the normalized distribution of the cycle counts does not change when additional time series are synthesized and counted. For these two examples, the cycle count matrix was considered stable when the normalized number of cycle counts in each stress bin stayed within a half cycle count of its previous value when the synthesis time was doubled.[2] Also, the high-stress tail of the cycle count distribution was used to judge the stability of the synthesis process. Namely, the distribution was considered stable if the tail of the distribution was a relatively smooth function. For the two examples discussed here, the total synthesized time required to achieve a stable cycle count distribution was approximately 240,000 seconds in the NPS turbine and 10,200 seconds for the Test Bed turbine.

The comparisons shown in Figs. 9 and 10b illustrate that time series data for the determination of stress cycles imposed on a wind turbine blade may be effectively synthesized from average frequency-spectra data. Moreover, the ability of the algorithm to generate long time series permits the high-stress tail of the cycle count distribution to be defined within the accuracy of the input frequency spectrum. *However, the ability to fill out the tail of the distribution should not be confused with the actual distribution of stress cycles imposed upon the turbine. The frequency spectra used in the analysis are still based upon a rather limited set of data, and those spectra may not contain sufficient information to define the correct high-stress tail of the distribution of cycle counts.*

4.3. Analytical Descriptions of Normal-Operation Load Spectra

Analytical representations have been used extensively to describe cycle count distributions. These representations not only provide the analysts with closed-form solutions for the fatigue analysis but through the insight they provide, these formulations permit incomplete data to be interpolated and/or extrapolated to fill voids in the data. Moreover, these representations when combined with reliability analysis permit the evaluation of the effects of randomness in the input variables on the predicted service lifetime of a wind turbine.

Several analytical expressions have been used to describe the load spectra on a wind turbine blade. These expressions are typically derived from best-fit analyses of experimental data. Most of the successful expressions fall within a generalized Weibull distribution with the narrow-band Gaussian distribution (Rayleigh distribution) being used extensively to describe the load spectra on Vertical Axis Wind Turbines (VAWTs), and the exponential distribution for the load spectra on Horizontal Axis Wind Turbines (HAWTs). [Weibull probability density functions for various shape factors are shown below in Fig. 43.] In this section of the paper we discuss both of these techniques and a generalized fitting technique that distorts a parent distribution to better fit the loads on the machine.

[2] The stability of a cycle count matrix (distribution) can also be defined based on the damage rate. Namely, the cycle count distribution is considered stable if the damage rate represented by these cycles changes by some small percentage when the synthesis time is increased significantly.

4.3.1. Narrow-Band Gaussian Formulation

One of the first uses of an analytical expression to describe the load spectra on a blade was the characterization of the load spectra on VAWTs using a narrow-band Gaussian formulation by Malcolm [41, 42], Veers [18, 43-45] and Akins [46]. In this formulation, the distribution of cycle counts takes the form of a Rayleigh distribution, a specialized form of the general Weibull distribution (see Appendix A). For this distribution, the Weibull shape factor, α, has a value of 2. This distribution may be written in the following form:

$$p_{s|U} = \left[\frac{s_a}{s_U^2}\right] \exp\left[\frac{-s_a^2}{2\, s_U^2}\right] \quad , \tag{22}$$

where the probability density function $p_{\sigma|U}$ of the cyclic stress σ_a is a function of the standard deviation of the cyclic stress σ_U at a wind speed U. To convert this probability density function into cycle counts, the cycle count rate, which is discussed in section 4.3.6 "Cycle Rate" on p. 23, is required. The cycle count distribution is obtained by multiplying the probability density function shown in Eq. 22 by the cycle count rate.

Figure 11 presents a comparison of the measured (and rainflow counted) cycle count distribution

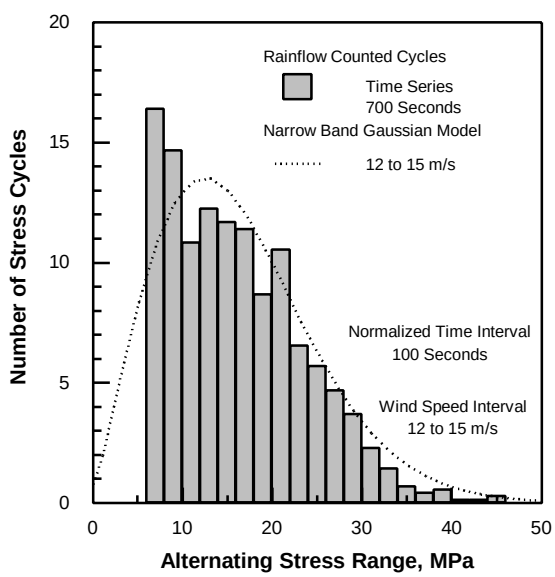

Figure 11a. Semi-Log Plot of the Cycle Count Distributions.

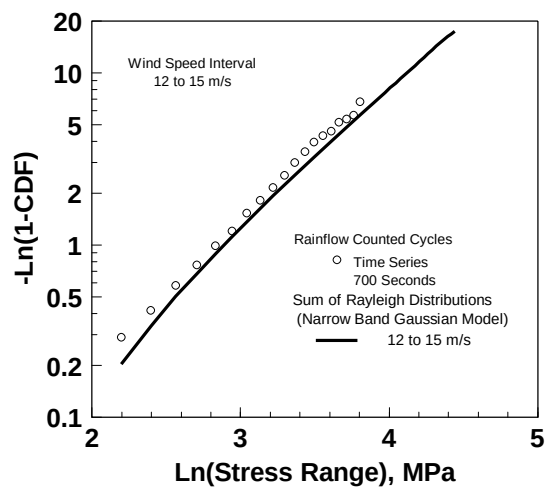

Figure 11b. Weibull Plot of the Cycle Count Distributions.

Figure 11. Comparison of the Rainflow Counted Cycle Count Distribution and the Narrow-Band Gaussian Model for the Sandia 34-m Test Bed.

and its Gaussian approximation for the 12 to 15 m/s wind speed bin for the 34-meter Test Bed VAWT in Bushland Texas [39]. This figure illustrates the very good agreement between the measured and modeled cycle count distributions in the body and the tail of the distribution. As implied in this figure, this technique is only used to describe the distribution of the fatigue cycles with respect to their alternating stress component. *In cases where the S-N material properties are a function of the mean stress, this formulation of the cycle count distribution implies that the damage calculations must be based on a constant (non-zero) mean stress across the entire distribution* [43].

4.3.2. Exponential Formulation

The exponential distribution used by Jackson [47, 48], Kelley [49, 50] and Kelley and McKenna [51] is also contained in the generalized Weibull distribution, see Appendix A. For this distribution, the Weibull shape parameter α has a value of 1. The distribution may be written in the following form:

$$p_{s|U} = \left[\frac{1}{s_U}\right] \exp\left[\frac{-s_a}{s_U}\right] = \left[\frac{1}{\overline{s}_U}\right] \exp\left[\frac{-s_a}{\overline{s}_U}\right] \quad , \tag{23}$$

where the probability density function $p_{\sigma|U}$ of the cyclic stress σ_a at a particular wind speed U is a function of the standard deviation of the cyclic stress σ_U (in this case, σ_U is equivalent to the mean of the cyclic stress $\overline{s}_U$). Again, the mean stress is assumed to be a constant across this distribution of cycle counts.

The distribution function that was proposed by Kelley [49] is actually the sum of three distributions, with the exponential distribution describing the high-stress tail of the distribution. A Gaussian distribution is used to describe the low-stress region and a log-normal distribution is used to describe the transition between the low and high stress regions.

4.3.3. Generalized Curve Fitting Techniques

<u>4.3.3.1. Weibull Distribution</u>

The Rayleigh and exponential distributions cited above can be generalized to the Weibull distribution. In its generalized form, the distribution becomes

$$p_{s|U} = \left[\frac{a}{b}\right]\left[\frac{s_a}{b}\right]^{a-1} \exp\left\{\left[\frac{-s_a}{b}\right]^{a}\right\} \quad , \tag{24}$$

where the Weibull parameters α and β can be expressed as functions of the mean and standard deviation of the cycle count distribution (Appendix A).

4.3.3.2. Higher Order Fits

A generalized curve fitting technique, named FITTING, that provides fourth order fits to the data has been proposed by Winterstein et al. [52, 53]. This formulation optimally retains the statistical information of the high-stress level data (i.e., the tail of the cycle count distribution) by distorting a parent distribution to fit the first four statistical moments of the data. Importantly, this technique distorts the parent distribution when the data indicate that the distribution differs from the parent distribution. The tail is fit to the observed distribution by warping the parent distribution (two parameter distributions) using two additional parameters: the skewness (3rd moment of the distribution) and the kurtosis (4th moment of the distribution). Three parent distributions are available in the FITTING routine: a Gaussian, a Weibull, and a Gumbel. *In subsequent analyses, Winterstein and Kashef [54] demonstrated that for the one-sided distributions typically encountered in cycle-counts, three-moment distributions provide better fits of the data than four-moment distributions.*

As discussed above, previous fits to cyclic load distributions from wind turbines have emphasized Rayleigh and exponential distributions, which are special cases of the Weibull distribution. Weibull distributions can model a wide range of behaviors with two parameters to describe the central tendency of the distribution (i.e., the body of the distribution) and the spread of the distribution (i.e., the tail of the distribution). With its versatility and the previous emphasis that has been placed on its use, a generalized Weibull fit will be used exclusively in the examples presented here.

Typical generalized curve fits for the data presented in Figs. 8 and 11 are given in Figs. 12 and 13, respectively. As illustrated in these figures, the fit has excellent agreement with the data in the body and the tail of the distribution. And, as discussed above, the low-amplitude portion of the distribution is not included in the fit because it is of no consequence in the damage calculations. Moreover, Winterstein et al. have recommended that the curve fit should not include the low-amplitude cycles because they will decrease the accuracy of the fit in the body and the tail of distribution where the damage is concentrated for typical blade materials. As with its specialized forms, the generalized technique only describes the distribution of the fatigue cycles with respect to their alternating stress component. And, *the mean stress is assumed to be a constant across this distribution of cycle counts*. The elimination of the low-amplitude stress cycles and the mean stress variations from the fitting process are particularly evident when Fig. 8 is compared to Fig. 12.

The importance of defining the correct functional form for the distribution of cycle counts is discussed in Sutherland and Butterfield [55]. When the same cycle count distribution was fit with an exponential distribution and with a Rayleigh distribution, the former was found to contain ten times more damage than the latter. This significant increase in damage is a direct result of the cycles contained in the tail of the distributions, with the exponential predicting more cycles in the tail than the Rayleigh. Thus, the fitting technique is extremely important, and its form should not be prejudged. And, by using the generalized fitting routine, the fitting algorithm obtains the best fit to the data by choosing both the form of the underlying distribution and its distortion.

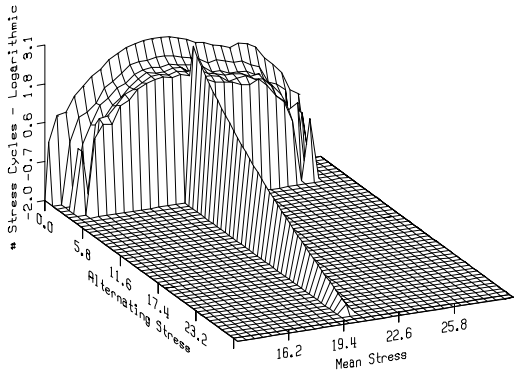

Figure 12a. Flapwise Bending Stress.

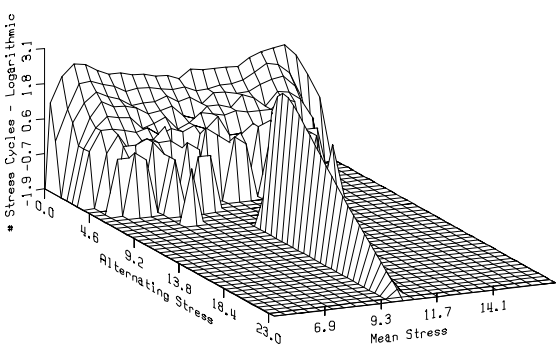

Figure 12b. Edgewise Bending Stress.

Figure 12. Semi-Log Plot of the Cycle Count Distribution on the NPS Turbine.

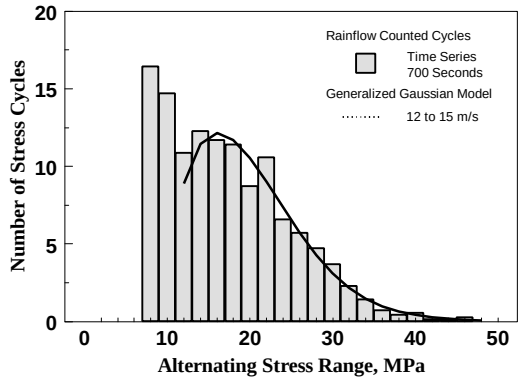

Figure 13a. Semi-Log Plot of the Cycle Count Distributions.

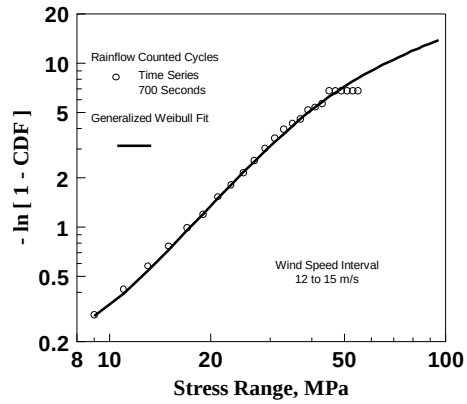

Figure 13b. Weibull Plot of the Cycle Count Distributions.

Figure 13. Comparison of the Rainflow Counted Cycle Count Distribution and the Generalized Gaussian Model for the Sandia 34-m Test Bed.

4.3.4. Low-Amplitude Truncation

The curve-fitting procedures described above are implicitly tied to the assumption that the initial portion of the cycle count distribution is not important in a damage calculation. For example, the analytical distribution shown in Fig. 13a matches the measured cycle counts very well above approximately the 14 MPa bin. Below this bin, the distribution falls to zero, while the measured distribution increases dramatically, with the smallest bin having several thousand counts. As discussed in section 4.4.1 "Minimum Data Requirements" on p. 24 and illustrated by Fig. 16, *these counts are typically not significant in the determination of damage and may be ignored in*

the curve fitting procedure. In special cases, these low-damage (approaching zero) cycles can be included in the damage analysis by maintaining them as true cycle count bins, as shown in Fig. 12 or by adding multiple piecewise distributions together [49].

4.3.5. Load Parameters

For all of the above formulations, the functional relationship between the stress state parameters and the characteristics of the inflow must be determined before they can be applied. As cited in Eqs. 22 and 23, the Rayleigh and the exponential formulations are one-parameter models that describe this functional relationship. In both cases, this parameter is related to the RMS blade stress σ_U; which is then related to the average inflow wind speed U. To date, the majority of the work characterizing this relationship uses the Rayleigh model to characterize VAWT loads. A typical relationship between σ_U and U, for the 34-m Test Bed turbine [39], is shown in Fig. 14 [56]. This relationship is typically characterized as a piece-wise, linear relationship for analysis [57].

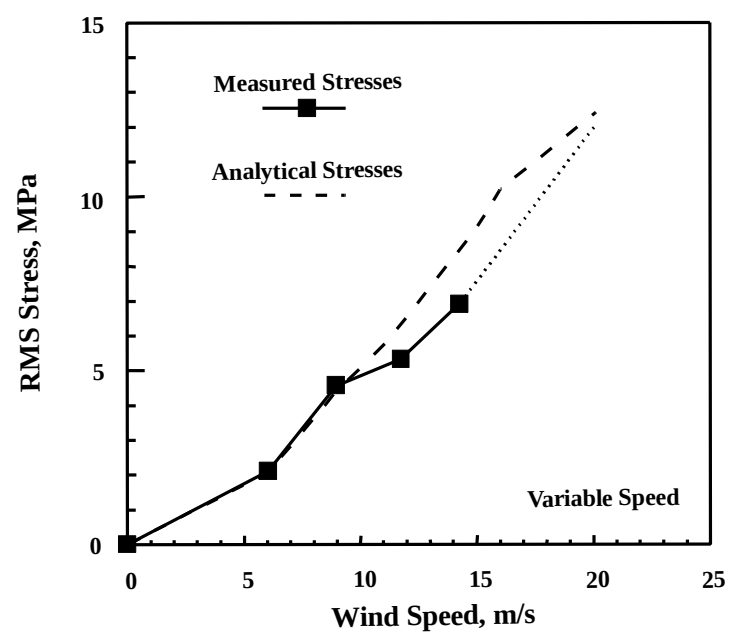

Figure 14. Comparison of the Measured and Predicted RMS Flatwise Stresses for the Test Bed for Variable Speed Operation.

As the formulations are extended to higher orders, the descriptions of the parameter set required by the models can become significantly more complicated. Higher order characterizations are reported in Lange and Winterstein [58], Kashef and Winterstein [59] and Veers and Winterstein [60].

4.3.6. Cycle Rate

In most of these formulations, the distribution of stress cycles is represented as a normalized distribution. Thus, the total number of stress cycles contained in the distribution (or, more precisely, the average rate at which stress cycles are imposed upon the structure) is another parameter required by the fitting procedure. There have been several techniques proposed for assessing the value of this variable.

The first, and the most obvious technique, is to use one of the cycle counting techniques discussed above to determine the average rate of cycle accumulation. This technique was used by Sutherland and Veers [61] in their evaluation of the effectiveness of these models and in the detailed analysis of the fatigue loads on the Sandia 34-m Test Bed [57]. Other methods, originally proposed by Veers, use the dominant frequency of blade vibration [43] or the rate of mean level crossings [18] as the average cycle rate. In these two methods, the frequency is usually chosen to be independent of wind speed. Typically for VAWTs, the cycle rate is chosen to be three times the rotational rate of the turbine for edgewise stresses and two times for flatwise stresses. For HAWTs, the edgewise rotation cycle rate is chosen equal to the rotation rate. In their comparisons of results, Ashwill et al. [57] illustrate that the measured cyclic rates were higher than the estimated rate, but, when the damage from these two rates was compared, the differences were not significant.

4.4. Representative Samples

As indicated in Eq. 11, the normal operation cyclic loads are typically weighted using the annual wind speed distribution and then summed to find the total operating load spectrum. This analysis technique implicitly assumes that each normal-operation wind-speed bin contains a representative sample for all of the inflow conditions characterized by the short-term average inflow velocity. Each sample is typically extremely short in time when compared to the design lifetime of the turbine, i.e., minutes or hours as opposed to years.

As discussed by Winterstein (his comments are reported in Sutherland and Butterfield [55]), representative samples are adequate for this application because the fatigue analysis needs only to accurately estimate the *mean damage rate* at a given operational state. In other words, fatigue analysis should not require more loads data if the service lifetime is increased from 30 to 60 years, say. This observation is especially important because it implies that the fatigue analysis can be based on representative samples that can then be scaled to the lifetime of the turbine. However, *the representative sample conjecture requires that the sample be truly representative and that statistical models can use this sample to extrapolate from relative short-term data to long-term data.*

4.4.1. Minimum Data Requirements

The importance of obtaining a truly representative sample has been graphically presented in Sutherland and Veers [61]. In this paper, Sutherland and Veers demonstrate that the damage contained in separate 10-minute data segments, taken for normal operation of the 34-m Test Bed at a constant mean wind speed, can vary by *two orders of magnitude*.

In a follow-on analytical study, Kelley and Sutherland [62] examined damage predictions for a Micon 65/13 turbine installed in Row 37 of a 41-row wind farm in San Gorgonio Pass, California. They examine accumulated damage in the blades during a typical diurnal variation of the inflow at the San Gorgonio site. Of the total 144 ten-minute simulations, 37 simulations had a mean inflow velocity between 11 and 13 m/s. The normalized damage trajectory based on the sequential analysis of the 37 ten-minute simulations is illustrated in Fig. 15. In this plot, the average damage

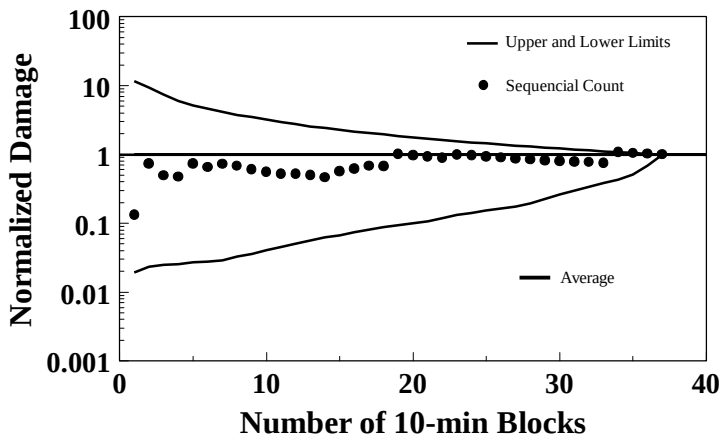

Figure 15. Normalized Damage Trajectory for a Micon 65/13 Turbine.

rate for the 37 simulations is normalized to one. The average nominal damage rate is then plotted as a function of the number of ten-minute records included in the average. This plot demonstrates that the damage stays within approximately +7 and -25 percent of its average value after the first 19 10-minute simulations (3.1 hours). Thus, one would surmise that a representative sample requires a minimum of 19 simulations for this operational state and turbine. However, if sequencing in the trajectory is changed, a very different result is obtained. Namely, consider the upper and lower bound trajectories shown in the figure. In these plots, the simulations are added in the order of the damage they contain, with the upper bound sorted in descending order and the lower bound sorted in ascending order. First, these trajectories demonstrated that the simulation containing the smallest damage underestimates the average damage by almost two orders of magnitude and the largest overestimates the average damage by over one order of magnitude. And, the sample requires almost all of 37 simulations before it stabilizes to the average damage rate. Thus, when the trajectory is based on ordered members of the data set, the trajectory essentially does not stabilize until all members of the set have been added because the sample is not representative. Techniques for insuring that a representative sample has been obtained are typically based on obtaining a representative set of inflow conditions, such as turbulence intensity in each mean wind speed bin. Criteria for this technique are discussed in section 4.4.2 “Inflow Parameters” on p. 26.

In another study, Winterstein and Lange [52] note that the data requirement for representative samples also depends on the coefficient of variation (COV) that is acceptable in the damage calculation. Using the data from the Northern Power Systems 100-kW turbine and assumed values for the COV of the damage and material variability, they estimated that at least 280 minutes (4.7 hours) are required to define the cyclic load distribution for a composite blade.

As reported in Sutherland and Butterfield [55], Winterstein notes another critical concept when determining minimum data requirements for fatigue analyses. In particular, fatigue analyses depend heavily on *both the loads and the fatigue behavior of the material*; e.g., the slope of the S-N curve (i.e., m in Eq. 34, below) used to define damage rate (Eq. 8). As shown in Fig. 16, the damage contained in the flapwise bending stress spectrum, Fig. 16a (also shown in Fig. 6b), is concentrated in the body of the distribution when the exponential slope m is small (typical of welded materials), Fig. 16b, and in the tail of the distribution when the slope is large (typical of

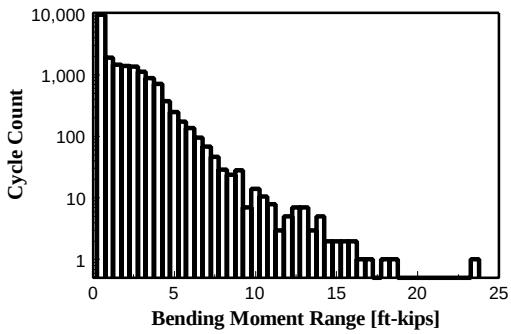

Figure 16a. Flapwise Fatigue Load Spectrum.

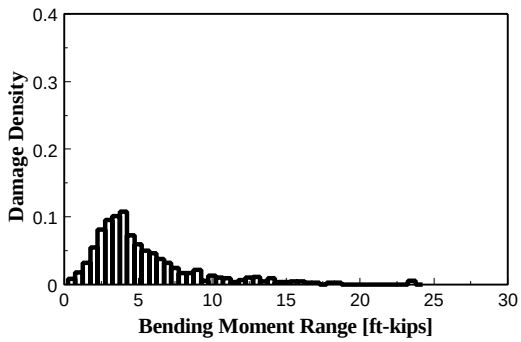

Figure 16b. Damage Density Function for Welded (m @3) Materials.

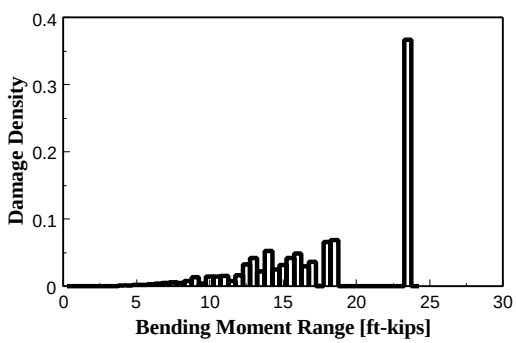

Figure 16c.Damage Density Function for Composite (m @10) Blade Materials.

Figure 16. Damage Density Functions for the NPS 100kW Turbine.

composite materials), Fig. 16c.[3] Thus, the blade material becomes an important parameter when determining whether a sample is representative and sufficient. *For small exponents, the body of the distribution must be determined accurately, and for large exponents, the tail of the distribution is more important.*

Thus, these analyses indicate that the current best estimate of the minimum quantity of data required to obtain a representative sample is on the order of several hours for each operation state with an m of approximately 10. This statement is predicated on the assumption that the external conditions for that state are contained in the sample and in their proper portions. For example, each average wind speed bin used to describe a normal operational state should contain a variation in turbulence levels that is based on site characteristics or certification requirements.

4.4.2. Inflow Parameters

To assist in collecting samples that are truly representative, the data are usually taken across a series of inflow conditions. To the first order, normal operational states depend mostly on the mean wind speed, but secondary factors are also important. These factors are intended to describe the instantaneous inflow velocity variations across the rotor disk. They are typically characterized by the vertical wind shear

[3] Typical values of the fatigue exponent for steel and aluminum are 3 and 6, respectively. For typical fiberglass blade materials, the exponent is larger than 10. The fatigue exponent is discussed in detail in section 5 "Material Properties" on p. 41.

across the rotor and the single-point turbulence intensity measured at hub-height in front of the turbine. Although these parameters are typically the only ones specified in the certification process, several other parameters have been proposed for characterizing the inflow across the rotor. These parameters warrant consideration when defining a representative sample for all of the inflow conditions from short-term average inflow velocity data. Sets of parameters that have been proposed for defining the inflow are discussed in section 6.2 “Inflow Characteristics” on p. 76.

In another approach to the problem, Kashef and Winterstein [59] have demonstrated that the dependence of the blade loads on mean wind speed and turbulence may be reduced to a single variable that is based on the standard deviation of the high-frequency turbulence. Namely, when the low-frequency components (well below the rotor speed) of the inflow velocity u are removed, the resulting turbulence level σ_H can be correlated to the distribution of fatigue cycles across all mean inflow velocities. The initial evaluation of this correlation was based on data from a single turbine. When extended to another, smaller data set, the correlation to σ_H broke down and was replaced by a dependence on the average inflow velocity U.

The crux of the analyses summarized here, as pointed out by Kashef and Winterstein [59], is that the correlation between fatigue loads and inflow parameters is probably case dependent. At this time, the appropriate distribution of inflow parameter(s) across a cycle count bin has not been identified. The IEC Standards Committee, [17, 22] recommends that the turbulence intensity, as a function of average inflow velocity, should be the governing parameter for describing the inflow for design load calculations. The IEC recommendations define this functional relationship. Implicit to this formulation is that the turbulence intensity will be a constant across a cycle count bin. My view is that this approach is somewhat simplistic and that *the fatigue load spectrum should use, at the very least, a distribution of turbulence intensities across each cycle count bin*.

From an analysis standpoint, the inflow is typically described using the SNLWIND model [63-65]. In this model, the mean inflow velocity, the integral length scale, and the shear velocity (related to the turbulence σ) are typical input parameters for the turbulence and coherence modeling of the inflow. Thus, additional variations in length scales and/or the Reynolds stresses [particularly the $\overline{(u\,w)}$ term] are warranted when defining the inflow distributions across a particular cycle count bin; see the detailed discussion of inflow parameters in section 6.2 “Inflow Characteristics” on p. 76.

Cuerva-Tejero et al. [66] have suggested yet another approach to solving this difficult problem. They used “principal component” and regression analysis to identify combinations of inflow parameters to develop a set of four factors that describe the inflow. In general, these four factors may be associated with various parings of the common inflow parameters. One factor is associated with the mean wind speed; the second with the high-level statistics of the wind speed (skewness and kurtosis); and the third and fourth with the stochastic characteristics of the wind speed (combinations of a length scale, a correlation coefficient and the standard deviations of its three components), and the fourth is turbulence and the correlation between the horizontal component and the vertical component).

As discussed here, many parameters have been suggested as descriptors for the inflow. Which descriptors are necessary and sufficient remain to be determined.

4.4.3. Scaling and Extrapolating Representative Samples

Once the representative sample of the loads has been determined, the sample must be scaled in time to lifetime loads. Several techniques are currently used to scale them. Many designers simply scale the sample loads directly. For normal operation, this scaling is typically based on the average annual wind speed distribution discussed in section 6.2 "Inflow Characteristics" on p. 76. These designers note that the samples define the main body of the load distribution, and thus, they capture all of the necessary loads on the turbine to define its service lifetime.

Other designers note that the infrequent occurrences of high-stress events contained in the "tail of the load distribution" are affected by the specific data set, and that the distribution tails fill in as more and more data are added to the record [47, 67]. And, as noted above, the existence of a "high stress tail" on the distribution has significant influence on the predicted service lifetime of the turbine. Thus, they believe that it must be well defined for an accurate analysis. This group of designers typically extrapolates from the body of the cycle count distribution into this tail region.

As discussed by Lange and Winterstein [58], the data contained in a representative sample defines the main body of the load distribution on the turbine very well. However, the extreme loads in the high-stress tail of the distribution may or may not be defined accurately. In section 4.3 "Analytical Descriptions of Normal-Operation Load Spectra" on p. 18, curve-fitting techniques are used to develop analytical descriptions of the load distribution. These fits may also be used to extrapolate limited data to the prediction of the tail of the load distribution. Thus, statistical measures of the data are potentially very useful for deducing the shape and magnitude of the low-probability-of-occurrence, high-stress tail of the load distribution.

There are two critical issues for this technique. The first concerns the use of statistical modeling to deduce the shape and magnitude of the low-probability-of-occurrence, high-stress tail of the load distribution and the second concerns the extent of the predicted tail that is realized during the life of the turbine.

For the latter, the argument is that under a probabilistic framework, large loads are possible, but they are associated with a decreasing rate-of-occurrence (i.e., large return period or a decreasing exceedence probability). Hence they may quickly become irrelevant in practical applications, such as wind turbines with a finite service lifetime. While these large-load cycles may truly have a finite probability of occurrence, their existence is controversial and typically difficult to estimate from data. Several researchers have questioned the realism of the prediction in the tail of the distribution [55]. Their skepticism is based on the realization that the relatively small representative sample is to be extrapolated to a 30-year lifetime. Consider the case where each wind speed bin contains only a single 10-minute record. For an 8 m/s Raleigh site (see the discussion in section 6.1 "Annual Average Wind Speed" on p. 75), the turbine will operate approximately 5.5 percent of the time in the 11-12 m/s wind speed bin. Thus, the extrapolation technique is being asked to extend the data from the 1 per 10 minutes fractal to the 1 per 1.65

year fractal (5.5 percent of 30 years); i.e., by a factor of approximately 90 thousand (0.055x30x365x24x6)! Even if an hour of data is used in each bin, the extrapolation will be almost 15 thousand.

The discussion on the existence and extent of this high stress tail is very important because, as noted above, the tail of the distribution is critical to the prediction of service lifetimes for composite turbine blades. Most designers fit the data with a distribution. In some cases, the designer will use the entire predicted distribution while others will truncate the distribution at five or ten times its RMS value (2nd moment of the distribution). *However, at this time, there is no consensus concerning the use of statistical models for predicting the shape and the extent of the tail of the load distribution used in service lifetime predictions.* For conservative predictions, a distribution should be fit to the available data and used to extrapolate these data to long service lifetimes. And, in no case should the distribution be truncated below the maximum measured or simulated load level.

4.5. General Topics

4.5.1. Load Spectra Derived from Inflow Parameters

The analytical formulations cited in the previous section are descriptive models. Namely, they use measured loads data at a given set of inflow conditions and operational parameters to obtain mathematical formulations that describe the loads on the turbine. As discussed by Kashef and Winterstein [59], the correlation between fatigue loads and inflow parameters is probably case dependent, because each turbine will react to a turbulent inflow spectrum based on such parameters as its size, architecture, modal frequencies, and damping characteristics. *Thus, the descriptive nature of these models implies that they are turbine and site specific.*

A number of techniques have been proposed for extending the description of a turbine at one site to another site or to another turbine. Jackson [68] offers a classical route to the extension of these formulations from descriptive models to predictive models. In this analysis, dimensional analysis is used to scale the size of the turbine. In another technique, Kashef and Winterstein [59] use a de-trending analysis to change sites. Spera [69] uses empirical relationships, derived from rotationally-sampled inflow data, to obtain fatigue loads from structural analysis codes. And, in yet another approach developed by Kelley [49] and by Barnard and Wendell [70], the inflow time series is rainflow counted. The inflow cycles are then related to the fatigue cycles using a transfer function. They postulate that the transfer function is constant for a given turbine.

4.5.2. Structural Analyses

The only true prescriptive models that can be used to analyze the fatigue loads, without experimental measurements, are based on analytical inflow and structural analysis codes [25, 26]. In this technique, an inflow model is combined with atmospheric design specifications and with aerodynamic load and structural analysis models to prescribe the fatigue loads on the turbine [24]. The SNLWIND model, proposed by Veers [63, 64] and upgraded to three components by Kelley [49, 65], is typically used in the U.S. The European models are typified by the work of Mann

[71]. Popular aero/structural codes used in the U.S. are the analyses by Wilson et al. using the FAST code [72], Hansen using the YawDyn code [73], and Elliott and Wright using the Adams/WT code [74]. Detailed discussions of these codes are beyond the scope of this report. Quarton [75] provides a detailed summary of wind turbine design analysis.

The direct application of the structural analysis codes for predicting of fatigue loads is beyond the scope of this report and will not be discussed here. Direct ties between structural analysis codes and fatigue analysis have been conducted by Wilson et al., [76] for the FAST code and Laino and Hansen [77-79] for the YawDyn and Adams/WT codes.

4.5.3. Bin Size

Binsing rainflow cycle counts into count matrices is typically the technique of choice for analyzing the cyclic loads on a wind turbine. However, the accuracy of this technique is limited by the size of bins. In particular, the cycle counts within a bin are spread across the bin. Because the damage contained within the bin, see Eq. 5, is a non-linear function of its stress level, the characterization of all the load cycles within a bin at a single level can significantly under or overestimate their damage to the structure. Several analytical techniques, based on materials properties and on the assumed distribution of the loads contained in the bin, can locate the damage centroid for the bin. However, these techniques are typically overkill. A conservative technique is to use the highest stress level for each bin as stress level for all cycles in that bin and to keep the size of each bin relatively small. *For the latter, the minimum recommended number of bins is fifty [25]*, and the expected maximum cyclic stress is typically set to fall within the 70 percent bin.[4]

4.5.4. Mean Value Bins

As discussed above, the fatigue load spectrum may be described using one of three representations: the range spectra in a column of cycle counts, a range and mean spectra in a 2-D matrix of cycle counts, and a Markov matrix of peaks and valleys in a from-to matrix. *The range-mean (2-D) cycle-count matrix is the form favored by this author for most applications*. The inclusion of the mean value in the description of each cycle count adds important information concerning the general state of stress (strain) on the component. This information can be used effectively by the linear damage models and the additional information is gained with little additional complexity.

However, this view is not shared by all. In reduced formulations (2-D to 1-D), the variation of the mean stress across cycles is replaced by a single average value in some fitting techniques and, in others, the variation is totally ignored. In an apparent contradiction to the statement in the preceding paragraph, the author has used several of the reduced formulations extensively, e.g., see section 4.3.3 “Generalized Curve Fitting Techniques” on p. 20. The use of a reduced formulation

[4] The purpose of the 70 percent value is to provide room-at-the-top of the cycle count matrix; in particular, if an unexpectedly high stress cycle occurs, it will be included accurately in the cycle count matrix. If data are preprocessed, the 70 percent value may be increased to reflect the known value of the highest stress cycle.

is supported by several observations. For most turbine load spectra, the range of mean stresses is relatively small. And, if the material properties are based on a mean stress or an R value that falls somewhere near the middle of this range, service lifetime predictions are typically close to those predicted using the mean stress information.[5] *Thus, the variation of the cycle counts with mean stress can sometimes be ignored if the material properties used in their evaluation are based on an average mean value*. However, designers should evaluate their designs and load spectra using both techniques before using one or the other, to ensure that their choice does not lead to a non-conservative estimate of the service lifetime.

4.5.5. Counting Cycles

As discussed above, the data samples forming the representative data set are formulated from relatively short samples of data that are collectively on the order of several hours in duration. Typically, the duration of each segment is 10 minutes. These segments are counted as series of independent segments or concatenated into a single file for counting. As pointed out in Kelley and Sutherland [62] and Mouzakis and Morfiadakis [80], the two techniques can produce significantly different service lifetime predictions because the closeout cycles may not be matched correctly and the low-occurrence cycles may be missed entirely. Mouzakis and Morfiadakis [80] demonstrate that the service lifetime predictions based on segmented data can underestimate damage by over 40 percent for materials with large fatigue exponents. For smaller material exponents, the effects are less dramatic. Using time-series data that was divided into 10-minute segments, they compared predicted service lifetimes with and without closeout and low-occurrence cycles. Their results are shown in Fig. 17. For this figure, the time-series data were counted first in segments without closing the half-cycles. The resulting damage calculation yielded the reference service lifetime. The data were then re-counted in segments with the half cycles included in the count. The resulting service lifetime is compared to the reference service lifetime in the plots labeled "Half Cycles" in the figure. The data were recounted a final time with all of the time-series data concatenated into a single file. Half cycles

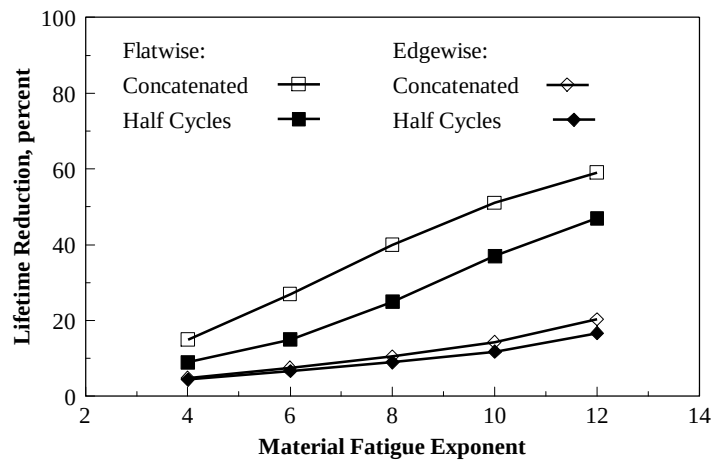

Figure 17. Effect of Segmented Data on the Prediction of Service Lifetimes.

[5] As discussed in detail below, the fatigue properties of typical wind turbine materials are significantly more dependent on the alternating stress level than on the mean stress level.

were included in this count as well. This resulting damage yielded plots labeled "Concatenated" in the figure. *Thus, when the representative data set is segmented, the sets should be counted as a single, continuous record*. This discussion is continued in section 4.6.2 "Transition Cycles" on p. 33 where the cycles between operational states are discussed.

4.5.6. Equivalent Fatigue Load

To describe the impact on fatigue from a spectral load distribution, the concept of an equivalent fatigue load may be used [31]. In general, the equivalent fatigue load is determined using Miner's Rule (see Eqs. 5 through 7) to determine a single, constant-rate fatigue load that will produce equivalent damage. If the equivalent cyclic load F(•) has a mean stress level of $(\sigma_m)_e$, and an alternating level of $(\sigma_a)_e$, then:

$$\frac{F\left[(\sigma_m)_e\,,\,(\sigma_a)_e\right] f_0}{N\left[(\sigma_m)_e\,,\,(\sigma_a)_e\right]} = \int \int_0 \frac{n(\sigma_m\,,\,\sigma_a)}{N(\sigma_m\,,\,\sigma_a)}\, d\sigma_a\, d\sigma_m \quad , \tag{25}$$

where f_o is the cyclic rate for F(•) and N(•) is the number of cycles to failure at the specified mean and alternating stress level, see Eq. 9. In the absence of actual cycle counts, the frequency f_o may be taken to be 1 p (i.e., the blade rotation rate) for the edgewise bending moments and 3 p for flapwise bending moments of three-bladed machines and 2 p for two-bladed machines. F(•) is not unique. Typically, the mean value $(\sigma_m)_e$ is chosen and then $(\sigma_a)_e$ is calculated.

Obviously, this equivalent fatigue load is material dependent. As discussed in section 5 "Material Properties" starting on p. 41, this formulation may take one of several forms. For power law formulations, see Eq. 31, with a constant mean stress, Eq. 25 may be written in the form:

$$(\sigma_a)_e = \left[\frac{\sum_i (\sigma_a)^m\, n_i}{f_0\, T}\right]^{1/m} \quad , \tag{26}$$

where m is the fatigue exponent, and T is the total time covered by the load spectrum. Typical values for m are 3 for welded steel, 6 for extruded aluminum and 10 for fiberglass composite materials.

The equivalent fatigue load is one method used to test wind turbine components in fatigue [81]. In this simulation technique, the spectral loads on a component are replaced with a constant amplitude load cycle. This technique for simulating spectral loads significantly simplifies the experiment. Moreover, by increasing the amplitude of the equivalent fatigue load (mean and/or alternating stress level), the service lifetime of the component can be simulated in a relatively short time period. However, these simulations are predicated on the validity of the assumed damage law and a detailed understanding of material behavior.

4.6. Total Load Spectrum

The load spectrum for normal operating states is typically obtained by summing the time-scaled representative samples for each operational state of the turbine. This summation does not include the fatigue cycles from transient events and from transitions between operational states. Because these transitional states can contain high load events, they should be included in the total load spectrum for a turbine component. This section of the paper highlights these events.

4.6.1. Transient Events

Wind turbines may be subjected to a large number of transient events that can significantly reduce their service lifetime. Typical events include, but are not limited to, start-stop cycles, high-rate yaw events, hitting the teeter stops, non-operating high-wind buffeting loads, loss-of-grid shutdowns and emergency shutdowns. Transient events are turbine dependent and must be evaluated on a turbine-by-turbine basis. Some are created by inflow events, as with rapidly changing inflow direction [78], others are created by the turbine's control system [82] and others are created by starting and stopping the turbine [83]. Whatever their source, these loads can be some of the largest loads on the turbine. Therefore, *transient events should be analyzed and included in the fatigue analysis of the turbine*.

While survival loads are transient events, their extremely low rate of occurrence (probably zero for at least half of a fleet of turbines) and their very large size are not typical of the loads expected on the turbine. Therefore, *survival loads are typically not included in the fatigue analysis of wind turbines.*

4.6.2. Transition Cycles

As discussed above, the load spectra for an operating wind turbine are formulated from relatively short representative samples of data that collectively are on the order of several hours in duration. The operational states are typically considered to be independent of one another. Thus, the fatigue cycle produced by the *transition from one operational state to another* are missed when the states are added together to form the total spectrum. Larsen and Thomsen [84] conducted the initial analytical study of these cycles. In their analysis of the load cycles imposed upon turbine blades during a year of operation, the transition cycles increase the damage rate by 3 percent in materials with low fatigue exponents and by 60 percent in materials with high exponents. Two other studies on how these cycles affect predicted service lifetimes have been conducted. Kelley and Sutherland [62] have shown in their analytical study that the transition cycles are insignificant. And, Mouzakis and Morfiadakis [80] in their analysis of experimental data indicate that these loads increase damage by approximately 10 percent for low material exponents and by 70 percent for high material exponents. The transition cycles between normal operational states of the turbine are commonly called ground cycles.

Ground cycles are difficult to determine. However, they can be determined either analytically [62 and 84] or experimentally [62, 80]. In both cases, the simplest solution is to count all of the data from all of the operational states together as a single record. Although simple in concept, the

technique is very difficult in practice because a large amount of data must be analyzed. Moreover, each sample must be added in proportion to its expected probability of occurrence and in its expected sequence. Larsen and Thomsen [84] have actually conducted such a simulation. In their technique, the load spectrum for the transition between operational states is predicted analytically, then long-term inflow simulations are used to predict the number of transitions between each and every two states for the life of the turbine. Their results are cited above.

Thus, if ground-cycle data are available, they should be used in the service lifetime analysis. However, because these data are difficult to obtain and predictions of service lifetimes are, at most, only marginally affected by them, we conclude that that ground cycles may be ignored in most service lifetime predictions.

4.6.3. Comment

While differences of 10 percent and 70 percent variation in the predicted service lifetimes seem high, one should remember that for many applications, uncertainties in the loads, materials and damage typically yield widely varying damage predictions. For wind turbine applications, *differences of a factor of 2 between damage predictions and measured lifetimes are not only common, they should be expected.* Once said, there are several places were these relatively small uncertainties occur, see above and below. Unfortunately, most are non-conservative and they can add to a significant result. Thus, the designer should include as many of these special-case fatigue loads in the design calculations as practically possible.

4.6.4. Summation of Load States

Once the representative samples of the load spectra have been assembled, they must be summed to estimate the lifetime of the turbine. As indicated in Eq. 11, the normal operation cyclic loads are weighted using the annual wind speed distribution and then summed to find the total operating load spectrum. The number of significant transient events is projected and then added to the operating spectrum. The result is the total load spectrum on the wind turbine.

4.6.5. Partial Safety Factors

To assure a safe design, the IEC-61400-1 standard [17] uses partial safety factors to cover the uncertainties and variabilities in the loads (and in the materials). Namely, the partial safety factors account for the possibility of unfavorable deviations of the load from the characteristic value and for uncertainties in the loading model. A discussion of partial safety factors and their application to wind turbine design is beyond the scope of this report and will not be discussed here.

4.7. Off-Axis Analysis

In most wind turbine blade analyses and experimental data sets, the loads are decomposed into two primary bending moments along the primary blade axes. The first primary moment, called the “flap” or “flatwise” bending moment, is bending out of the plane of rotation. The second, called

the "edgewise" or "lead-lag" bending moment, is bending in the plane of rotation.[6] In the initial discussions here, these loads are treated independently. However, the critical fatigue loads (stress cycles) imposed on the blade may not be along one of these primary blade axes [85, 86]. Rather, the critical loads may occur along another axis. Sutherland [85] has presented both time-domain and frequency-domain analysis techniques for determining the off-axis fatigue cycles from primary-axis loads.

4.7.1. Geometric Load Parameters

To determine the off-axis stress states in a blade section, the two principal bending stresses at that blade station may be added together vectorially, see Timoshenko [87]. Combining the stresses yields:

$$\sigma_\theta(t) \quad \rho_F \sigma_F(t)\cos(\theta) \quad \rho_E \sigma_E(t)\sin(\theta) \quad , \tag{27}$$

where σ_θ is the bending stress at time t and angle θ, σ_F is the root flapwise bending stress, σ_E is the root edgewise bending stress, and $_F$ and $_E$ are geometric correction factors. The angle θ is defined here to be the angle from the positive edgewise bending principal (neutral) axis toward the negative flapwise bending principal axis; i.e., from the tension side of the flapwise bending moment to the tension side of the edgewise bending moment, see Fig. 18. For time-series data, the time t in Eq. 27 is simply replaced by t_j, namely the jth component of the time series. The geometric factors $_F$ and $_E$ adjust the bending stress at the outer fibers of the principal axes to the bending stress at the outer fibers at the angle θ. The values for $_F$ and $_E$ are determined from:

$$\begin{aligned} (\rho_F)_\theta &= (y_o)_\theta \big/ (y_o)_F \\ (\rho_E)_\theta &= (y_o)_\theta \big/ (y_o)_E \end{aligned} \quad , \tag{28}$$

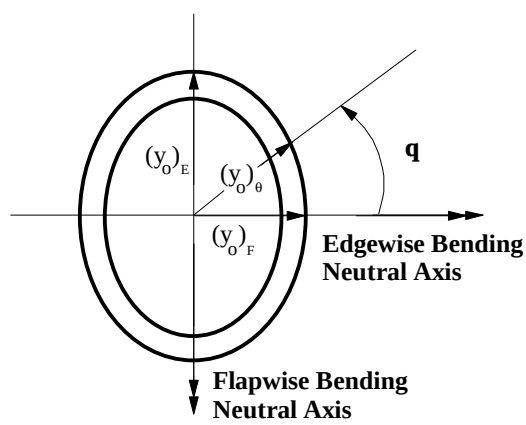

Figure 18. Geometric Parameters for an Elliptical Root Section.

where $(y_o)_\theta$ is the distance from the intersection of the principal axes to the outer fibers at angle θ, and $(y_o)_F$ and $(y_o)_E$ are the distances from the principal axis to the outer fibers along the flapwise and the edgewise axes, respectively, see Fig. 18.

[6] These definitions are not universal. For turbines with coned and/or pitch blades, the definitions of flapwise and edgewise bending moments are typically modified to be perpendicular and parallel to the chord line of the blade.

4.7.2. Typical Variations in Off-Axis Load Spectra

Using the time-series data summarized in Figs. 5 and 6, Sutherland [85] used Eq. 27 to add vectorially, point-by-point, the flapwise and edgewise loads for values of θ that ranged from 0 to 360 degrees. The resulting time series was rainflow counted to determine the load spectrum around the root of the turbine. The spectra for various angles are shown in Fig. 19.

A typical result for the range load spectrum at +45°, i.e., halfway between the tension side of the flapwise bending moment and the tension side of the edgewise bending moment, is given in Fig 19b. Similar plots for -30°, -45° and -60° are shown in Figs. 19d, e and f. The range spectra at 0° and 90° are duplicated in Figs. 19a and c to enhance the comparison of results. As seen in both

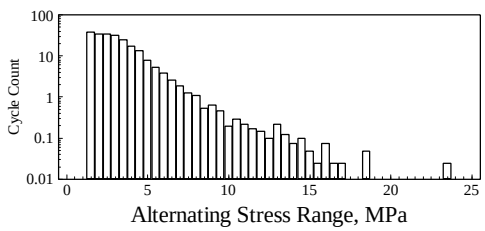

Figure 19a. Bending Stress at 0°.

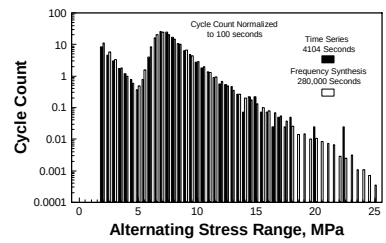

Figure 19e. Bending Stress at -45°.

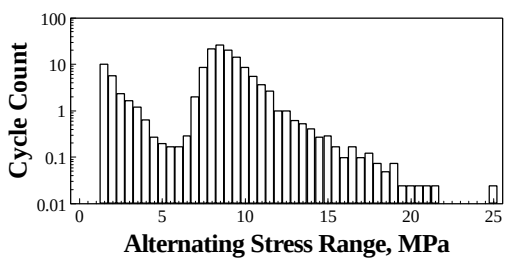

Figure 19b. Bending Stress at 45°.

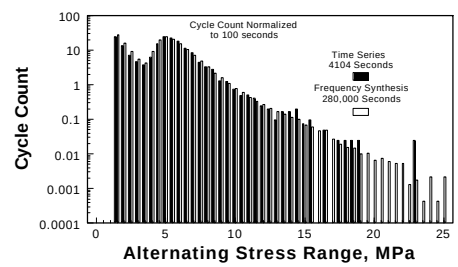

Figure 19d. Bending Stress at -30°.

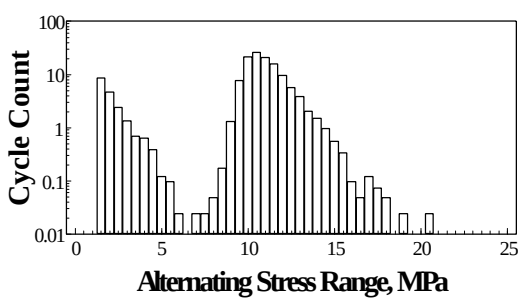

Figure 19c. Bending Stress at 90°.

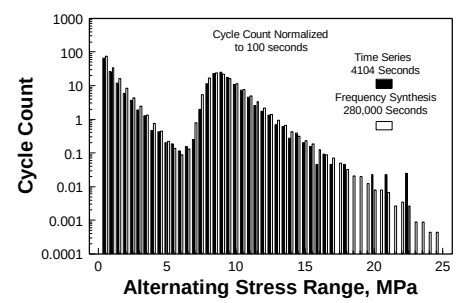

Figure 19f. Bending Stress at -60°.

Figure 19. Cycle Count Matrices for a Range of Bending Stress Directions.

figures, the typical two-hump characteristic of the edgewise-bending stress is still strong in all of the off-axis spectra. These plots are based on a frequency domain analysis proposed by Sutherland [85].

4.8. Specialized Load Spectra for Testing

4.8.1. Variable Amplitude Test Spectrum

The bulk of the fatigue testing of materials and wind turbine components is constant amplitude testing over a large variety of both compressive and tensile loads. However, wind turbines are subjected to a spectrum of loads that can significantly change their behavior; see the discussion by Veers et al. [30]. Thus, constant amplitude testing may not be characterizing their fatigue response correctly.

To determine if constant amplitude tests can be used to predict the service lifetimes of turbine components under spectral loading, specimens must be tested under spectral loads that are representative of the loads on the turbine. The European community was the first to develop a *test-load spectrum* for wind turbine components. This spectrum is called WISPER (WInd turbine reference SPEctRum) for short [88, 89]. It was designed to represent the loads on a generic turbine operating alone in flat terrain. Because the loads in these conditions are relatively mild when compared to the spectrum imposed on a wind farm turbine in mountainous terrain, a second test spectrum, the U.S. Wind Farm spectrum, was proposed by Kelley [90]. This section discusses these two variable-amplitude test spectra.

4.8.1.1. WISPER

The WISPER reference-loading spectrum was developed by an international working group composed of thirteen different European research institutes and manufacturers [88]. The objective of the effort was to specify variable-amplitude test-loading histories that model root flapwise (out-of-plane) bending of horizontal-axis wind turbine blades in the field. These features include exhibiting a spectral shape that is characteristic of the type of structure under test, while also providing the interactions thought to be important in such a stochastic environment. Great care was taken to ensure that the final loading spectra did not represent any particular turbine design or operating environment (e.g., the WISPER loads are not time correlated). These features imply that this test-load spectrum is to be used for comparative purposes only.

WISPER is derived from eight load cases that are called classes or modes. The first two classes are the loads for discrete events, specifically turbine start-up (Class 1) and stopping (Class 2). The six remaining classes, 3 through 8, are based upon 10-minute load histories obtained during continuous operation of the turbines over their operating wind speed range. Mode 3 contains representative data for mean wind speeds below 9 m/s. Modes 4 through 7 contain data for mean wind speeds of 9-11, 11-13, 13-15, and 15-17 m/s, respectively. Finally, Mode 8 describes the loads for mean wind speeds exceeding 17 m/s.

The loads in WISPER are based on a large population of load measurements from nine two-bladed and three-bladed turbines. Their rotor diameters ranged from 11.7 to 80 m. A total of 65 rainflow counted load cycle matrices (sorted by WISPER Wind Speed Class) were used to construct the WISPER spectrum. For Modes 3-8, the individual matrices from each turbine were normalized by the magnitude of the load cycle occurring once per 1000 revolutions. The normalized matrices for each wind speed class were then averaged together to reduce the influence of individual turbines. Using this approach, six normalized load cycle matrices were obtained; one each for Wind Speed Classes 3 through 8. The normalization of Operating Modes 1 and 2 (start-up/stop) was handled somewhat differently. A detailed discussion of this procedure is not warranted here.

The WISPER protocol uses the six normalized load spectra as representative samples for the operation of the turbine. The total load spectrum is obtained by adding each of these representative samples together in proportion to the number of hours the turbine will operate during a two-month period. The hours of operation used in the WISPER protocol are based on the long-term wind statistics from two different sites along the northern coast of Germany.

While WISPER offers the complete range of loads on a wind turbine (approximately 130,000 load cycles), researchers have found that its many small load cycles make testing somewhat difficult. To provide a shorter testing sequence, the low-amplitude cycles have been removed from the WISPER load spectrum to form the WISPERX load spectrum. The latter reduces the number of load cycles by approximately a factor of 10 (approximately 13,000 load cycles remain) by removing all cycles with an amplitude of level 17 or less (WISPER has a total of 64 load levels). WISPERX maintains all of the larger cycles in both tension and compression. For testing rates of 2 Hz, a WISPERX test block will require approximately 2 hours to complete, while a WISPER test block will require about 18 hours.

4.8.1.2. U.S. Wind Farm Spectrum

The U.S. wind farm spectrum was developed by Kelley [90] based on operating data obtained from two Micon 65 turbines that were tested at Row 37 of a 41-row wind farm in San Gorgonio Pass, California [91, 92]. The data set consisted of 397 10-minute records that were collected over a wide range of inflow conditions during the late wind season (late July and early August). These data were processed using the WISPER development protocol to form the load cycle matrices for Modes 3 through 7.

The U.S. wind farm spectrum does not compare directly with the WISPER spectrum because they are based on different wind speed distributions. To provide a comparison, the normalized load cycle matrices from the WISPER spectrum were combined with the San Gorgonio wind speed distribution to form an equivalent WISPER spectrum for the San Gorgonio site. The equivalent WISPER distribution is compared to the U.S. wind farm spectrum in Figure 20. As shown in this figure, the San Gorgonio spectrum has many more cycles than does WISPER. And as verified by Sutherland and Kelley [93], the former is significantly more damaging.

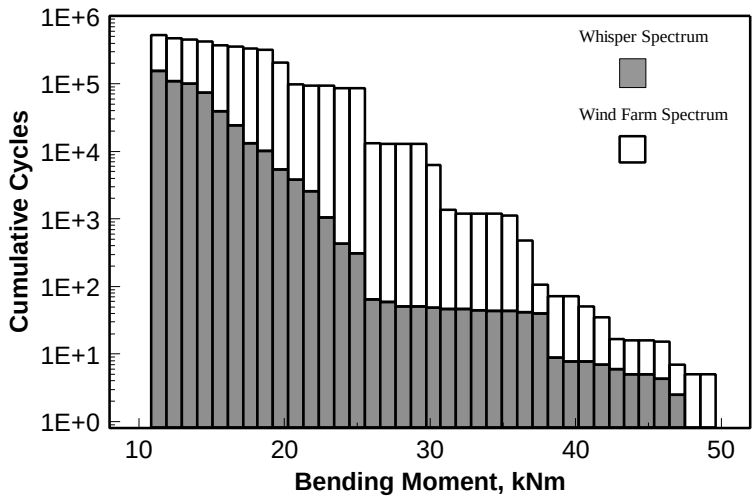

Figure 20. Cumulative 2-Month Reference Alternating Load Spectrum.

4.8.2. Load Spectra for Gears

The conventional design technique used for a non-wind generator gearbox is based on the maximum torque transmitted through the box and by the spectral content of the operational loads. The spectral content is usually characterized by a service factor. Recommended service factors for normal applications are supplied by gearbox manufactures and standardized by the American Gear Manufacturers Association (AGMA). For example, a service factor of 1.0 is recommended for relatively short duration applications involving uniform loads, as with rotary pumps for liquids. A factor of 2.0 is recommended for continuous applications involving reciprocating loads, as with cooling tower fans or beet slicers in the sugar industry. Unfortunately, the unique torque spectrum imposed upon gearboxes used in wind turbines precludes designs based upon any of the standard categories.

In a technique that is used to characterize and analyze the loads on a typical wind turbine gearbox, McNiff et al. [83] developed a "time-at-level" histogram for the loads on the gearbox. In this technique, the torque applied to the gearbox is characterized by the total time the gearbox will be subjected to a given magnitude of torque. Figure 21 presents the annual time-at-level histogram developed by

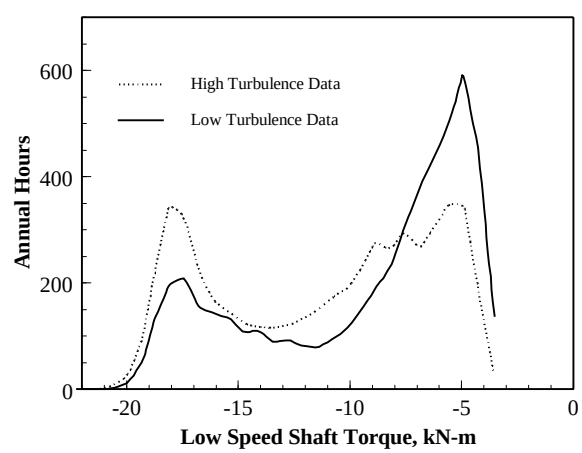

Figure 21. High and Low Turbulence Torque Spectrum for the Micon 65.

McNiff, Musial and Errichello [83] for the Micon 65 turbine. The development of these loads is based on a point-by-point binsing of the time series data by magnitude. The service lifetime analysis assumes that each torque bin is applied to the gearbox in a quasi-static manner; namely, the torque is a slowly varying function of time.[7] Thomsen and Petersen [94] conducted a similar study for both stall and pitch controlled wind turbines.

In the time-at-level technique, the torque time series is binsed by magnitude. The number of stress cycles on an average gear tooth is determined from this histogram by dividing the time in each torque bin by the duration of a tooth engagement (or, conversely, multiply by the rate of tooth engagement) and, then dividing by the number of teeth on the gear. Thus, the cycle count histograms and the time-at-torque histograms are simple multiples of one another.

The time-at-torque histogram for a Micon 65 turbine is shown in Fig. 22. As shown in this figure, the time-at-torque is a function of sample rate. Sutherland and Burwinkle [95] have demonstrated that the time-at-torque techniques yield essentially equivalent results to rainflow counting the tooth loads; namely, *for the fatigue analysis of gears, torque loads may be considered to be slowly varying functions of time*.

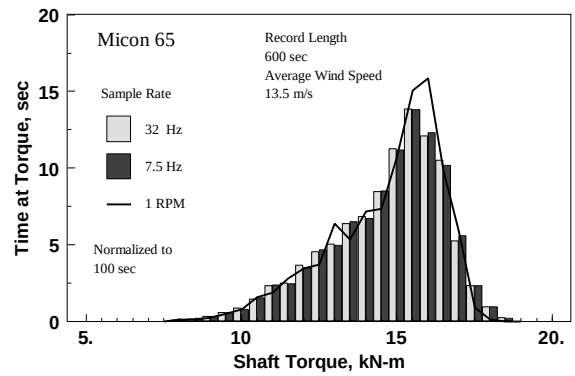

Figure22a. Linear Histogram.

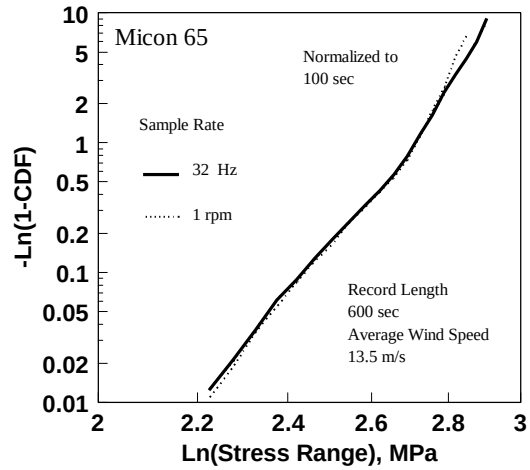

Figure 22b. Weibull Plot.

Figure 22. Time-at-Torque Histogram for the Micon 65.

A joint AGMA (American Gear Manufactures Association) and AWEA (American Wind Energy Association) committee has developed design guidelines for gearboxes used in wind turbine applications [96].

[7] A "slowly varying function of time" implies that the torque loads on the gear teeth produce a single stress cycle per each tooth engagement.

5. MATERIAL PROPERTIES

Most of the materials used in the construction of wind turbines are typical of those materials that are used in rotating machinery and towers. Thus, the turbine system is primarily composed of materials that are relatively common structural materials with extensive engineering applications and databases. However, blades are unique structural components of wind turbines. They are a minimum weight and cost component that must endure a very large number of fatigue cycles during their service lifetime. As shown in Fig. 23, blades must endure several orders of magnitude more cycles than an airplane, the original fatigue critical structure. Thus, turbine blades are also fatigue critical structures. Moreover, the cost of the materials used in the turbine must be kept at a relative minimum to ensure a commercially viable product.

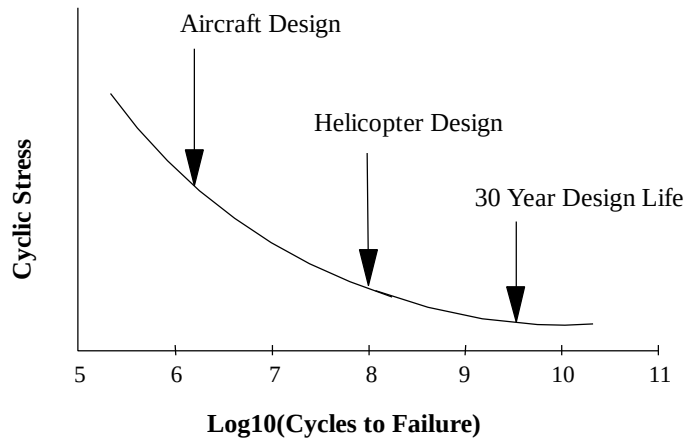

Figure 23. Schematic S-N Diagram for Various Fatigue Critical Structures.

Wind turbine blades have been made from a variety of materials that range from wood to metals to composites. Wood (a naturally occurring composite material) has proven to be a successful material. Its relatively high strength-to-weight ratio, and good stiffness and resilience yield high quality blades. Wood was used in the early windmills (including the early Dutch windmills and the U.S. water pumpers) and has remained a favorite with the designer of small and medium sized wind turbines. However, wood's inherent problems with moisture stability and joining efficiency [97] have forced designers to examine other materials. Metals were initially a popular material because they yield a low-cost blade and can be manufactured with a high degree of reliability. However, most metallic blades (steel) proved to be relatively heavy, which limits their application in commercial turbines. Lightweight metals (aluminum) have found some applications. Composites have become the blade material of choice. High strength and stiffness and the ability to tailor the material to the loads has led to its widespread use as a blade material.

The bulk of the fatigue properties developed for materials that are used in wind turbine components are based on coupon tests conducted under constant amplitude loading. The techniques used in these tests have varied widely. Swanson [98] provides a general reference for typical testing techniques. This section provides a general overview of the fatigue properties for the various wind turbine blade materials and references to fatigue databases.

5.1. Characterization of Fatigue Properties

Typically, the fatigue characteristics of materials are determined by subjecting test specimens to fatigue cycles and counting the number of cycles to failure. In constant-amplitude fatigue tests, the data are typically called S-N data, reflecting the number of cycles, N, at the stress (or strain) level S required to fail the sample. For crack propagation the data, normally called da/dn data, track the number of cycles required to extend a crack of length a by a length da. In both cases, experimental procedures lend themselves to tracking the cycles to failure as a function of the cyclic amplitude while holding the mean or R ratio constant. This testing procedure yields a family of curves that describes the fatigue behavior of the material.

The information contained in these curves is typically characterized using several standard techniques. The first and foremost is a presentation of the family of S-N curves themselves. This simple presentation can be somewhat deceiving, because various authors use various forms of S and n; see section 2 "General Fatigue Nomenclature" on p. 3. In particular, the value of S can be chosen to be the range of the cycle, the amplitude of the cycle, the maximum of the cycle (tension) or the minimum of the cycle (compression). Moreover, these values may be normalized by ultimate tensile or compressive strength. The number of cycles n is usually the number of full cycles to failure. But it can also be the number of "cross-overs" (zero-crossings) or the number of reversals (two reversals for each full cycle). *Thus, one must also be cautious with S-N data. Always check the reference to ascertain the definitions of the variables used to characterize the data.*

In addition to the presentation of the family of curves, several other graphical and mathematical descriptions of the data have proven useful. A very popular graphical technique is the constant-life Goodman Diagram, and log-linear and log-log curve fitting techniques. This section of the paper discusses several of these techniques.

5.1.1. Goodman Diagram

For design, a family of S-N curves is typically not very useful. Rather, the designer prefers constant-life curves that depict the locus of all stress states that produce a given fatigue life. These curves allow the designer to determine quickly and accurately the effect on lifetime of changes in the stress or strain in a component under design [10]. A typical Goodman diagram is illustrated in Fig. 24. In this figure, the vertical axis is a measure of the cyclic

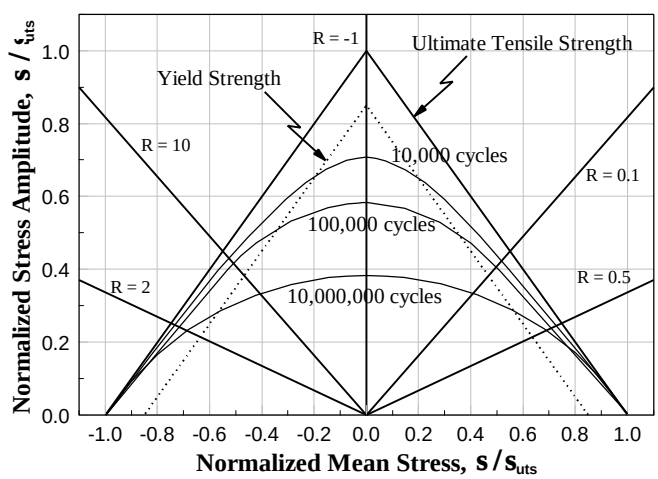

Figure 24. Typical Symmetric Goodman Diagram.

amplitude, and the horizontal axis is a measure of the mean stress. In both cases, theses stress levels have been normalized by the ultimate tensile strength of the material.

Figure 24 illustrates that a constant R ratio plots as a straight line in this diagram. All constant R ratio plots have their origin at zero mean and zero amplitude. Fully reverse bending, R = -1, is the vertical axis; i.e., the mean stress is zero.

In this figure, the constant life curves are bounded by the ultimate tensile strength of the material on the tensile side (right side) of the diagram. This stress level plots as a straight line between (0,1) and (1,0). Likewise, the ultimate compressive strength bounds the compressive side of diagram (left side). It plots between (0,1) and (-1,0). Similar straight lines are shown in the figure for the tensile and compressive yield stress. In this illustration, we assumed that the tensile and compressive strengths are equal.

Three representative constant life diagrams are shown in this figure, at 10,000, 100,000 and 10,000,000 cycles. Each constant-life plot can be constructed from a family of S-N curves. Depending on the data behind the plot, the constant-life curve may be straight-line segmented curve or a smooth fitted curve.

This diagram illustrated in Fig. 24 is called symmetric; namely the left side of the plot is the mirror image of the right side of the plot. Thus, for symmetric materials, the ultimate tensile and compressive strength must be equal, and fatigue life is dependent on the absolute value of the mean stress. For symmetric materials, only the right half of the full Goodman diagram is typically plotted. Metals are typically symmetric materials; fiberglass materials typically are not.

5.1.2. General Characterizations of Fatigue Behavior

5.1.2.1. Curve Fitting S-N Data

As discussed by many authors, the S-N behavior of composite materials at a constant R value is typically fit using one of two equations. The first is a power law of the form:

$$s = CN^{1/m} = CN^{1/k} \quad , \tag{29}$$

or alternately,

$$\log(\sigma) = \log(C) + \frac{1}{m}\log(N) \quad , \tag{30}$$

where N is the number of cycles to failure at stress level σ, and the coefficient m, sometimes denoted by k or b, is called the fatigue exponent. In this form, *the fatigue exponent is a negative number; i.e., the stress level decreases as the number of cycles increases. However, most fatigue literature reports positive fatigue exponents; namely, Eqs. 29 and 30 have been rewritten with an explicit negative sign.* Thus, these two equations become:

$$\sigma = CN^{-1/m} = CN^{-1/k} \quad , \tag{31}$$

$$\log(\sigma) = \log(C) - \frac{1}{m}\log(N) \quad . \tag{32}$$

In nondimensional form, Eq. 31 takes the form:

$$\frac{\sigma}{\sigma_o} = C\,N^{-1/m} = C\,N^{-1/k} \quad , \tag{33}$$

or

$$\log\left(\frac{\sigma}{\sigma_o}\right) = \log(C) - \frac{1}{m}\log(N) \quad , \tag{34}$$

where σ_o is the static strength of the composite. In this form, C' *has a value of 1* when the curve fit to the S-N data set passes through the static strength at 10^0 cycles, i. e., at static failure in the first fatigue cycle. However, best fits for many materials yield values for C that are typically much larger than one. Thus, a multi-segmented curve is typically required to characterize the low and high cycle fatigue behavior of composites. For wind turbine applications where design lifetimes are relatively long, this region of the curve is typically not important.

The second form is given by a log-linear function of the form:

$$\sigma = C - \frac{1}{m}\log(N) = C - b\log(N) \quad , \tag{35}$$

or alternately,

$$10^{\sigma} = CN^{-1/m} \quad , \tag{36}$$

where the inverse of m is typically denoted by b. In nondimensional form, Eq. 35 takes the following form:

$$\frac{\sigma}{\sigma_o} = C - \frac{1}{m}\log(N) = C - b\log(N) \quad . \tag{37}$$

In this form, *C' also has a value of 1* when the curve fit to the S-N data set passes through the static strength at 10^0 cycles. Best fits typically yield values of C that are very close to one.

The exponent m in Eqs. 35 and 37 is different. When a specific S-N data set is fit with these two equations, the respective fatigue exponents are comparable, but they typically will not have the same magnitude. As discussed in section 5.4.6.2 “Predicted Service Lifetime” on p. 65, fits of composite data with one of these two forms will have comparable goodness of fits. However,

when used in damage analysis for spectral loads, the two fits produce significantly different predicted lifetimes.

5.1.2.2. Goodman Fit for Mean Stress

As discussed in preceding section, the family of S-N curves may be formed into the Goodman diagram shown in Fig. 24. For many materials, the dependence of the constant-life curves on alternating and mean stress may be collapsed into a single curve using a Goodman fit [8]; i.e., the Goodman diagram is mapped into a single curve that is based on an equivalent stress level. Typically, the data are collapsed to a single, zero-mean-stress S-N curve (equivalent to R = -1).

The Goodman Fit defines the relationship between mean and alternating stress levels. This rule states that the fatigue life at alternating stress σ_a and mean stress σ_m is equal to the fatigue life at an equivalent zero-mean-stress alternating stress state of σ_e through the relation:

$$\sigma_a = \sigma_e \left[1 - \frac{\sigma_m}{\sigma_u} \right]^c \quad , \tag{38}$$

where σ_u is the ultimate strength of the material. Variations on this equation replace the ultimate strength of the material with the yield stress, or various fractions and/or combinations of the ultimate strength and yield stress. Usually the exponent c is taken to be equal to one, but other values are often used to improve the fitting characteristics. The form chosen for a particular material is usually determined using a best-fit algorithm.

5.1.2.3. Crack Propagation Model

A generalized crack propagation model was proposed by Forman et al. [99]. This formulation takes the following form:

$$\frac{da}{dn} = \frac{C\left(1 - R\right)^m \Delta K^n \left(\Delta K - \Delta K_{th}\right)^p}{\left[\left(1 - R\right) K_c - \Delta K\right]^q} \quad , \tag{39}$$

where da/dn is the crack propagation rate (see Eq. 12), ? K is the change in the stress intensity factor K at the crack tip for the nth cycle, and *C*, *m*, *n*, *p*, *q*, ? K_{th} and K_c are material constants. The equation reduces to traditional formulations via the specialized values shown in Table I. In this table, m_w is a material constant. This formulation has been fit to a selected set of materials in Forman et al. [100].

Table I. Specialized Values for the Forman Crack Growth Model.

Constitutive Relationship	Exponent		
	m	*p*	*q*
Paris	0	0	0
Forman	0	0	1
Walker	$(m_w - 1)\,n$	0	0

5.2. Wood

The *Wood Handbook* [101] is a general reference for the structural properties of solid wood. Wood is not a single material; rather, it includes many species with a wide range of mechanical properties and densities. Density variations range over an order of magnitude, from approximately 96 kg/m^3 (6 lb/ft^3) to 960 kg/m^3 (60 lb/ft^3). In general, the mechanical properties of wood, moduli and strength, are proportional to density because the basic organic material is essentially the same in all species. The design flexibility of wood is obvious. Low-density species, e.g. balsa wood, can be used as the core for sandwich panels where stiffness and buckling resistance must be accomplished with a minimum weight design. And, high-density species, e.g., Douglas fir, are used for the blade skin and structural stiffeners where high strength is essential [97].

5.2.1. General Properties

5.2.1.1. Mechanical Properties

The mechanical properties of wood are influenced significantly by a number of variables. As noted above, moisture content is the most significant. The *Wood Handbook* [101] presents a general empirical relationship that characterizes the changes in mechanical properties with moisture content. This relationship is for "clear" wood at approximately 20°C. The mechanical property P (i.e., the various anisotropic moduli and strength properties) is related to the moisture content M (in percent by weight) by the following equation:

$$P = P_{12}\left[\frac{P_{12}}{P_g}\right]^{-\left(\frac{M-12}{M_p-12}\right)} = P_{12}\left[K\right]^{-\left(\frac{M-12}{M_p-12}\right)} \quad , \tag{40}$$

where P_{12} is the property at 12 percent moisture content, M_p is the moisture content at which changes in the property first occur as the wood is dried, and P_g is the property (in the green

condition) for all wood moisture contents greater than M_p. M_p varies between 18 and 21 percent for most wood varieties. And the property P varies on the order of ± 20 percent for moduli and up to 35 percent for strength. The ratio of P_{12} and P_g, K, is a constant for a given wood and property. The adjustment of physical properties for moisture content is also covered by standards ASTM D 245 and 2915.

The mechanical properties of wood are also a function of temperature, time-at-load and sample volume. At constant moisture content and below about 150°C, mechanical properties are approximately linearly related to temperature, with the properties decreasing as the temperature increases. A change of 50°C from 20°C can produce as much as 50 percent change in modulus and, typically, a 20 or 30 percent change in strength. Time at load can increase strain by approximately 100 percent in a year's time, and decrease strength by 50 percent relative to properties determined in short-term tests.

5.2.1.2. Grading

Wood is a natural material. Thus, natural variations within a given species are common and are important to the design of structures made from wood. To obtain a consistent set of mechanical properties, wood is typically graded by visual inspection. This qualitative measure of the grain structure in a given piece (batch) of wood has proven to be a good indicator of the quality of its mechanical properties. The *Wood Handbook* [101] provides a detailed description of a typical visual grading system.

A quantitative grading system for grading veneer sheets was developed by Jung [102, 103]. In this system, an acoustic wave (a 50 kHz wave was used in these studies) is passed along the length of the sheet [2.44 m (8 ft.)]. The transit time is then used to estimate the quality of veneer sheet. While the transit time is primarily a function of sheet's modulus, this measurement also reflects grain slope and knots, which can significantly reduce the quality of a veneer sheet. Gougeon Brothers, Inc. [97] has used this system successfully for grading the veneers they use in the construction of their laminated wood blades.

5.2.2. Laminated Wood

The techniques for manufacturing wooden wind turbine blades were drawn from the aircraft and boating industries. The process uses a laminated wood manufacturing technique to create a wood composite from sheet veneers [approximately 2.5 mm (0.1 in) thick] and epoxy. This process is quite similar to that used for building hand-layup fiberglass composites structures. Wood veneers are first cut to size and then wetted with epoxy. They are then placed into a female mold. During the layup process, particular attention must be paid to the alignment of each sheet to ensure that the intra-layer joints are properly aligned. And, to ensure that the sheets lay flat in the mold, the curvature of each sheet is typically limited to a single axis of curvature. The entire stack of veneers are then cured as a single block that is typically vacuum bagged to remove excess air and to apply a uniform pressure to the stack as the bond is cured. In wind turbine applications, the resulting laminate is approximately 20 percent resin. This relatively high resin ratio is used to seal

all the veneer's surfaces, thus controlling moisture, and to fill the voids and gaps that are typical of this relatively low-pressure manufacturing process [97].

Although rather simplistic in concept, the design of a laminate structure is particularly complex in practice. Namely, the manufacturing process requires that each sheet be cut and trimmed to a shape that will fit precisely into the complex geometry of the mold. The shape of each piece of veneer is dictated by a number of considerations. First, each piece must lay properly in the veneer stack, i.e., the veneer's stiffness essentially restricts each piece to a single axis of curvature. Second, the inter-layer joints between pieces of veneer must be precisely aligned to ensure high-strength, fatigue-resistant joints. And, third, the joints must be staggered between the various layers to ensure that the final stack does not have joints occurring so close to one another that the structural integrity of the stack is compromised. Thus, sizing each piece of veneer becomes a difficult task in conformal geometry.

5.2.2.1. Moisture Content

The effects of moisture on a laminate-wood structure can be deduced by modifying Eq. 40 [97]. For a weight fraction of epoxy that is given by ω_E, the moisture content of the wood is given by:

$$M = \left(1 + w_E\right) M_L \quad , \tag{41}$$

where M_L is the moisture content of laminate. Thus, Eq. 40 becomes:

$$P = P_{12} \left[\frac{P_{12}}{P_g} \right]^{-\left(\frac{(1+w_E)M_L - 12}{M_p - 12} \right)} = P_{12} \left[K\right]^{-\left(\frac{(1+w_E)M_L - 12}{M_p - 12} \right)} \quad . \tag{42}$$

The parameters contained in these two equations are described in the discussion of Eq. 40.

5.2.2.2. Attachments

As with most blades, the attachment of the blade root to the hub is critical to a reliable blade design. For wood blades, a bonded stud system has proven to be quite successful, see the discussion in section 8.2.3 "Bolted Studs" on p. 96.

5.2.3. Laminated Douglas Fir

In the U.S., laminated Douglas fir is the wood of choice for wood blades. Spera et al. [97] have characterized this material.

5.2.3.1. Moisture Content

The effect of moisture content on the mechanical properties of a laminated structure may be characterized using Eq. 42. In this equation, M_p equals 24 percent for Douglas fir, ω_E equals 0.22 and various values of the parameter K are summarized in Table II.

Table II. Typical Mechanical Property Ratios for Laminated Douglas Fir.

Property	K Values Used in Eq. 42.
Static tension parallel to grain	1.21*
Static tension perpendicular to grain	1.13*
Static compression parallel to grain	1.92*
Static compression perpendicular to grain	1.50
Static shear parallel to grain	1.07
Modulus of elasticity parallel to grain	1.05
Tension-tension fatigue parallel to grain	1.21
Compression-compression fatigue parallel to grain	1.92
Tension-compression fatigue parallel to grain	1.57

*Properties of clear Douglas fir [101].

5.2.3.2. Fatigue Properties

A typical set of fatigue results of this study is shown in Fig. 25. Three important features in the fatigue design of these laminate structures are illustrated in this figure: grade, joint structure and size.

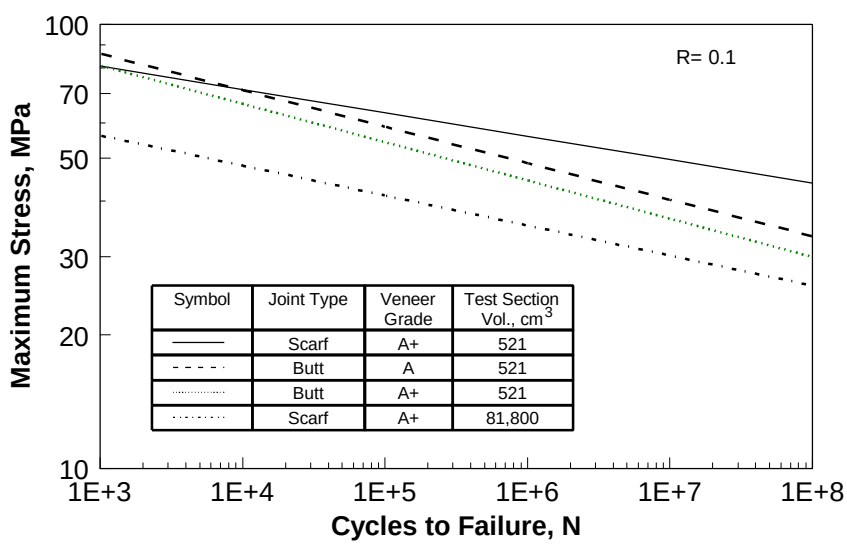

Figure 25. S-N Diagram for Douglas Fir/Epoxy Laminate.

Grade: As illustrated in Fig. 25, the grade of the veneer does not imply consistent structural performance. In this case, a grade A veneer outperforms a grade A+ veneer.

From a structural standpoint, the grading system quantifies the straightness of grain (grain distortions). As discussed above, the veneer can be graded either visually or mechanically. The acoustic technique provides a quantitative measure of the veneer's mechanical properties (modulus) and has proven to be the most consistent technique for grading veneers for wind turbine applications. This technique, to the extent possible, ensures a consistent structural grading of the quasi-static properties of the veneer coming into their process line, but not its dynamic (fatigue) properties. Thus, *the designer must always remember that wood is a natural material and can have subtle variations in properties that can only be detected with destructive testing.*

Joint Structure: The second effect illustrated in Fig. 25 concerns how two pieces of veneer in the same laminate layer are joined together. In this comparison, two internal joints are examined. In the first, called a butt joint, the edges of both veneers are square and they are simply butted up next to one another. In the second, called a scarf joint, the edges are tapered with complementary angles that permit the veneers to overlay one another in the joint.

Figure 25 illustrates that a scarf joint decreases the static and the low-cycle fatigue strength of a laminate structure. This measurement is in direct contradiction to what engineering judgment would indicate. Namely, the increased surface area in the joint created in the scarf does not translate into an increase in strength and fatigue resistance. In retrospect, several possibilities may be the cause of this reduced strength. The first is that the larger area of the scarf allows the veneer to out-gas during the layup process. Thus, the bond in the joint would contain a larger number of voids and significantly degrade the bond. Another possibility is that the joint is not aligned properly, which creates a thickness variation in the stack, namely the layer thickness is increased if the veneers are too close together (too much overlap) and is decreased when the veneers are too far apart (too little overlap). And, the thickness of the bond line will also be changed accordingly. At this time, the cause(s) of the reduced static strength and low-cycle fatigue resistance is unknown. These data also illustrate that high-cycle fatigue strength is increased by the scarf joint.

Size effects: As shown in this figure, wood, as with most natural materials, is subject to decrease in properties with increasing size. For the scarf joint, data from two sizes of samples are compared. In the first, the sample volume is 521 cm^3 (31.8 in^3) and in the second, it is 81,804 cm^3 (4992 in^3). Thus, the specimen volume has been increased by over two orders of magnitude. The data illustrate that the strength is decreased by approximately 20 percent from the first to the second. The size effect for the laminate strength σ_u may be characterized using:

$$s_u = A V^{-B} + C \quad , \tag{43}$$

where V is the volume and A, B, and C are empirical constants. For the tensile strength of laminated Douglas fir, the values of these constants are 126 MPa (18300 psi), 0.320, and 56.2 MPa (8150 psi), respectively. The volume effect is typically less in compression than in tension.

5.2.3.3. Goodman Diagram

The data contained in Fig. 25 and other data can be combined to form a Goodman diagram for the Douglas fir/epoxy laminate. Rather than show the entire diagram here, the partial diagram for 10^7 cycles is shown in Fig. 26. As shown in this figure, the diagram is approximately symmetric and, at 10^7 cycles, the scarf joint outperforms the butt joint. All of these data are for 521 cm^3 (31.8 in^3) test sections, a test temperature of 21°C (70°F) and the moisture content normalized to 6 percent.

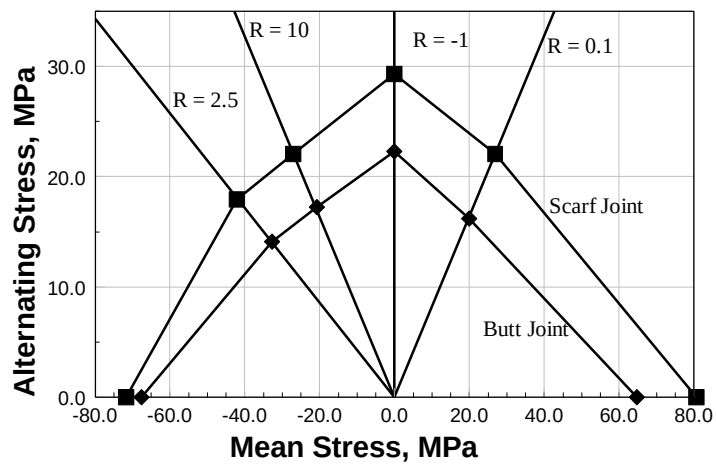

Figure 26. Goodman Diagram at 10^7 Cycles for Douglas Fir/Epoxy Laminate.

5.2.4. Other Wood Laminates

Douglas fir is the material of choice for U.S. companies. However, other woods have been chosen and used successfully by other companies. Some of the woods that have been investigated include Khaya ivorensis (an African mahogany) [104], Swedish spruce and birch plywood [105], Sitka spruce [106] and Baltic pine, popular, beech birch [107].

5.3. Metals

Metals are the primary class of materials used to construct wind turbines. With the exception of the blades, most major components are constructed with ferrous alloys (primarily steel). Ferrous materials are favored by designers because there is extensive design experience with these materials from the rotating machine industry, they are relatively cheap to purchase and machine, and they can be fabricated easily using conventional practices. Moreover, they typically have a fatigue limit that permits the designer to design the turbine component to a stress level that essentially precludes failure in unjointed material.

In the early years of windmills and in the initial designs of modern wind turbines [1, 2], most blades were constructed exclusive from metals. The modern turbine has forced turbine designers away from the relatively heavy metallic designs. Rather, they use composite materials to achieve the relatively lightweight designs that typify modern wind turbines. However, metallic alloys are the materials of choice for making strong, reliable bolted joints. Thus, most current blade designs transition to aluminum or steel at the hub joint, debatably the most important joint in the entire turbine assembly.

From a material standpoint, this class of materials has been studied and extensively documented; e g., see Fuchs and Stephens [11], Forman [100], Boyer and Gall [108], *Aluminum Standard and Data* [109], and Boyer [110, 111].

5.3.1. Steel

Most of a wind turbine's structural components are constructed from ferrous alloys that are typically a variety of steel. From a fatigue standpoint, the drivers in the design of these materials are the joint structures used to combine the subcomponents of the wind turbine into its final structure. Joints, both mechanical and welded, create high stress concentrations [112], introduce flaws and/or leave residual stresses that lead to failure [113].

Discussions of these mechanisms are outside the realm of this report and are not discussed here. However, they are extremely important to building a reliable wind turbine and should not be overlooked in the design process.

5.3.2. Aluminum

The use of aluminum in wind turbine blades is an outgrowth of vertical-axis wind turbine (VAWT) technology. In this class of turbines, the blades do not require the twisted and tapered sections of HAWTs to achieve relatively high aerodynamic efficiencies. Moreover, through the use of extrusion technology, VAWT aluminum blades can be constructed quickly and relatively inexpensively [114]. Additional innovations in the manufacturing process also allow some variations in the aerodynamic cross sections of the blade through step tapering [115]. For these applications, the material of choice is 6063-T5 aluminum.

5.3.2.1. S-N Data Base

General properties for aluminum are provided in *Aluminum Standard and Data* [109] and Boyer [110, 111].

VanDenAvyle and Sutherland [116] have developed a specialized database for extruded 6063-T5 aluminum. 6063-T5 aluminum had a measured yield stress of 205 MPa (29.7 ksi) and a measured ultimate stress of 244 MPa (35.4 ksi). The fatigue database for this material contains approximately 100 fatigue data points obtained from bend specimens cycled at five alternating stress amplitudes and at four mean stress levels. The samples were tested to a maximum of 5×10^8 (500,000,000) cycles.

When the S-N data are mapped into the equivalent stress state using the Goodman rule, see Eq. 38, there are two distinct regions to the curve, see Fig. 27. Each segment may be fit with a straight line on a log-log plot of the form shown in Eq. 37; namely,

$$\log_{10}\left[\sigma_e\right] = C + b \log_{10}[n] \quad . \tag{44}$$

This segmented curve fit is shown in the figure as a solid line (labeled least squares curve fit). The respective confidence limits on the data, based on a statistical analysis for a Weibull fit to the variations about the least-squares fit, are also shown in the figure.

The aluminum data presented in Fig. 27 indicate that the aluminum has an apparent fatigue limit or at least a significant change in the slope of its S-N curve near 10^7 cycles. This break in the curve is particularly significant for characterizing the fatigue properties of aluminum for wind turbine applications.

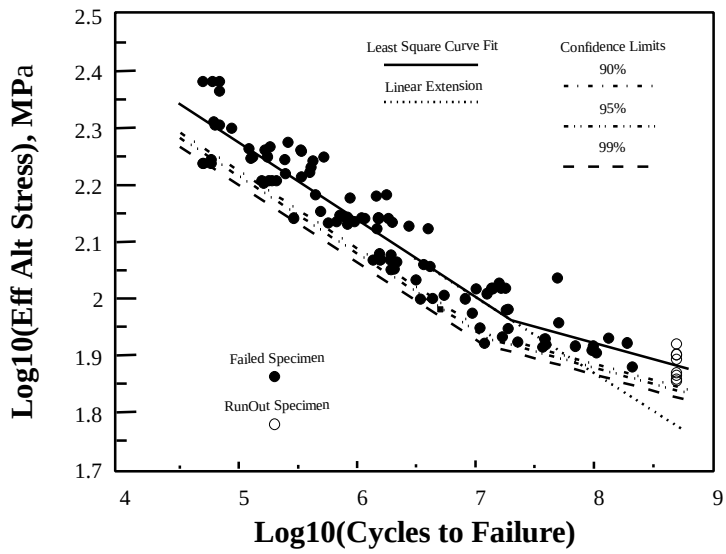

Figure 27. Normalized S-N Diagram for 6063-T5 Aluminum.

5.3.2.2. Spectral Loading

As noted above, typical S-N data are based on constant amplitude tests. The data plotted in Fig. 27 are no exception. As discussed by Mitchell [117], if the aluminum specimens had been based on spectral loads instead of constant amplitude loads, the observed break in the data would probably disappear and the S-N data would follow a linear extension of the initial slope of the curve. This extension to the least-squares fit is shown in Fig. 27 as the short-dash line. Mitchell's argument is based on a crack-propagation view of the process. Under both classes of loading, a plastically deformed region surrounds the crack tip. Under high-stress constant-amplitude testing, each cycle is strong enough to overcome the residual stress field and, thereby, open and propagate the crack. However, under relative low-stress testing, the residual stresses restrict the crack opening displacement, and thereby, significantly reduce the growth rate of the crack. When spectral loads are applied, the relatively large components of the load spectra drive the crack into virgin material with little or no residual stresses. Thus, the crack growth rate is not restrained under low-stress loads, and the crack grows at the high stress rate.

Ashwill et al. [57] have investigated the influence of this extension on the fatigue life of a Sandia 34-m Test Bed [39]. In those calculations, the linear extension is shown to have little effect on the predicted service lifetime of this turbine. As noted in section 4.4.1 "Minimum Data Requirements" on p. 24, the fatigue exponent for metals (i.e., the reciprocal of b in Eq. 44) is typically relatively small, and the damage to the structure is governed primarily by the main body of the fatigue-load distribution. As the stress levels on this turbine are primarily above the stress

threshold, see Fig. 27, the low stress region is of minor importance in the prediction of service lifetimes for this turbine, i.e., these cycles do not count when lifetimes are relatively short.

As with all designs, the finding that this region is not important for the prediction of service lifetimes in the Test Bed should only serve as a guide. In other turbines, this extension may be significant. *Thus, to remain conservative in the fatigue design of a turbine, the linear extension should be examined during the fatigue analysis of the turbine.*

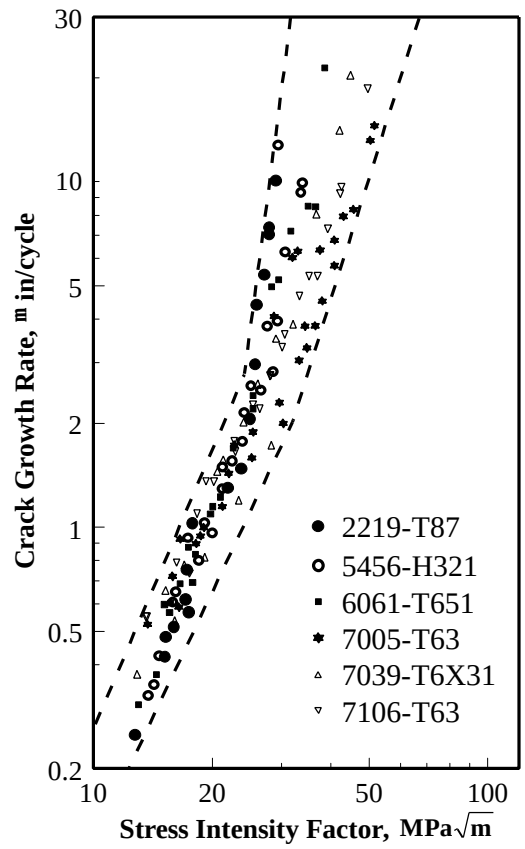

Figure 28. Fracture Mechanics Characterization for Aluminum Alloys.

5.3.2.3. Linear Crack Propagation Data Base

In addition to the development of S-N data, da/dn crack propagation curves have been developed for aluminum. Rolfe and Barsom [118] reported the general crack propagation properties of aluminum. The properties of 6063 aluminum are reported in Van Den Avyle and Sutherland [116], Hatch, Van Den Avyle and Laing [119] and Warren and Pelloux [120].

Sutherland and Schluter [20] have investigated this analysis technique to predict crack propagation in an aluminum blade on the 34-m test Bed Turbine [39]. In this analysis, the crack growth rate for aluminum was taken to be the generalized form developed by Rolfe and Barsom [118], see Fig. 28. Starting from a rather small crack of 0.025 mm (0.001 in), the crack will grow to critical length (essentially infinite growth rate) in less than 6 months, see Fig. 29. *Thus, this linear fracture analysis suggests that the service lifetime of this aluminum blade is relatively short once a crack is present.*

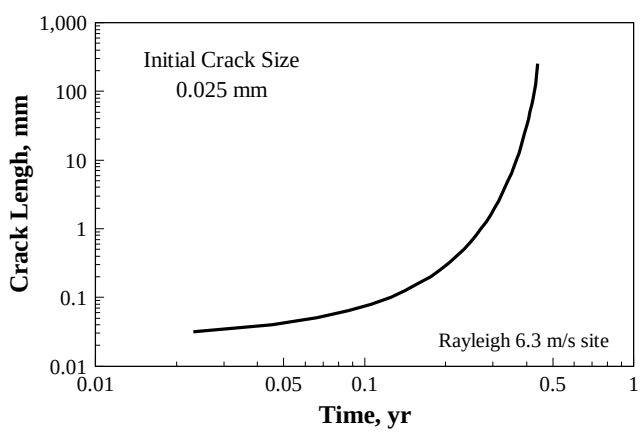

Figure 29. Crack Growth in an Aluminum Blade.

Veers and Van Den Avyle [121] have investigated the application of the constant amplitude data to spectral loading conditions. Using the constant amplitude data obtained by Van Den Avyle and Sutherland [116], the behavior of 6065-T5 aluminum is characterized using Eq. 39 with the constants *m*, *p* and *q* set equal to zero. Predictions based on this model are then compared to crack propagation data obtained under spectral loads. They find that linear models yield predictions that are not conservative for this material.

5.3.3. Gears

The AGMA has developed material properties and design practices for typical gear materials [122, 123]. A typical S-N diagram used by the AGMA for alloy steels case carburized to Rockwell C (R_c) 58-63 case hardness and 30-42 core hardness is shown in Fig. 30. The break in the curve, at approximately $2x10^6$ cycles in Fig. 30, is representative of a fatigue or endurance limit. The slope of the curve after the break is a 34.5 MPa (5 ksi) drop between $2x10^6$ to 10^8 cycles (see the discussion directly above). Additional S-N diagrams for gear materials are available in the literature and directly from gear manufacturers (proprietary data).

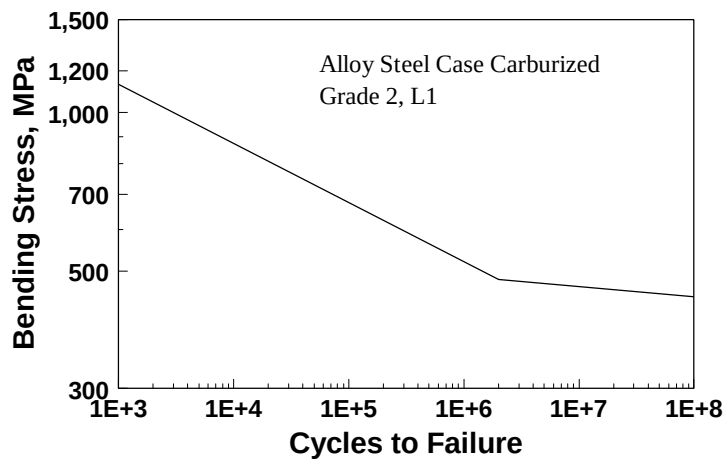

Figure 30. S-N Diagram for Carbonized Steel Gears.

5.4. Fiberglass Composites

Composites constructed with fiberglass reinforcements are currently the blade materials of choice for wind turbine blades. This class of materials is called simply fiberglass composites or fiber reinforced plastics (FRP). In turbine designs, they are usually composed of E-glass in a polyester, vinyl ester or epoxy matrix. Blades are typically produced using hand-layup techniques, but recent advances in RTM (Resin Transfer Molding) and pultrusion technology have blade manufacturers examining new procedures for increasing the quality of the final product and reducing manufacturing costs.

General references on designing with composite materials are provided in *Composites, Engineered Materials Handbook* [124] and Tsai and Hahn [125]. Mayer [126] describes the use of fiberglass composites for the design of wind turbine blades.

5.4.1. Databases

There are two main fiberglass composite databases for wind turbine applications. The first is the DOE/MSU database that has been developed in the U.S. by Mandell and Samborsky [127], and the second is the European database. The latter is the compilation of the work of many researchers, that has been compiled as the FACT database by de Smet and Bach [128] and the recent compilation by Kensche [16]. The European database is best characterized as the study of a few materials in great depth, and the former is best characterized as a study of many materials in not as much depth. Here, the DOE/MSU database will be used to illustrate data trends and the European database will be used to bring out the details that are important to the fatigue design of a wind turbine blade.

5.4.1.1. DOE/MSU

The DOE/MSU database was developed by Mandell et al. in a series of papers [127, 129-137]. This database for E-glass composites contains over 4500 data points for 130 material systems. A high frequency database provides a significant data set for unidirectional composites to 10^8 cycles. Most of the data are presented in terms of maximum initial strain measured in the early stages of the test. The database explores such material parameters as reinforcement fabric architecture, fiber content, matrix materials and loading parameters (R values).

5.4.1.2. European Database

The European database is a compilation of data from many research groups. Most of these data was collected under the auspices of the European Commission (EC). The objective of the EC's program was to develop the basic information required to set design limits for rotor blades constructed with Glass Fiber Reinforced Plastics (GFRP). The compilation of these data is the FACT database [128]. A complete collection of the database, an evaluation of results and a detailed list of the references are provided in Kensche [16]. Only selected references from this database are discussed here.

5.4.2. Trend Analysis

As discussed by van Delft et al. [138] and used by many other authors, the S-N behavior of composite materials at a constant R value is typically described using either Eq. 34 or 37. Typically, Eq. 37 has been used to characterize the DOE/MSU database [127]. The European database is typically fit with Eq. 34, [128, 138].

Equation 37 was chosen to characterize the DOE/MSU database because the fit yields a value for C that is very close to 1. As discussed below, this property is extremely important when characterizing composite data, because normalization to the static strength may then be used to eliminate batch-to-batch material variation in the fatigue data.

The formulation shown in Eq. 37 has led to the *"ten percent" rule* that is typically used as a general rule-of-thumb for the tensile fatigue behavior ($R \cong 0.1$) of uniaxial composites [139].

Namely, the fatigue strength of the composite is reduced by ten percent by each decade of fatigue cycles, i.e., when C is one and b is one tenth (i.e., a fatigue exponent of 10). A similar rule-of-thumb for compressive fatigue behavior (R ≅ 10) reduces the compressive strength by approximately 7 to 8 percent for each decade, i.e., when C is one and b is 0.07 or 0.08. This form is typically used for composites when comparing different material systems because it normalizes out variations in the static strength. Other typical values for the fatigue exponent m are 3 for welded steel and 6 for aluminum.

Both forms of the material representation have been used extensively to fit composite fatigue data and, as discussed later, they have important implications to damage calculations for spectral data.

5.4.3. General Data Trends

A large number of data points from the DOE/MSU database are plotted in Fig. 31. These data are for fiberglass composites with at least 25 percent fiber in the loading direction tested at R = 0.1. When fit with Eq. 37, the good materials have a slope of 0.10 and the poor have a slope of 0.14. Thus, the good materials in this figure are approaching the best fatigue behavior that can be obtained for fiberglass materials in tensile fatigue (the ten percent rule for uniaxial composites at R = 0.1) [139], while the poor materials do not perform nearly as well. Indeed, the small appearing variation in the fatigue slope b produces significant differences in fatigue performance. As shown in the figure, at 20 percent of static strength, the good materials have almost 2.5 orders of magnitude longer life than the poor materials.

Figures 32 and 33 illustrate the trends for compressive and reverse fatigue. For compressive fatigue, the good materials have a slope of 0.07 and the poor materials have a slope of 0.11. For reverse fatigue, the slopes are 0.12 and 0.18, respectively.

Even when a family of laminates is tested, see Figure 34, similar behavior is observed in tension (R ≅ 0.1), with slopes of 0.10 and 0.14 for the good and poor materials, respectively.[8] Thus,

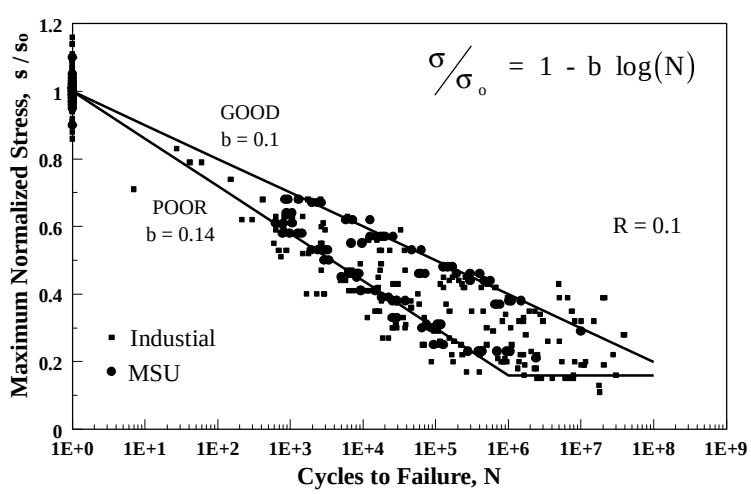

Figure 31. Extremes of Normalized S-N Tensile Fatigue Data for Fiberglass Laminates, R=0.1.

[8] In this case, the variation in properties is a direct result of varying the overall volume fraction from 31 percent for the good material to 54 percent for the poor material. This result is discussed in detail described in section 5.4.3.2 "Fiber Content" on p. 60.

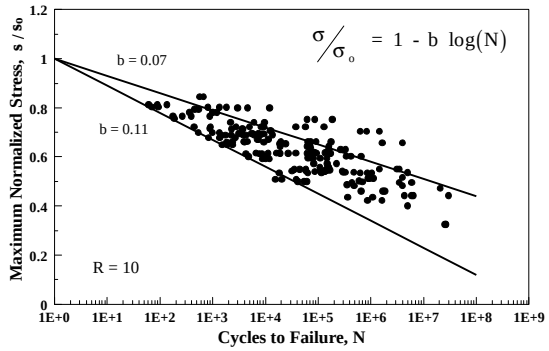

Figure 32. Extremes of Normalized S-N Compressive Fatigue Data for Fiberglass Laminates, R = 10. Normalized to the Ultimate Compressive Strength.

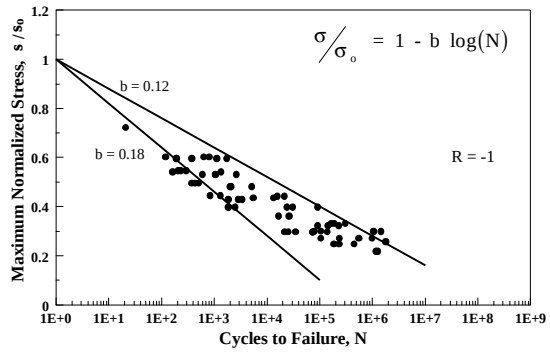

Figure 33. Extremes of Normalized S-N Reverse Fatigue Data for Fiberglass Laminates, R = -1. Normalized to the Ultimate Tensile Strength.

a major objective in the development of this database has been to sort out the differences between the good and the poor materials.

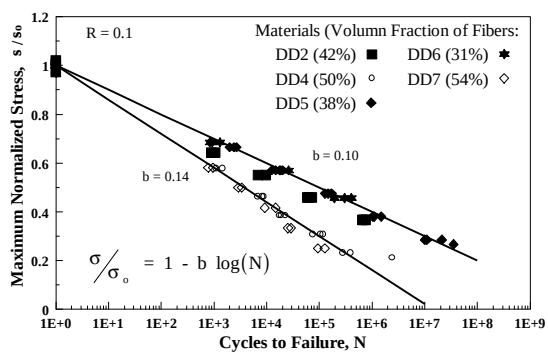

Figure 34. Extremes of Normalized S-N Fatigue Data for a Single Family of Fiberglass Laminates with 72% 0° Plies and 28% ±45° Plies, R = 0.1.

5.4.3.1. Fabric Architecture

The geometry of reinforcing fabrics plays a major role in static and fatigue properties. Woven glass-fabric composites typically show poorer tensile fatigue resistance than well-aligned, uniformly dispersed composite systems [139]. Samborsky et al. [136] give a comparison of static and fatigue properties for several types of E-glass fabric laminates with 0° plies. Ultimate tensile strength and elastic modulus are relatively insensitive to fabric type, but ultimate compressive strength is significantly lower for fabrics like A130 with a weave geometry that produces an out-of-plane curvature in the strands. Woven fabrics have about half the compressive strength of fabrics with straight strands. Mandell and Samborsky [127] note that the compressive fatigue resistance, when normalized by the ultimate compressive strength, is insensitive to fabric type or fiber content.[9]

[9] The straight-strand fabrics will also have significantly reduced compressive strength if the fibers become "wavy" during fabrication.

Typically, *the fabrics used in wind turbine application have either stitched or woven stand structures*, see Fig. 35.

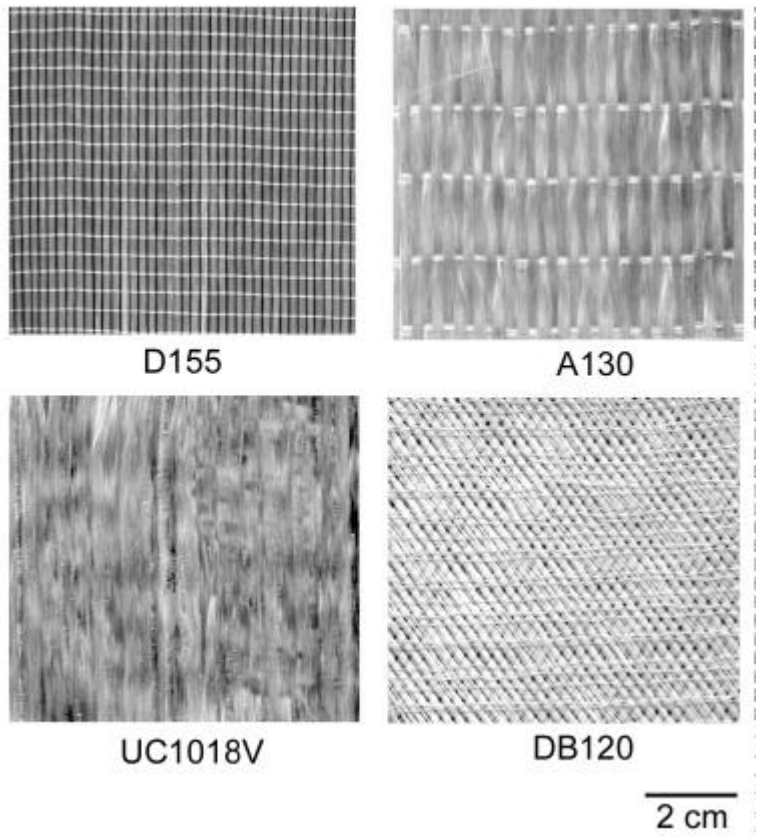

Figure 35. Dry Fabric Samples.

A material that was investigated early in the development of this database was a stitched-triax material, i.e., the material contains 0° and ±45° layers that are stitched together with organic fibers at the factory to save handling costs during blade fabrication. Two laminate constructions with the same triax fabric were studied. The first had a 35 percent volume fraction of fibers and the second had a 40 percent volume fraction. Both laminates, called Material AA in the database [127], behaved uniformly in the poor category, as did many other types of triax fabrics [127]. They are very important in this study because they provide an understanding of the basic difference between the best and worst materials in the entire database.

The essence of the results is that when the stitching is removed, the unstitched-triax behaves as one of the best materials. This observation is also true for an equivalent laminate (same layup schedule) constructed from unstitched 0° and ±45° layers. This result was explained with the aid of a detailed finite element analysis (FEA) of the local fiber stress in the composite near off-axis matrix cracks [129, 131, 135]. As the composite is loaded in tension, the matrix in the off-axis (45°) layers cracks (these cracks start forming at stress levels that are relatively low when compared to the static strength of the laminate). The FEA analysis of one of these cracked regions demonstrates that a local stress concentration factor of approximately 2.5 is generated in the 0° strands at the crossing of a 0° and a 45° layer. This large stress concentration is a direct result of the construction techniques used in the triax material. Namely, the organic fibers that are used to tie the various layers of the laminate together hold the glass fibers very close to one another, essentially touching. Under normal separation (obtained by not stitching the 0° and ±45° layers together), the stress concentration is approximately 1.4 to 1.7. Thus, the large local stresses produce early failure and uniformly poor fatigue behavior in the stitched triax material.

5.4.3.2. Fiber Content

The implication of the previous discussion is that behavior of composite systems will, in general, degrade as fiber content, is increased [127]. In earlier work, Mandell [139] found that many woven glass-fabric composites show poorer tensile fatigue resistance than the well-aligned, uniformly dispersed systems. Fig. 36 illustrates this behavior in several materials for fiber content, by volume, between approximately 30 and 60 percent. The materials cited in this figure are both cross-plied composite laminates, $[0/\pm45/0]_s$, (Materials AA and DD) and uniaxial laminates (Materials A130 and D155). As illustrated in Fig. 36a, material AA (stitched triax plies) has uniformly poor behavior, but when the separate, unstitched 0° and ±45° layers are used, there is a transition from good to poor behavior that begins at an approximate fiber content of 35 percent (see Fig. 34). Note once again that the main difference between the AA triax and the DD laminate is that the 0° and ±45° layers in the AA material are stitched together.

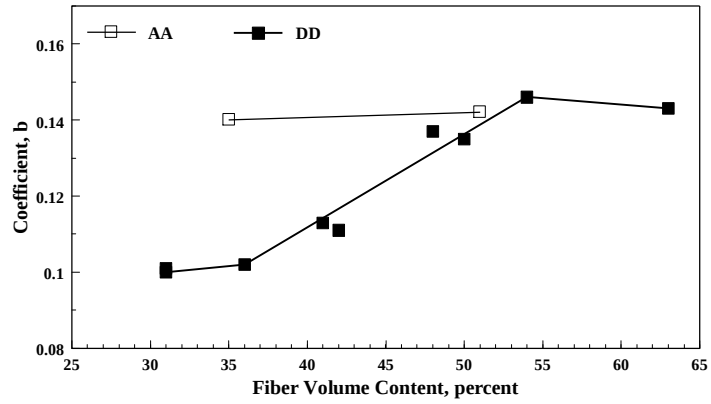

Figure 36a. Fatigue Sensitivity Coefficient for Various Fiber Contents in Fiberglass Laminates with 0° and ±45° Plies.

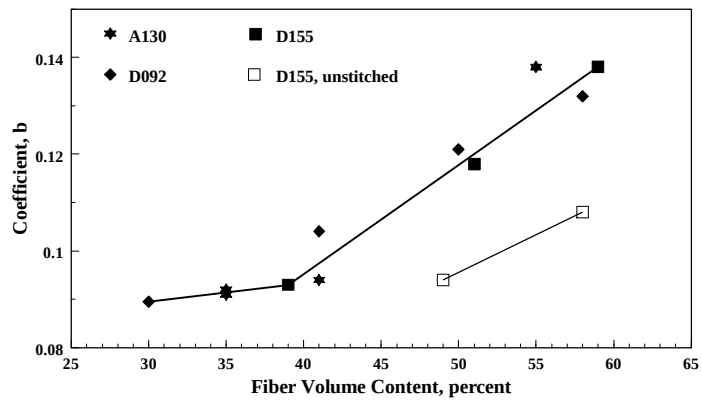

Figure 36b. Fatigue Sensitivity Coefficient for Unidirectional Fiberglass Laminates.

Figure 36. Fatigue Sensitivity Coefficient for Fiberglass Laminates as a Function of Fiber Content, at R = 0.1.

Similar data for unidirectional materials are shown in Figure 36b. As shown by data for the A130 (woven), D092 and D155 (loosely held together with organic fibers) composites, the optimum fatigue performance is achieved with a fiber content of approximately 40 percent. Moreover, as illustrated by unstitched D155 material data, if *all stitching*, be it relatively loose or otherwise, is removed, the progression from good to poor fatigue behavior is delayed to almost 50 percent fiber volume.

As discussed above, the origin of the sharp decrease in fatigue resistance as the fiber content increases apparently lies in a transition to a condition where the laminate fails in fatigue soon after the matrix cracks, usually along the stitching or weave cross-over [127]. When 45° plies are present, poor performance is observed if the 0° plies fail soon after the ±45° plies form matrix cracks. Good performance is associated with the 0° fiber wearing-out gradually, as occurs in the testing of a single strand of material [127, 139].

Thus, the fiber separation is an important parameter for defining the fatigue behavior of composite laminate systems. And, although stitching makes fiber layers and bundles easier to handle in the manufacturing process, they degrade the fatigue behavior of the composite system.

5.4.3.3. Normalization

The above discussion uses normalized data to enable a relatively large number of laminate systems to be compared directly to one another. As the static tensile strength is approximately proportional to fiber volume fraction, the minimum fatigue coefficient b does not guarantee the optimum fatigue behavior. Rather, the increased strength offered by more fibers will offset a small amount of the decrease in the fatigue performance, depending on the design loads for the blade. However, *the strain-to-failure in fatigue is much lower (by a factor of approximately 2) for the materials with the poor behavior*.

5.4.3.4. Matrix Material

Three matrix materials are commonly used in the construction of composite blades for wind turbines. They are vinyl ester, polyester and epoxy. As reported in the DOE/MSU database [127] and the FACT database [128], the matrix material has minimal effect on the static and fatigue properties of this class of composites because typical blade materials are primarily uniaxial. The various resin systems are compared in Fig. 37. These data are for tension fatigue (R=0.1) in an unstitched $[0/\pm45/0]_s$ composite. Similar results are obtained in both compressive and reverse fatigue.

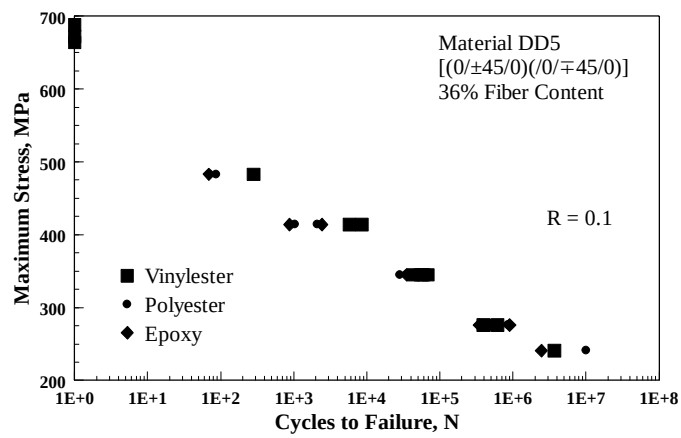

Figure 37. Effect of Matrix Material on Tensile Fatigue in a Fiberglass Laminate with 0° and ±45° Plies.

5.4.4. Modulus Changes

The composite laminates that are typically used in wind turbine blades have very low strain-to-failure in the transverse direction. This characteristic implies that matrix cracking will be present in the off-axis ±45° plies of a laminated structure long before it fails. As shown in the MSU/DOE

database [127], the transverse ply's ultimate strain-to-failure is approximately 0.24 percent. This value translates to 0.39 percent strain in ±45° plies along the 0° direction of a $[0/\pm45]_s$ laminate. At a million cycles in tensile fatigue, the strain to failure in the 45's reduces to approximately 0.14 percent strain. The early loss of the matrix function in these layers translates into a decreasing laminate modulus.

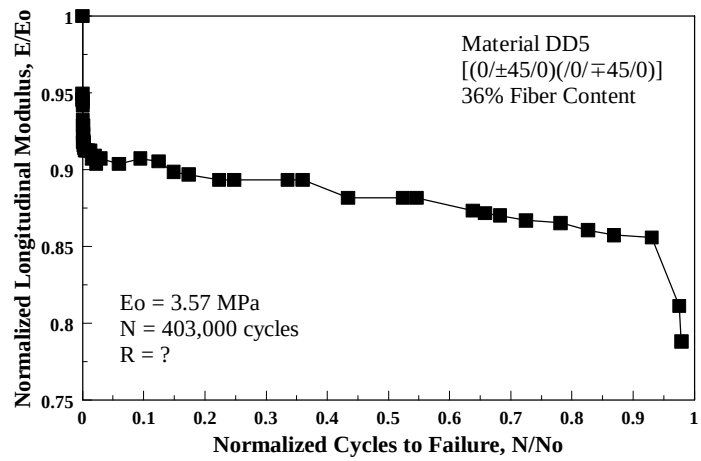

Figure 38. Reduction of Tensile Modulus in a Fiberglass Laminate with 0° and ±45° Plies Damaged in Tensile Fatigue.

Figure 38 illustrates the drop in modulus for a cross-plied composite laminate, as a function of the normalized fatigue lifetime, i.e., n/N. As shown in this figure, the longitudinal modulus drops initially by 10 to 15 percent and then remains approximately constant for most of the laminate's lifetime. As the laminate approaches failure, the modulus drops precipitously.

Mandell and Samborsky [127] used standard laminated plate theory to estimate stiffness reduction as the off-axis plies are damaged. Their results, shown in Table III, are presented as the expected drop in laminate stiffness for several composite laminates. This prediction is based on the assumption that the transverse modulus E_T and the shear modulus G_{LT} of the ±45 layers decreases to 25 percent of the original value when their matrix material cracks. The 25 percent value was derived empirically and only applies to low cycle fatigue. *When empirical data are not available, the conservative approach to predicting stiffness reduction is to delete or severely decrease the properties of the matrix-dominated, off-axis plies, i.e., assume that the off-axis plies will be fully cracked almost immediately after the blade has been put into service.* Thus, E_T and G_{LT} for the off-axis plies are reduced to zero (or a slightly positive number).

Table III. Predicted and Measured Percent Decrease in Longitudinal Modulus due to Cracking of the ±45 Plies.

Layup	Volume Fraction of Fibers, percent	Decrease in Longitudinal Modulus percent	
		Predicted	Measured
$[0/\pm45/0]_s$	38	6.2	10
$[0/\pm45]_4$	36	16	10 - 20
$[\pm45/0/\pm45]_s$	36	31	31 -42

After the initial loss of modulus, the laminate continues to lose stiffness, see Fig. 38. This reduction should not be attributed to the cracking of the ±45 layers alone. Rather, the additional reduction is due to damage accumulation in the other layers of the laminate.

Mohamadian and Graham [140] have found similar results in composites constructed with chopped mat.

5.4.5. Predicting Service Lifetimes

5.4.5.1. Industrial Materials

Sutherland and Mandell [141] have demonstrated how the MSU/DOE database may be used to predict service lifetimes for wind turbine blades. Because the high-cycle portion of the database is primarily composed of data obtained from specialized material coupons, the requisite Goodman diagram is constructed using normalized coupon data. It is then de-normalized to typical industrial laminates for the analysis of service lifetimes. The procedures described in this reference should be used to ensure the blade material used in the construction of the wind turbine is the same as the blade material being analyzed. The analysis is based on material coupons, which perform close to the good line in Fig. 31 and will be non-conservative for poor laminates.

5.4.5.2. Database Comparison

A comparison of the Goodman Diagram from the two databases is shown in Fig. 39. Of particular significance in this comparison is that the diagrams for the MSU/DOE and the European (FACT) database are very similar

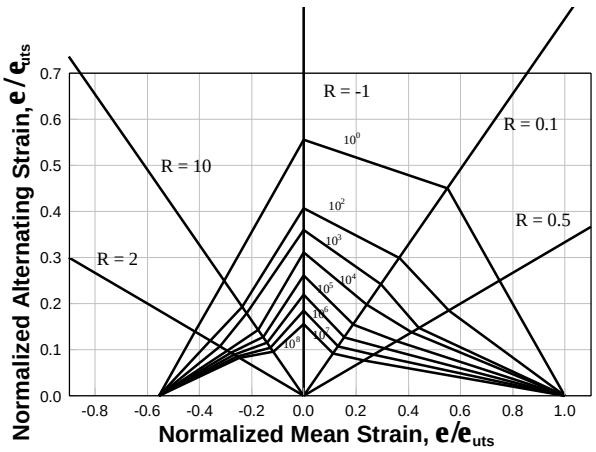

Figure 39a. Goodman Diagram based on the MSU/DOE Database.

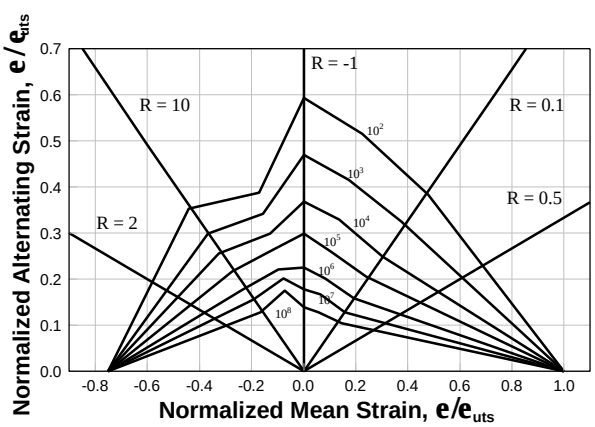

Figure 39b. Goodman Diagram Based on the FACT Database.

Figure 39. Goodman Diagrams for Fiberglass Composites.

to one another on the tension side (right side) of the diagram and very dissimilar to one another on the compression side (left side). This variation is a significant change in the form of the Goodman diagram. In particular, the MSU/DOE database yields a highly non-symmetric diagram with a strain to failure of 2.7 and 1.5 percent for tensile and compressive strengths, respectively [132]. This ratio of the tensile and compressive failure strains of 1.80 is significantly different from the European database which has a ratio of 1.33. Namely, the European database yields an approximately symmetric (about the zero mean-stress axis) Goodman diagram with strain-to-failure of 2.58 and 1.94 in tension and compression, respectively [128]. A symmetric diagram implies that there are only small differences between tensile and compressive failures.

Although they could not prove it, Sutherland and Mandell [141] suggest that the discrepancy in the compressive failure-strain reflects the difference in compressive testing techniques. In particular, the compressive tests conducted for the MSU/DOE database used gauge sections with no lateral supports, whereas, the FACT database has a preponderance of data obtained from compression tests with lateral constraints. A sample of the more recent data from the MSU/DOE database illustrates that the ratio of the ultimate tensile to the ultimate compressive strain varies from 0.94 to 2.23 with an average value of 1.50 [127]. Thus, differences in the databases can be attributed entirely to material variation. However, the differences in the testing techniques should not be discounted. Detailed comparisons of fatigue data from identical materials will be required to sort out the differences in the two databases.

When the two databases are compared on a non-normalized basis, the FACT data are found to contain a preponderance of the data that behave as the good material in the MSU database. Thus, the MSU/DOE database will predict a service lifetime that is equal to or shorter than that predicted by the FACT database.

Sutherland and Mandell [141] investigated the effect of these differences on predicted service lifetimes. Using the WISPER-protocol U.S. wind farm load spectrum (see the discussion in section 4.8.1.2 “U.S. Wind Farm Spectrum” on p. 38), the predicted service lifetimes for tensile failure were comparable (44.9 to 67.5 years based on the MSU/DOE and the FACT databases, respectively). However, for compressive failures, the predictions differed by approximately a factor of 5 (23.5 and 136 years, respectively).

5.4.6. Spectral Loading

As discussed extensively above, wind turbines are subjected to spectral loads that are unique to this structure. Test spectra have been proposed, and fatigue data on material behavior are being obtained. However, to date, these data are limited in extent. Van Delft et al. [138, 142, 143] have examined the differences between the response in fiberglass to constant and variable amplitude loading using the WISPER and the WISPERX spectrum. Their experiments on a polyester fiberglass laminated with 0° and ±45° layers at approximately 32 percent fiber volume provide insight into using constant amplitude S-N data to predict service lifetimes under the spectral loads normally encountered by wind turbines.

5.4.6.1. WISPER vs. WISPERX

As discussed in section 4.8.1.1 "WISPER" on p. 37, the WISPERX load spectrum is the WISPER spectrum with the small cycles removed. Damage estimates predict that the removal of the small cycles should have less than a 10 percent effect. However, the measured data indicated that a difference of the order of 50 percent (a factor of 2) is actually observed, see Fig. 40. These data imply that the low-amplitude cycles are more damaging than suggested by the constant amplitude S-N data.

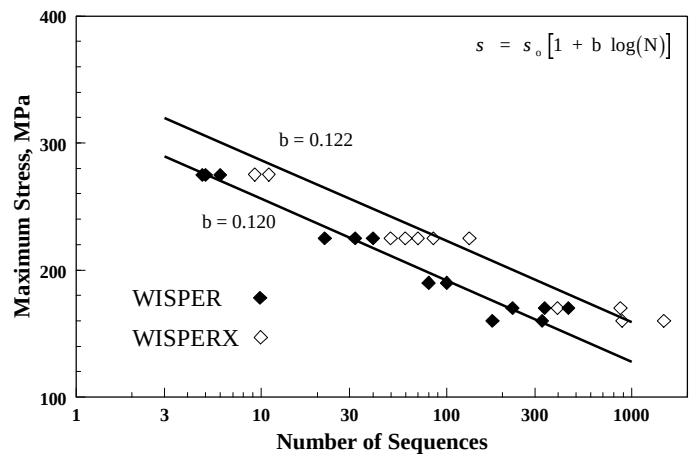

Figure 40. S-N Diagram for a Fiberglass Laminate with 0° and ±45° Plies, under WISPER Loading Conditions.

Also the fatigue exponent b is changed from approximately 0.10 for the constant amplitude data to approximately 0.12 for the spectral data, a significant change.[10]

5.4.6.2. Predicted Service Lifetime

Van Delft et al. [138, 143] have used the constant-amplitude European database to predict the response of composite coupons to the WISPER and the WISPERX loads. Lifetimes were predicted using Miner's rule and a power-law fit, see Eq. 32, to constant-amplitude S-N data for an R-value of a -1 (reverse loading). The data were expanded to a full Goodman diagram using a Goodman rule of the form shown in Eq. 38. *The predicted service lifetime is approximately two orders of magnitude higher than the measured lifetime*. However, when the S-N data were fit to a log-linear curve, Eq. 35, the predicted and measured service lifetimes were essentially the same, with the predicted service lifetime being slightly conservative.

In another study, Echtermeyer et al. [144] compared the predicted and measured fatigue life for several composite laminates to WISPERX spectral loads. These predictions of service lifetimes were based on a Goodman diagram constructed from S-N data for R-values of 0.1, -1 and 10. These data were fit best using a log-log representation. *In one laminate, the predictions agreed* with measured lifetimes. In two others, the prediction was a *factor of approximately 5 higher than the measured lifetime*. And in the final laminate, the predictions varied between a factor of 4 higher to a factor of 0.6 lower.

[10] In this case, the exponent being compared is based on the fit of the S-N curve for the number of the WISPER or WISPERX load sequences to failure.

Thus, *the behavior of composites under typical wind turbine loads is not well understood* and is the subject of on-going research in various wind programs throughout the world. Based on the limited data discussed above and the data presented in Fig. 40, we can surmise that the low amplitude fatigue cycles are more damaging than indicated by the constant-amplitude S-N data.

5.4.7. Structural Details

The extension of coupon data to the behavior of full-size structural components is being studied by Mandell et al. [127, 134, 145-148]. The results of their studies on such details as ply drops, local fiber content and transverse cracks are summarized in Table IV. The "knock-down" factor F in this table is defined to be the ratio of the maximum cyclic strain (R = 0.1) of a uniform coupon to that of a structured coupon at one million (10^6) cycles; namely:

$$F = \frac{\text{Uniform Coupon Strain @ } 10^6 \text{ Cycles}}{\text{Structured Coupon Strain @ } 10^6 \text{ Cycles}} \quad . \tag{45}$$

5.4.7.1. Ply Drops

One common feature of blade structures is the use of ply drops to tailor the thickness of the composite structure to meet loads criteria while minimizing weight. In the detailed studies by Cairns et al. [134, 146], several configurations for the ply drops have been experimentally investigated and analyzed. As shown in Fig. 41, the ply drop may be internal (covered by at least one layer of fabric) or external.

The internal ply drop creates local stress concentrations that initiate failures. As shown in Table IV, these local stress concentrations can significantly reduce fatigue lifetimes. The investigation illustrated that *internal ply drops are less susceptible to delamination than external ply drops* and that for the same ply drops, *thicker laminates are better in resisting delaminations*. As indicated by an increased knockdown factor [127], *dropping two plys in the same location is twice as harmful as dropping a single ply*, and that *feathering (i.e., staggering adjacent tows) or "Z-spiking*[11]*" the ply will significantly decrease delamination growth rate*.

Figure 41a. External Ply Drop.

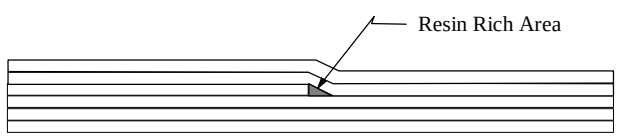

Figure 41b. Internal Ply Drop.

Figure 41. Typical Ply Drop Configurations.

[11] Z-spiking consists of plunging some of the fibers from the ply drop edge into the adjacent layers (the z-direction).

Table IV. Knock-Down Factors for Selected Structural Details in Tension and Compression for Approximately 70% 0° Materials.

DETAIL	SKETCH	KNOCK-DOWN FACTOR, F		
		A 130 Fabric	D155 Fabric	UC1018V Fabric
Simple Coupon (Straight Material)		1.0	1.0	1.0
Surface Indentation Tension, R=0.1 (V_f increased, thickness reduced by 25%)	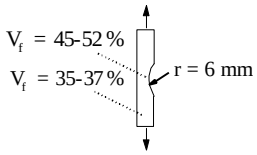	1.6	2.5	1.2
Surface Indentation Compression, R=10 (V_f increased, thickness reduced by 25%)	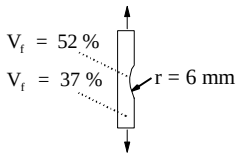	1.0	1.4	--
Locally Higher Fiber Content Tension, R=0.1 (2-90° Piles in center)	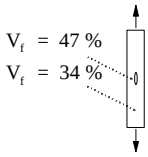	2.1	1.5	--
Locally Higher Fiber Content Compression, R=10 (2-90° Piles in center)	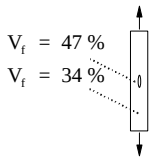	1.0	1.4	--
Exterior Cracked Transverse Tension, R=0.1 90° Patch		--	1.0	--
Double Interior 0° Ply Drop Tension, R=0.1	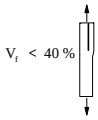	1.4	1.6	--

5.4.7.2. Locally Higher Fiber Content

As discussed above (see the discussion in section 5.4.3.2 "Fiber Content" on p. 60), the fiberglass laminates typically used in wind turbine blades are *susceptible to significant degradation in their fatigue properties if fibers are forced very close to one another*. The effect is noted in the dependence in fatigue coefficient on fiber density shown in Fig. 36. *This effect also translates into local manufacturing defects, simulated by surface indentations and excess fiber layers*. As shown in Table IV, a surface indentation produces a knock-down factor of 2.5 for a local increase in fiber content from 35 percent to 47 percent in tension. In compression, the knock-down factor is 1.4 for a local increase in the fiber volume from 37 percent to 52 percent.

5.4.7.3. Transverse Cracks

In typical lay-ups of composite structures and especially for wind turbine blades, a high percent of the fibers is aligned with the primary load direction. Additional off-axis layers are added to prevent splitting and to increase shear properties. As discussed above, these off-axis layers are typically more susceptible to fatigue damage. Ideally, these layers would split off from the underlying layers that carry the main loads without causing them to fail prematurely.[12] Thus, Table IV supports the concept that *no knock-down factor is required for the propagation of transverse cracks into uniaxial composites*. As discussed above, this factor is based on the assumption that fiber separation is adequate to prevent the fiber density effects discussed above.

5.4.7.4. Environmental Effects

As discussed by Kensche [16], wind turbine blades are subjected to a hostile environment throughout their service lifetimes. The primary effects include ultra violet (UV) radiation; temperature fluctuations; rain, ice, humidity; thunderstorms/lighting; hailstones; erosion from sand particles; and extreme dryness in desert environments. A matrix-rich outer-layer of gel coat is typically applied to the blades to provide UV protection and to seal the exterior surface of the composite.

Kensche [16] summarizes the degradation of the mechanical properties of various laminate systems used in wind turbine blades and presents a general discussion of the topic. Bach [149] presents a general discussion of the influence of moisture on bolted joints in composite materials.

In terms of fatigue behavior for composite laminates in turbine applications, the three most important environmental factors are attacks on the matrix material by temperature, humidity and UV radiation. The gel coating offers good protection from UV radiation. Temperature alone is typically not an important environmental parameter because the turbine blades are designed for a specific range of operating temperatures and the laminate's matrix is chosen to meet those

[12] Thus, the resulting failure of the cross section will be a relatively slow event that can be detected before catastrophic failure of the section (and the blade) occurs.

conditions.[13] However, temperature and humidity combined to become the primary environmental factors that must be considered in the fatigue design of the blade. The discussions here will concentrate on these two environmental factors.

5.4.7.5. Equilibrium Moisture Content

Under time-varying environmental loads, Fick's law [16] may be used to predict moisture content. Several authors have used this technique to analyze the yearly cycle of environmental loads of temperature, humidity and rain on a turbine blade. Kensche [16] used this technique to analyze the moisture content of a blade subjected to a yearly cycle of cold-wet and warm-dry conditions. His predictions indicate that the moisture content will stabilize at 0.4 to 0.5 percent. Similar simulations have been conducted by de Bruijn [150, 151] for the Dutch climatological cycle; see the discussion in section 5.4.7.8 "EN-WISPER Spectrum" on p. 70. For this set of conditions, the total moisture content is predicted to stabilize at approximately 0.25 percent. Measurements from a blade exposed to the Dutch environment for approximately four years agrees with the 0.25 percent prediction.

A question does arise concerning the use of the Dutch (northern European) climatological cycle for a general characterization of the behavior of composites under environmental loads. The Dutch cycle, and for that matter, a typical U.S. climatological cycle, is relatively benign. Turbines designed for deployment in other regions, e.g. India, will have significantly higher environmental loads. Designers of advanced composite structures (e.g., those using carbon fibers) consider Vietnam's climatological cycle as their extreme case. Thus, a moisture content of of 0.4 to 0.5 percent is non-conservative for many applications.

5.4.7.6. Matrix Degradation

The matrix materials used in turbine blades are typically polymeric materials that absorb moisture from the humidity in the surrounding air and/or from water lying on their surfaces. The temperature governs the velocity of the diffusion process, and the humidity governs the moisture content. As the moisture content increases, the glass transition temperature, T_g, of the matrix is depressed, and the matrix will swell. Eventually, microcracks (crazing) may form in the matrix. Depending on the physical and chemical properties of the matrix (i.e., toughness, etc.), these changes may destroy the structural integrity of the laminate. This damage to the matrix has minimal effect on the tensile behavior of the laminate because the fibers are the primary load carrier. However, these effects are significant in compression and shear, where the matrix is the primary load carrier.

[13] Differential thermal expansion can damage components of the wind turbine blade. However, as thermal expansion is more of a structural design problem than a material problem, it is not considered here.

5.4.7.7. Property Degradation

Kensche [16] presents a detailed examination of the effects of absorbed moisture on the physical properties of a typical epoxy laminate system. In this set of data, the test specimens have been preconditioned using continuous hot-wet conditions. These conditions are 90 percent humidity at 45°C. Under these conditions, specimens reach equilibrium in approximately 120 days with moisture content between 0.4 and 0.5 percent.

When comparing the properties of moist and dry virgin specimens, the static tensile strength was essentially not affected by absorbed moisture (as one would anticipate). The static compressive strength was reduced by approximately one third and the interlaminar shear strength by slightly over ten percent.

Figure 42 compares the fatigue performance of wet and dry samples under reverse loading (R = -1). These data illustrate that the strain-to-failure for a given lifetime (number of cycles to failure) is reduced by 15 to 20 percent. With the larger value occurring in the low-cycle region.

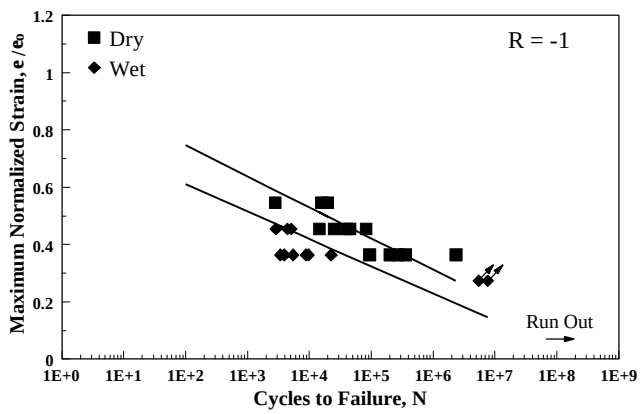

Figure 42. S-N Diagram for a Fiberglass Laminate with 0° and ±45° Plies, under Wet and Dry Environment Conditions.

Mandell [152] predicts similar results in compression tests of fiberglass coupons subjected to distilled water at 40°C for approximately 190 days. Under these conditions, the polyester matrix has a weight gain of approximately 3 percent. The compressive strength of these coupons is reduced by 10 to 20 percent when tested at room temperature. When tested at 50°C, the compressive strength is reduced by 20 to 35 percent.

5.4.7.8. EN-WISPER Spectrum

As discussed above, many of these tests are based on pre-conditioning the samples in a hot-wet environment. However, wind turbine blades in the field undergo a series of environmental changes, typically on an annual cycle that both adds and removes absorbed moisture from the blade. To help quantify the effects of field environment, de Bruijn [150, 151] and Joosse [153] have proposed a reference environmental spectrum. The spectrum is based on the annual Dutch climatological cycle, summarized and idealized (simplified) in Table V. The accelerated pre-conditioning cycle they proposed to simulate this climatological cycle is shown in Table VI. Both simulations and field measurements were used to validate that the accelerated cycle reproduced both the moisture profile and the moisture content.

Table V. Idealized Annual Climatological Cycle for the Dutch Environment.

Condition	Time, days	T, °C	ΔT, °C/hour	Relative Humidity, percent
Normal	228	10	5*	80
Hot	5.5	32	-5*	50
Frosty	22	-15	5*	85
Wet	109	8		100

*Rate of change of the temperature from the current to the next condition.

Table VI. Accelerated Climatological Cycle for the Dutch Environment.

Condition	Time, days	T, °C	ΔT, °C/hour	Relative Humidity, percent
Normal	105	18	50*	85
Hot	2.5	45	-50*	40
Frosty	10	-23	50*	100
Wet	49	16		100

*Rate of change of the temperature from the current to the next condition.

When tested, *the S-N data from samples that have been pre-conditioned by the EN-WISPER spectrum are not significantly different from non-conditioned specimens*; in contrast with the hot-wet pre-conditioned specimens discussion above. Joose [153] attributes this apparent discrepancy to a dominance of the test on the ambient conditions during the test. Implications of this observation are many. However, as noted by Joose, some test procedures have been called into question and require more study. Thus, the *pre-conditioned hot-wet samples do bound the problem, but the penalties in material performance they predict are probably too high for actual field conditions in Northern Europe and in most of the U.S. This may not be the case for India and Southeast Asia.*

5.4.7.9. Effects of the Environment

At this time, environmental effects on composite turbine blades are not well understood, and are currently a subject of research, discussion and speculation. For instance, some studies of advanced composites for aircraft indicate that the daily maximum use temperature is more important than the average temperature. *Thus, current databases may yield non-conservative designs for environmental loads. And, the designer should use them only with extreme care.*

5.4.8. Comments

The design of composite materials for wind turbine blades has relied heavily on fiberglass technology. This material system has proven adequate to the task, even though it must withstand

extremely large numbers of fatigue loads with varying amplitudes under extreme environmental conditions. Potential areas for increasing the performance of this system have been identified and are being pursued. In addition to increasing the performance characteristics of the materials system, an understanding of the influence of spectral and bi-axial loading on cumulative damage rules must be developed [154]. Also, design criteria for full-sized structures that are based on coupon data must be determined.

As blades become larger, stiffness considerations are becoming more and more important to the design. Fiberglass systems may not be able to meet these requirements within reasonable design constraints on weight. The obvious answer to this design issue is to introduce stiffer fibers, i.e., carbon fibers, into the composite system. Typically, carbon fiber designs have been too expensive for wind turbine applications. However, mixed fiber designs are currently under consideration and appear to be cost effective. These systems are not represented in the databases described above, but will need to be added. Specifically, the composite system with a mix of glass and carbon fibers will have to be addressed.

5.5. Fatigue Limit Design

The use of a fatigue limit for the fatigue analysis of structures is based on the observation that some metals have an essentially infinite life when tested at or below the value of their fatigue limit. Thus, the structural design is based on reducing the stress level at the highest load to the fatigue limit.

In terms of the S-N curve, an infinite life translates to a zero slope. Most materials do not have a true fatigue limit. However, many metals exhibit a significant reduction in the slope of their S-N curve as the number of cycles to failure gets very large. Figures 27 and 30 illustrate this behavior in aluminum and steel, respectively. For this class of behavior, a fatigue limit analysis can be conducted by assuming a quasi-fatigue limit that corresponds to the largest number of the cycles the structure will have to bear. In Fig. 27, the quasi-fatigue limit would be between 60 and 80 MPa for 10^9 cycles; in Fig. 30 the limit occurs at approximately $2x10^6$ cycles.

The existence of a true or quasi fatigue limit is usually based on the experimental data obtained from constant amplitude fatigue tests. In many cases, when these materials are tested with variable amplitude loads, the initial slope of the S-N curve does not change as the number of cycles become very large, see section 5.3.2.1 “S-N Data Base” on p. 52. *Because wind turbines are subjected to spectral loads, the use of constant-amplitude fatigue limit is probably not appropriate for most materials used in wind turbine structures.*

5.6. Partial Safety Factors

The IEC has adopted a set of partial safety factors in IEC-61400-1[17] to account for the uncertainties and variabilities in material properties (and in loads). For material properties, the partial safety factors are included for the following: unfavorable deviations of the strength of material from the characteristic value; inaccurate assessment of the resistance of sections or load-carrying capacity of parts of the structure; uncertainties in the geometrical parameters; and

uncertainties in the relation between the material properties in the structure and those measured by tests on control specimens. A discussion of partial safety factors and their application to wind turbine design is beyond the scope of this report and is not discussed here.

6. INFLOW

6.1. Annual Average Wind Speed

The determination of damage in a wind turbine is predicated on the development of a load spectrum for the turbine. As shown in Eq. 11, the typical formulation uses the annual average probability density function for the wind speed as a primary parameter in the description of the load spectrum. Rohatgi and Nelson [155] provide a detailed discussion of annual wind speed distributions and they provide a compilation of the annual average wind speed for numerous sites.

6.1.1. Formulation

The annual wind speed distribution is typically posed as a probability density function [155]. The Weibull distribution that is discussed in Appendix A has proven to be particularly effective in depicting the annual wind speed distribution above approximately 3 m/s at a number of U.S. and world sites [4]. This two-parameter distribution takes the following form:

$$p_U = \left[\frac{a}{b}\right]\left[\frac{U}{b}\right]^{a-1} \exp\left\{-\left[\frac{U}{b}\right]^{a}\right\} \quad , \quad (a > 0,\ b > 0,\ U > 0) \quad , \tag{46}$$

where p_U is the probability density function, α and β are the shape factor and the amplitude factor of the distribution, respectively. As cited in Eq. A-3, the average annual wind speed, $\overline{U}$, is given in terms of the Weibull parameters by:

$$\overline{U} = b\ \Gamma\left[1 + \frac{1}{a}\right] \quad , \tag{47}$$

where $\Gamma[\bullet]$ is the gamma function.

6.1.2. Typical Distributions

Extensive data have been gathered, collated and published that describe the annual wind speeds for the U.S. and vast regions of the world [3, 155, 156 and 157]. Typical annual wind speed distributions for several characteristic members of the Weibull distribution family are shown in Fig. 43. For this example, β is normalized to a value of one.

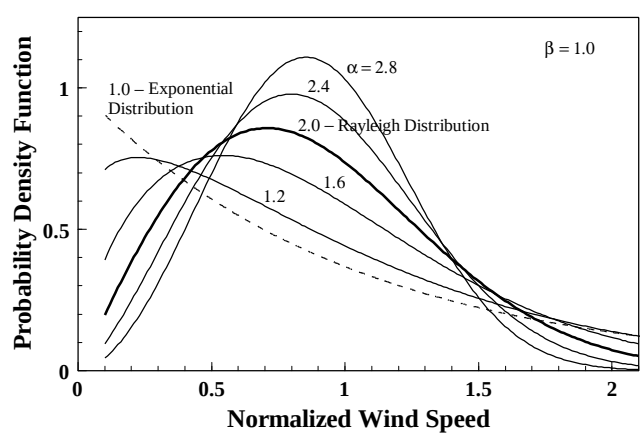

Figure 43. Weibull Probability Density Functions for Various Shape Factors.

Because the measurement and analysis

of these data are outside the scope of this report and they appear elsewhere in the open literature, detailed discussions of this subject are not presented here.

6.2. Inflow Characteristics

While "…tempting to think of wind as a constant homogeneous velocity field of fixed direction," the inflow is actually a three-dimensional, inhomogeneous, and unsteady flow field [4]. The challenge to the modeler is to describe those characteristics of the inflow that produce loads on the turbine. The three principal characteristics that have found favor with designers are the mean horizontal wind speed, the turbulence and the vertical shear.[14] As discussed above, this parameter set is probably not sufficient. Moreover, *at this time, there is no clear picture as to which inflow parameters govern the loads on the various machine configurations.* This section describes some of the atmospheric/inflow parameters that are currently being studied as potential predictors of turbine loads through the characterization of the inflow.

6.2.1.1. Turbulence

The primary characterization of the instantaneous flow field into the rotor has been the single-point turbulence intensity measured at hub-height in front of the turbine [5]. If the instantaneous horizontal velocity at rotor height, denoted by u(t), is separated into its long-term component U and its fluctuating value (about zero mean), such that,

$$u(t) = u(t) + U \quad \text{, where} \tag{48}$$

$$U = \frac{1}{T}\int_0^T u(t)\,dt \quad . \tag{49}$$

As noted above, the averaging time T is typically 10 minutes. The turbulence intensity I_u is the RMS of u' divided by its long-term average U. Namely,

$$I_u = \frac{\sigma_u}{U} = \frac{1}{U}\left[\frac{1}{T}\int_0^T (u)^2\,dt\right]^{1/2} \quad . \tag{50}$$

The parameter σ_u is commonly called the turbulence.

When determining operational loads on a turbine, each mean wind speed bin is assumed to have a weighted summation of the loads across the expected distribution for turbulence intensity.

---

[14] Variations in the inflow velocity can be separated into mean and turbulent components (i.e., long-term variations can be separated from short-term variations) because the power spectrum of the velocity of the inflow is divided naturally into two peaks. The low-frequency peak defines the variation of the mean inflow velocity and the high-frequency peak defines the turbulence. The peaks are separated by a spectral gap that covers the range from approximately 5 minutes to 2 hours [5].

6.2.1.2. Vertical Shear

The wind shear exponent α is typically used to characterize the variation of the mean wind speed from the bottom of the rotor disk to its top. In this form, the wind speed U as a function of height is given by:

$$\frac{U(z_1)}{U(z_2)} = \left[\frac{z_1}{z_2}\right]^{\alpha} \quad , \tag{51}$$

where z is the height above the prevailing terrain.

Wind shear is an integral part of the certification standard for wind turbines, and must be included in all structural analyses.

6.2.1.3. Additional Inflow Parameters

While turbulence and vertical shear are the two parameters typically used to describe the inflow, many additional inflow parameters are being investigated as descriptors for the inflow, or thereby, as predictors of turbine loads. In one of the more comprehensive experimental examinations of the relationship between inflow and fatigue loads to date, Mouzakis et al. [158-161] examine a long list of inflow statistics to determine which are important for introducing fatigue loads into the turbine. Their list includes mean horizontal velocity, standard deviation of the inflow in three directions, wind shear exponent, the skewness and kurtosis of the inflow in the primary flow direction, turbulence length scales in three directions and the Davenport decay factors for time and space between the hub and the top of the rotor. The turbulence length scale is a measure of the average size of eddies in the inflow [5]. The longitudinal length scale ${}^{x}L_u$ is defined in terms of the cross-correlation function R(r) by the following:

$${}^{x}L_u = \int_0 R(r)\,dr \quad , \tag{52}$$

where

$$R(r) = \frac{1}{T}\int_{t_o - T/2}^{t_o + T/2} \frac{u(x,t) \quad u(x+r,t)}{\sigma^2}\,dt \quad . \tag{53}$$

Using a regression analysis on three wind-speed bins that cover 7-9, 12-14, and 16-18 m/s, Mouzakis et al. calculate the correlation coefficient between fatigue loads and inflow statistics. Their evaluation of blade loads in mountainous terrain illustrates that *the standard deviation of the vertical component of the inflow, σ_w, dominates the flatwise blade loads.* This parameter was followed in importance by the average inflow velocity U, the standard deviations of the horizontal wind speed components (parallel and perpendicular to the direction of the average wind speed) and the wind shear exponent α. Some additional dependencies were noted for the skewness and kurtosis of the inflow. For edgewise blade loads, the inflow velocity U was the primary

parameter, with standard deviations of the vertical and horizontal wind speed components, and the shear exponent α following in their order of importance.

6.2.1.4. Reynolds Stresses

Kelley [49, 50] and Kelley and McKenna [51] have examined several other parameters for describing the inflow. The first are the Reynolds stresses. In a 3D flow field, these stresses are the average cross products of the fluctuating components of the inflow,

$$\overline{(u\,w)} \quad , \quad \overline{(u\,v)} \quad \text{and} \quad \overline{(v\,w)} \quad , \tag{54}$$

where u' and v' are the fluctuating components of the wind speed in the horizontal direction parallel and perpendicular to the direction of the average wind speed, respectively, and w' is the vertical component.

Richardson Number: Continuing the evaluation, Kelley et al. [49, 51] examined the gradient Richardson number, Ri. This parameter is a measure of the atmospheric stability between two elevations. For wind turbine applications, the two elevations are typically chosen with the reference elevation relatively close to ground level, denoted here with the subscript 1, and the other, the subscript 2, at the top of the rotor disk. If T is the temperature in degrees centigrade and the atmospheric pressure in hPa, then the layer mean potential temperature is given by:

$$\overline{(\quad_i)} = \left[\overline{T_i} + 273.16\right]\left[\frac{1000}{\overline{P_i}}\right]^{0.286} \quad . \tag{55}$$

The over bar on a quantity denotes its 10-minute average. The index i refers to the vertical position z of the measurement, i.e.; i = 1 refers to the reference height (typically near ground level) and i = 2 refers to an elevated height. Then the Ri is given by:

$$\mathrm{Ri} = \left(\frac{2\,g}{\overline{\quad_1} + \overline{\quad_2}}\right)\frac{\left(\overline{\quad_2} - \overline{\quad_1}\right)\Big/\left(z_2 - z_1\right)}{\left[\left(\overline{U_2} - \overline{U_1}\right)\Big/\left(z_2 - z_1\right)\right]^2} \quad , \tag{56}$$

where g is the gravitational acceleration (m/s^2). Based on the Richardson number, the atmosphere is said to be unstable when Ri < 0, near-stable when $0 \le \mathrm{Ri} < 0.01$ and stable when $\mathrm{Ri} \ge 0.01$.

Obukhov Length Scale: The final parameter investigated by Kelley et al. [49, 51] is the Obukhov length scale. This length is measured at a single elevation. This parameter is used in boundary layer turbulence scaling and is related to the gradient Richardson number. When divided into the elevation of the measurement, the result is the Monin-Obukhov stability parameter. In unstable

flows, the Richardson number is identical to the Monin-Obukhov stability parameter [49]. The Obukhov length scale is given by:

$$L = -\frac{\bar{\theta}\left[\left|\overline{(u'w')}\right|\right]^{3/2}}{0.4\, g\, \overline{(w'\theta')}} \quad , \tag{57}$$

where $\overline{(u\,w)}$ is the time average of the cross product of the fluctuating velocity components u' and w' described in Eq. 54 and $\overline{(w'\theta')}$ is the time average of the product of w' and the temperature θ' is fluctuating temperature components about the average temperature $\bar{\theta}$.

Kelley found that the flap bending loads were dominated by the vertical component of the Reynolds stress $\overline{(u\,w)}$. Thus, this term and the Richardson number dominate the edgewise-bending loads.

6.2.1.5. Summary

The effects of many inflow parameters have been shown to significantly influence turbine loads. Current practices reduce inflow descriptions to the mean horizontal inflow velocity, wind shear and the turbulence intensity. However, additional parameters must be examined to ensure that a complete set of loads on an operating turbine has been obtained; see section 4.4.2 “Inflow Parameters” on p. 26.

7. SOLUTION TECHNIQUES

The solution of Eq. 11,

$$\frac{1}{T} = \Delta D_t = \int_{U_{in}}^{U_{out}} p_U \int_{-\infty}^{\infty} \int_{0}^{\infty} \frac{n(s_m, s_a, U)}{N(s_m, s_a)} \, ds_a \, ds_m \, dU \quad , \tag{11}$$

for the damage rate in a wind turbine component can take many forms, depending on the assumptions about its characteristics. In this section of the paper, various solution techniques are presented.

7.1. Closed Form Solution

Although most solutions to Eq. 11 are numerical in form, Veers et al. [162, 163] have posed a closed form solution. The groundwork for this solution was laid by Veers in his analyses of the service lifetimes for VAWTs [18, 43-45]. As with all solutions, and in particular with closed form solutions, the assumptions behind the solution are very important.

7.1.1. Basic Assumptions

7.1.1.1. Annual Wind Speed Distribution

The wind speed distribution is assumed to be a Weibull distribution of the form cited in Appendix A and shown in Eq. 46. This two-parameter distribution is a function of the average annual wind speed $\overline{U}$ and the shape factor α_U.

7.1.1.2. Cyclic Stress

The distribution of cyclic stresses is also assumed to have a generalized Weibull distribution of the form shown in Eq. 24. The standard deviation of the cyclic stresses is assumed to depend directly on the mean wind speed. In this case, the dependence takes the form of a power law, namely:

$$s = K \, s_{char} \left(\frac{U}{U_{char}} \right)^p \quad , \tag{58}$$

where K is the stress concentration factor that relates global stresses to local stresses, and σ_{char} is the standard deviation of the cycle count distribution at a wind speed of U_{char}. The Weibull parameter for this distribution is α_s. The stress cycles are all assumed to have the same mean σ_m; see the discussion in section 4.5.4 “Mean Value Bins” on p. 30.

The rate at which these cycles are occurring is assumed to be a power series in wind speed of the form:

$$F = f_0 + f_1\left(\frac{U}{U_{char}}\right) + f_2\left(\frac{U}{U_{char}}\right)^2 \quad . \tag{59}$$

7.1.1.3. Material Behavior

The S-N curve is taken to be a straight-line fit on a log-log scale of the form cited in Eq. 31. Veers et al. have chosen to write the equation as follows:

$$N(\sigma_a, \sigma_m) \quad C\left(\frac{\sigma_a}{1 \quad K\frac{|\sigma_m|}{\sigma_u}}\right)^b \quad , \tag{60}$$

where the Goodman correction, see Eq. 38, based on the ultimate stress σ_u is used to include the effect of the constant mean stress σ_m.

7.1.1.4. Damage Rule

Miners Rule assumes that failure occurs when the damage equals one; i.e., when the damage rate ΔD_t in Eq. 11 for a representative time t multiplied by the projected lifetime T equals 1, see Eq. 6. However, depending on the material and the load spectrum, failure can occur at values of D that vary widely from one. For this analysis, failure is assumed to occur at a value of δ.

7.1.1.5. Run Time

The turbine is assumed to be available for the fraction A of each year of its operational lifetime, and the turbine is assumed to operate in all wind speeds between 0 and the cut-out wind speed V_{out}.

7.1.2. Solution

For the case, V_{out} and F = f_o, the predicted service lifetime T equals

$$T = \frac{C\delta}{f_0 A}\left\{\left(\frac{2}{(2/\alpha_s)!}\right)^{b/2}\left(\frac{K\sigma_{char}}{1 - K|\sigma_m|/\sigma_u}\right)^b\left(\frac{\overline{U}}{U_{char}(1/\alpha_U)!}\right)^{bp}\left(\frac{b}{\alpha_s}\right)!\left(\frac{bp}{\alpha_U}\right)!\right\}^{-1} \quad , \tag{61}$$

where the factorial (•)! is the gamma function.

The solution of this equation can be computed directly or by using the FAROW computer code [163].

7.2. Numerical Solutions

7.2.1. The LIFE Duo of Fatigue Analysis Codes

The initial analysis of the load spectra on a VAWT was addressed by Veers [18, 43-45]. These analyses laid the foundation for the LIFE series of fatigue analysis codes [164]. This formulation is essentially the numerical solution of Eq. 61 with a more restrictive set of assumptions; namely, the narrow-band Gaussian model for the stress spectra with a constant mean stress and cyclic frequency, a Rayleigh wind speed distribution, and a log-log description of the S-N curve. The initial code was later modified and used by Akins [165] and Malcolm [166]. Sutherland et al. [167] released the final version.

The great strength of the LIFE code was its simplicity. A VAWT could be analyzed relatively fast and with a minimum of input. However, its relatively restrictive assumption set soon led to a reformulation of its numerical algorithms that permitted the analysis of components from other classes of wind turbines. The code was completely rewritten and released by Sutherland et al. [168, 169]. The code, called the LIFE2 code, is essentially a solution for Eq. 11 with all of the functions described as tables. The table for each function can be input directly into the code or it can be generated using an internal algorithm. A six-volume set of reference manuals for this code is available [170-175].

The code is a PC-based, menu-driven FORTRAN code that is written in a top-down modular format. The package leads the user through the input definitions required to predict the service lifetime of a turbine component. The damage calculation may be based on Miner's rule or a linear-elastic crack propagation model [169]. Plotting capabilities are also included as an integral part of the code.

The LIFE2 code is used for most of the examples discussed above.

<u>7.2.1.1. Numerical Formulation</u>

The numerical formulation of the LIFE2 code is discussed in detail in Sutherland [171] and its numerical implementation in Schluter and Sutherland [170]. The numerical formulation starts with Eq. 11. The integrals in that equation may be discretized to the following finite summations:

$$\begin{aligned}\frac{1}{T} = \Delta D_t = & \sum_{q\,1}^{Q}\sum_{r\,1}^{R}\sum_{s\,1}^{S}(T_U)_q \frac{n_{qrs}\left[(\sigma_m)_r\,,\,(\sigma_a)_s\,,\,U_q\,,\,\Delta t\right]}{N_{rs}\left[(\sigma_m)_r\,,\,(\sigma_a)_s\right]} \\ & + \sum_{q\,1}^{Q}\sum_{r\,1}^{R}\sum_{s\,1}^{S}(S_U)_q \frac{n_{qrs}\left[(\sigma_m)_r\,,\,(\sigma_a)_s\,,\,U_q\,,\,\Delta t\right]}{N_{rs}\left[(\sigma_m)_r\,,\,(\sigma_a)_s\right]} \quad , \\ & + \sum_{q\,1}^{Q}\sum_{r\,1}^{R}\sum_{s\,1}^{S}(M)_q \frac{n_{qrs}\left[(\sigma_m)_r\,,\,(\sigma_a)_s\,,\,m_q\right]}{N_{rs}\left[(\sigma_m)_r\,,\,(\sigma_a)_s\right]}\end{aligned} \tag{62}$$

with

$$\left(T_U\right)_q = T_y \int_{U_{q-1}}^{U_q} p_U \, dU \quad , \tag{63}$$

where $U_0 = U_{in}$ and $U_q = U_{out}$, and T_y is the time in one year (in appropriate time units). The time steps in the second term, $(S_U)_q$ are similar to those in the first, but they start at $U_0 = U_{out}$ and U_q = maximum anticipated wind speed in term 2. In the first two terms, the matrix n(•) contains the cycle counts observed in time Δt. In each wind speed bin U_q (the bin size is from U_{q-1} to U_q), the cycle counts are binsed in R mean stress bins and S alternating stress bins. Although their form is identical, these terms have been separated in this analysis for convenience because the cycle count matrices, n(•), are typically derived from different data sets and/or analyses. In the last term, n(•) is the cycle count matrix for m_q occurrences of the discrete event q. These discrete events occur, on average, M_q times per year. In all three terms, the N(•) matrix is number of cycles to failure at the mean stress $(\sigma_m)_r$ and alternating stress $(\sigma_a)_s$.

In this form, Eq. 62 expresses the three classes of damage events explicitly. The first represents the damage from the operational stresses that occur between the cut-in and the cut-out wind speed. The second is the buffeting stresses that occur above the cut-out wind speed when the turbine is not operating. And the third is the transient events that occur during operation but are not covered by the first term. The latter term is typically used to describe stress cycles that occur during start/stop cycles, emergency shutdowns of various varieties, and any other transient events that damage the turbine.

In the LIFE2 formulation, all of the factors in Eq. 62 are held internally in tabular form. The input does not require that the tables match in size, bounds or intervals. Thus, the computational algorithms contained in the code typically interpolate between tabular inputs to obtain the size, bounds and intervals required to perform the summation cited in this equation.

7.2.1.2. Input Variables

Following Eq. 62, the LIFE2 code requires four sets of input for the prediction of the service lifetime of a turbine component. The first is the annual wind speed distribution at the site under investigation. The second is a description of the S-N (fatigue data) or crack growth rate data (linear crack propagation) for the material comprising the component under investigation. The third is the stress cycles on the component as a function of the operating state of the turbine and the average wind speed. And the fourth is the operating parameters and stress concentration factor(s) for the component.

The LIFE2 code contains many of the wind speed distributions, material models and load spectrum models that are discussed above. To use these internal models, the user supplies the parameters for the model, and the code constructs the appropriate discretization.

7.2.2. The ASYM Code

The ASYM code, originally started by McNerney [176] and continued by Vachon [177-182], performs a time-domain simulation that creates a random wind forcing function and predicts the second-to-second on-line control and damage of a wind turbine. Its output summarizes the energy produced, the sources of lost energy, the number of starts and stops at low and high wind-speed cut-outs, and the predicted service lifetime of the turbine.

The key elements of the code are a Markov wind simulator [183], the LIFE fatigue analysis [167] and a control module. The control module is rather simplistic in that the controller can only start and stop the turbine based upon current wind speed, moving averages of the wind speed and wait times following a shutdown. Control decisions are based on one-second updates of the inflow velocity. Initial formulations were limited to constant speed operation and instantaneous turbine response. Subsequent formulations [180, 182] added variable speed and inertial terms for the rotor. In addition to the standard LIFE fatigue analysis, ASYM includes the damage from start/stop cycles in its prediction of service lifetime.

ASYM is a unique analysis tool in that it permits a direct comparison of energy production and fatigue damage under various control algorithms. Vachon [179] used the Sandia 34-m Test Bed turbine (see Appendix B) to illustrate the ability of this code to evaluate control parameters. In this test case, the ASYM code was used to estimate the influence of the low-speed cut-in power on energy production and fatigue life at various Rayleigh wind speed sites with moderate turbulence. The basic controls for the turbine were assumed to have the following form: 1) The turbine is started after a moving average of the power in the wind, "low wind speed cut-in power," was exceeded; 2) the turbine coasts if it is running and the inflow fails to produce positive power; 3) if the turbine is coasting and the rpm falls below a low-rpm set point, the turbine is stopped; 4) if the inflow exceeds the "low-high" cut-out wind speed for a relatively long low-high moving average the turbine is stopped; 5) if the inflow exceeds the "high-high" cut-out wind speed for the relative short high-high moving average; and 6) once stopped, the turbine will remain stopped for a minimum time determined by the wait period set point. Typical values for these parameters are: a 30 kW (6 m/s) cut-in power for a 300-second moving average, low-high set point of 18 m/s for a 20-second moving average, a high-high set point of 22 m/s for a 4 second moving average and a 120-second wait time. As shown in Fig. 44, for various annual average wind speeds, the annual number of start/stop cycles is highly dependent on the low speed cut-in power control parameter and has significant site-to-site variability.

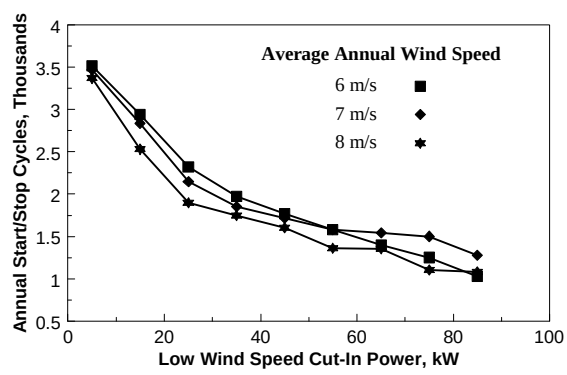

Figure 44. Variation of Low Wind Speed Start/Stop Cycles with Cut-In Power.

The evaluation continues with the determination of annual energy capture and fatigue life, see Figs. 45 and 46. Similar plots for the other control variables are provided in Vachon [179]. This information then permits current value analyses to project earnings and thereby optimize the control parameters.

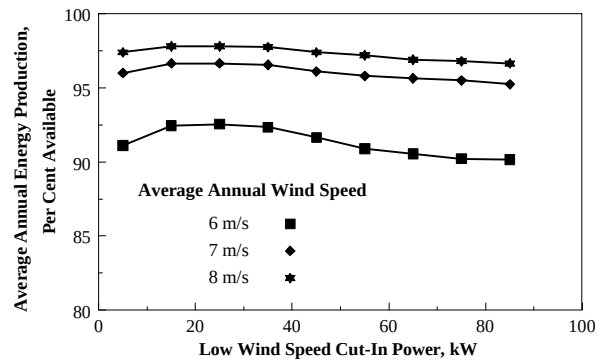

Figure 45. Variation of Annual Energy Production with Cut-In Power.

The ASYM code is an excellent code for setting the initial parameters in a turbine control system based on predictions of service lifetimes and cash flow. However, the code is based on a rather restrictive set of conditions that limits its effectiveness. Its obvious limits are the simplistic approach to turbine dynamics and the limited set of control options. Finally, the limited fatigue formulation hampers its use on a wide variety of turbines.

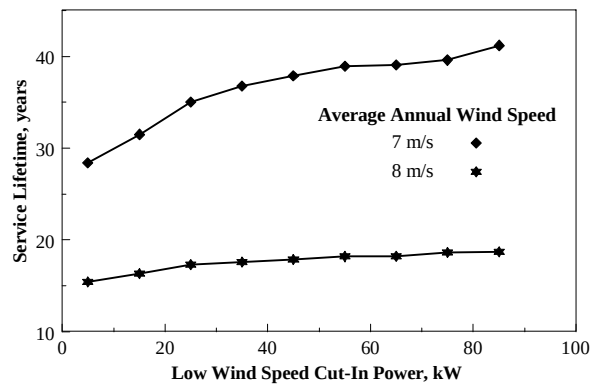

Figure 46. Variation of Service Lifetime with Cut-In Power.

7.2.3. Gear Codes

As discussed in section 4.8.2 "Load Spectra for Gears" on p. 39, the large variations in the torque supplied by the blades generally happen relatively slowly when compared to the time of gear teeth engagements. Thus, time-at-torque histograms are adequate for the analysis of fatigue of turbine gears and many commercial packages and propriety codes can be used for this analysis.

One code that has been applied successfully to the analysis wind turbine gears is the AGMA218 code developed by Errichello [83]. This code uses Miner's rule to perform either life ratings or power ratings of spur or helical gears. The code assumes that the gears conform to at least AGMA grade 2, their geometric accuracy conforms to at least AGMA quality No. 11, gear mesh alignment under load gives full-face contact consistent with a maximum load distribution factor of 1.2, and gear tooth stresses remain within elastic limits.

8. SPECIAL TOPICS

8.1. Reliability Analysis

After all of these analyses for fatigue are said and done, one must ask the question: "Have we asked the correct question?" All of the analyses discussed above are based on the question: "How long will this component last?" This question assumes that all of the inputs required to predict service lifetime are known with a relatively high degree of confidence and that we can describe mathematically the behavior of the turbine, the inflow, and its materials. The above discussions illustrate that this is simply not the case. The inflow has a random component that significantly affects the loads on the turbine. The turbine is a highly complex rotating structure that at the very least is subject to changes in its reaction to loads. These variations are due to the differences in individual components that arise from different suppliers and variations, within tolerance limits, of their manufacturing processes, and variations in the system resulting from the assembly of its many components. Further, the structural properties of each component are subject to statistical variations. These variations are especially large in the composites used in turbine blades. In addition to these deterministic variations in properties, there are even larger uncertainties in the state-of-nature, measurement, and modeling uncertainties and other approximations. Thus, in summary, perhaps we should be asking: "What is the probability that this turbine will achieve its design life?"

Obviously, fatigue analysis is the starting point for the answer to this question, so that our previous work has not been in vain. Moreover, reliability analysis is, at this point, relatively poorly understood and has not gained acceptance in the wind turbine community. This is not the case in many other structures that are subjected to random loads, e.g., the design of off-shore oil platforms. And, with all of the uncertainties and randomness in the prediction of service lifetimes for wind turbines, this is the wave of the future. Studies are currently being conducted in the U.S. [162, 163] and in Europe [184-187].

8.1.1. The Farow Code

The reliability studies by Veers et al. [162, 163] produced the FAROW code for the reliability analysis of turbine blades (see the discussion in section 7.1 "Closed Form Solution" on p. 81). This code, upgraded to do numerical integration and thus allow for more general inputs, is used in the following analysis.

8.1.2. Economic Implications

The form of the underlying fatigue question posed above raises a significant point concerning the type of fatigue failures one might see in a fleet of identical wind turbines [188]. If a single component has been under-designed,[15] each machine will have the same flaw that will produce

[15] For example, the design loads are under-estimated, or a seemingly minor change in the manufacturing process results in an inferior product, or the materials are behaving at the lower end of their performance spectrum

failures at approximately the same service lifetime. This class of failures will require a large capital outlay in a single installment to fix the fleet. In the opposite case when the turbine is not under-designed, the fleet will simply wear out over some period of time. Equivalent components on the various turbines will fail at some statistical variation about their mean service lifetimes. As a result, the capital outlays for maintaining the fleet will be distributed over time, rather than be concentrated in a single outlay.

Reliability analyses permit the designer to quantitatively determine the probability of failures over the operational life of a fleet of wind turbines based upon the statistical variations of the input parameters used to estimate the service lifetime of the fleet. Veers [188] details the techniques used in a typical evaluation. Once known, the failure probability can be incorporated into a financial analysis program to determine the financial risk for investors.

8.2. Analysis of Bonded Joints

The success or failure of a structure subjected to dynamic loads depends on the details of its design. This is especially true for wind turbine blades because they have both minimum weight and cost constraints placed on their design. One particular design detail that has proven to be very difficult is the bonded joint. This classical joint is used throughout wood and composite blades as the process of choice for joining blade parts. Primary applications have been for the blade root and for bonding span-wise beams (spars) to the blade skin, with the root joint being of paramount concern because all of the blade loads must be transferred through this structure to the hub. Detailed discussions of typical techniques for designing bonded joints are widely discussed [189-192], as are composite materials [193].

In classical wind turbine designs, two classes of bonded joints are favored. In the first, the root section of the blade is captured in metallic clamshell. The clamshell is typically bonded to the root. In the second, a hollow metallic cylinder is inserted into the blade root for bonding. In both cases, the metallic component contains the necessary attachment points that permit a metal-to-metal joint at the hub.

The bonded joints do not lend themselves to the fatigue or structural analysis techniques described above for other classes of structural components. The significant difference between the two is that the bond contains high-stress singularities at each of its ends. These singularities severely limit our ability to analyze these joints, and, therefore, most bonded joints must be tested to validate their design. Thus, the bonded joint is unique, and it is addressed in this special section of the paper. The section starts with a discussion of the singularities and then proceeds to discussions of the two classes of bonded joints.

8.2.1. The Bonded Joint

For illustration purposes, consider the bonded joint shown in Fig. 47a. Goland and Reissner [194] have analyzed this joint. Their analysis for a uniform, thin, elastic adhesive yields the shear stress distribution shown in Fig. 47b. As seen in this figure, the shear stresses are relatively small

along the bond line, except for very high stresses at each end.[16] Because the load on this joint is not symmetric, the bond is subjected to an internal bending moment that imposes a uniform tensile stress across the bond. This tensile stress, commonly called the "peel stress," is pulling the adhesive-adherend interfaces apart. And, the combined stress state produces premature failure of the bond joint; namely, the measured strength in this bond joint will be less than the strength of an equivalent symmetric joint with no peel stress across the bond. Moreover, if compressive peel stresses are placed across the bond, its apparent strength would increase.

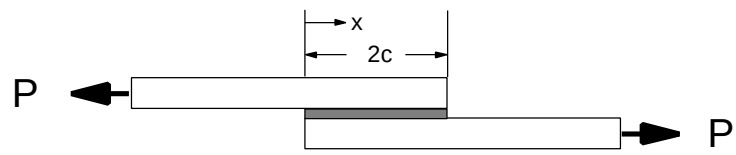

Figure 47a. Corner of a Lap Joint.

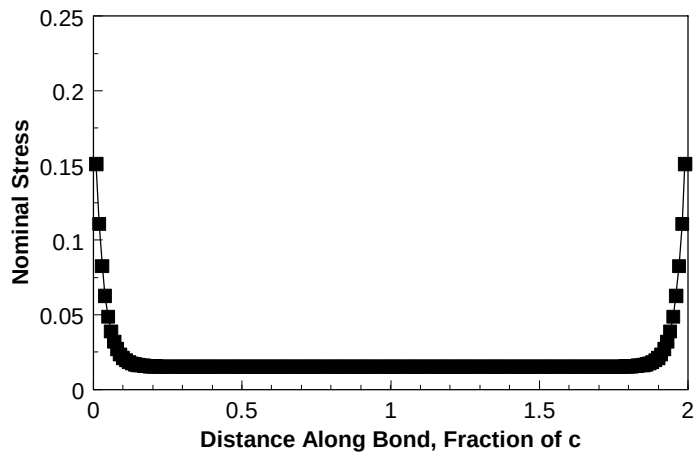

Figure 47b. Shear Stress in a Lap Joint.

Figure 47. A Typical Lap Joint.

For perfectly elastic materials, the singularities at both ends of the adhesive have an infinite stress level. When real materials are introduced into the problem, the adhesive at the end of the bond is deformed plastically and the stress is reduced to a finite level. As noted in the literature, e.g. see Carpenter and Patton [195], the singularity must be analyzed before the joint can be modeled adequately. When geometries are relatively simple, a fracture mechanics analysis that uses stress intensity factors works reasonably well. And when combined with specialized finite element analyses, more complex joint structures can be analyzed, e.g., see Habib, Aivazzadeh and Verchery [196]. However, most bonded joints must be tested to validate design loads.

8.2.2. Tubular Lap Joints

As discussed above, the bonded root joint for a turbine blade generally is cylindrical in geometry with a relatively thick layer of adhesive that varies in thickness in both the radial and circumferential directions. The bonded joint is required to support both axial and bending loads.

[16] As noted by Carpenter and Patton [195], "this solution is based on certain assumptions about the behavior of the adhesive … these assumptions can violate the equilibrium or compatibility equations as well as the boundary conditions." However, for our discussions here, this solution is adequate.

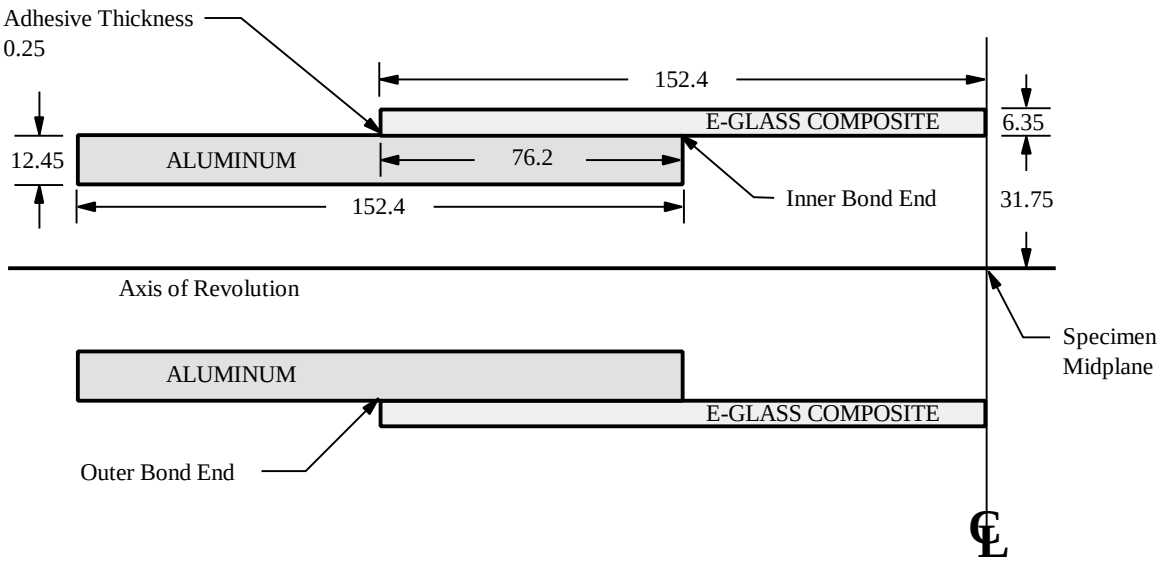

Figure 48. Geometry of the Tubular Lap Joint.

In a series of papers, Metzinger et al. [197-203] have combined state-of-the-art finite element analysis (FEA) techniques with experimental validation to examine idealized tubular lap joints that approximately represent the root connections in wind turbine blades. The joints that they analyzed, for the most part, are metallic (aluminum or steel) cylinders bonded to a fiberglass cylinder. Depending on the test series, the fiberglass cylinder was bonded either to the interior or the exterior of the metallic cylinder. For testing purposes, the specimens were constructed symmetrically, with the metallic cylinders bonded to either end of a composite cylinder. A typical specimen from this series of tests is shown in Fig. 48.

8.2.2.1. Axial Loads

To analyze this joint, detailed finite element analyses of the joint were first conducted for axial loads using two-dimensional (2D) axisymmetric meshes [198]. In two of the analyses presented in that paper, the adhesive is characterized as an unflawed (uncracked), elastic-plastic material and, in the another analysis, an elastic fracture mechanics methodology is used. The effective (von Mises) and the radial (peel) stress distributions along the joint, shown in Fig. 48, are plotted in Fig. 49. As shown in Fig. 49a, the percentage of the adhesive in plastic yield (i.e., at a von Mises stress of 60 MPa) increases to a significant portion of the bond length as the average shear stress is increased from 0.9 to 20.4 MPa. When loaded in tension, the peel stress is tensile at the outer bond end and compressive at the inner bond end. Thus, a tensile load places a compressive peel stress on the large plastic zone. When the joint is subjected to a compressive load, the sign is reversed, and the plastic zone is subjected to a tensile peel stress. Thus, the joint would be expected to fail at a lower load in compression than tension.

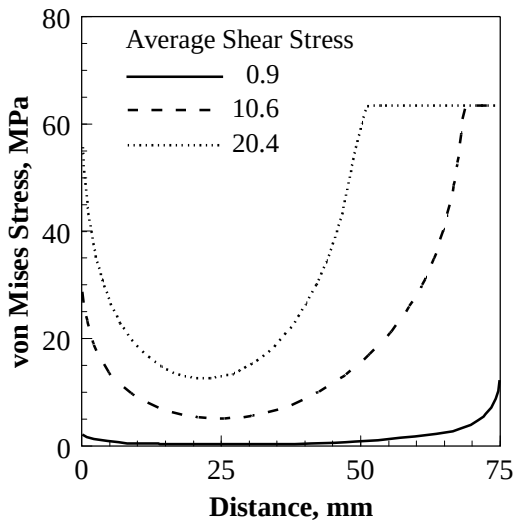

Figure 49a. Von Mises Stress Distribution.

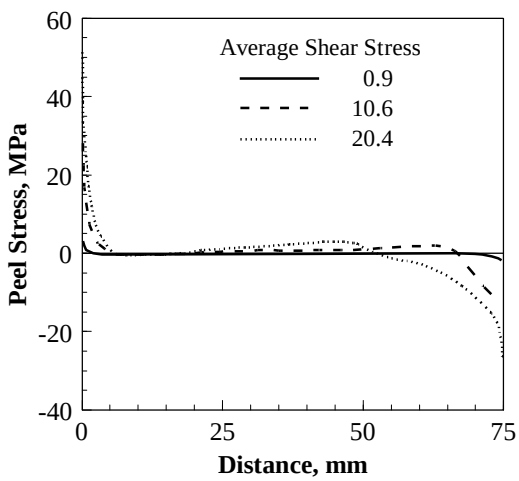

Figure 49b. Radial (Peel) Stress Distribution.

Figure 49. Stress Distribution in Cylindrical Lap Joint Under Tensile Loads (Distance measured from the outer bond end in elements adjacent to the bond end).

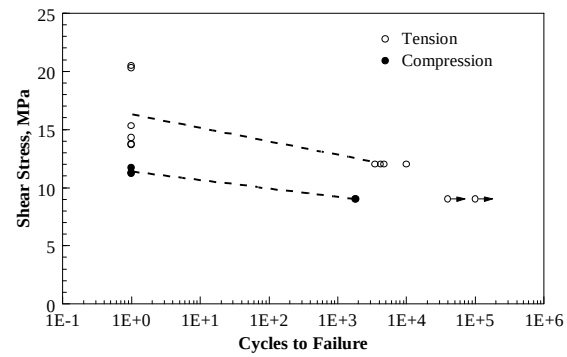

Figure 50. S-N Fatigue Data for an Aluminum-to-Fiberglass Bonded Joint.

The joint was tested under quasi-static loading to failure and under low-cycle fatigue loads, with R values of 0.1 and 10. These results are shown in Fig. 50. As shown in this figure and surmised above, the joint is weaker in compression than in tension and bond failures start in the regions with high plastic deformations (the inner bond end). These results also illustrate that bond failure is very susceptible to cyclic loading, with failure occurring in less than 10,000 cycles at 70 percent of its static strength.

These results are based on specimens constructed with the fiberglass cylinder bonded to the external surface on the steel cylinders. When this geometry is reversed, the sign of the peel stress will also be reversed [201]; namely, the peel stress is compressive with the joint in placed in tension and tensile when the joint is place in compression. The change in sign of the peel stress (tensile to compressive) is a direct result of the relatively large radial expansions/contractions (due to Poisson's effect) of the composite compared to that of the steel.

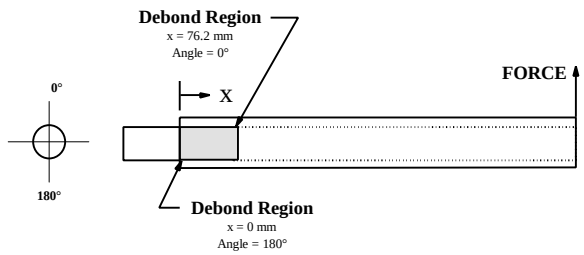

Figure 51a. Tubular Lap Joint with the Adhesive Bond Represented by Shaded Area.

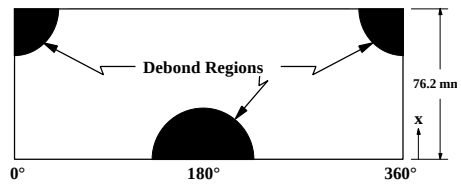

Figure 51b. C-Scan of the Debond Failure Regions.

Figure 51. Tubular Lap Joint Under Bending Loads.

8.2.2.2. Bending Loads

The axial loading results discussed above were extended to bending loads in Refs. 200 and 201. In the initial study [200], the tubular lap joint, depicted in Fig. 51a, was tested and analyzed using both a three-dimensional (3D) and a two-dimensional (2D) finite element model. Both FEA models illustrate that the peel stress is relatively large at the inner bond end at the 0° circumferential position and the outer bond end at the 180° circumferential position. Post-failure examination of the test specimens using C-scan images (see section 8.3 "Nondestructive Testing" on page 99) illustrated that the bond failed in these high-stress locations, see Fig. 51b.

Metzinger and Guess [201] analyzed turbine-size joints subjected to bending loads. They also used both 2D and 3D FEA models. Figure 52 presents a portion of the mesh used for the 3D finite element analysis of a circular turbine joint. As described above, relatively large peel stresses are

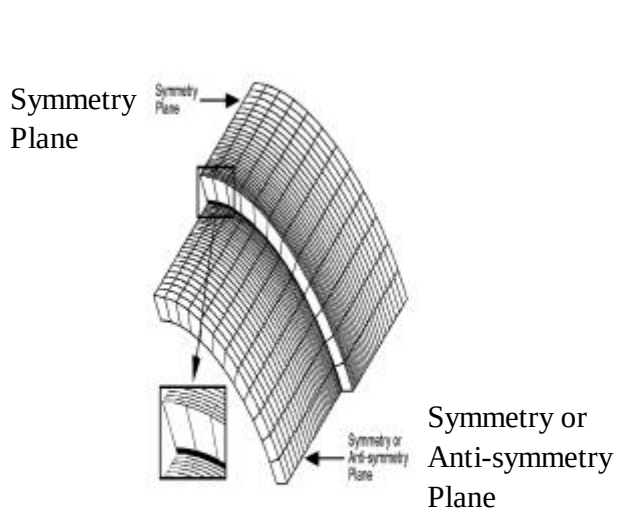

Figure 52. 3-D Finite Element Mesh of a Circular Bond Joint.

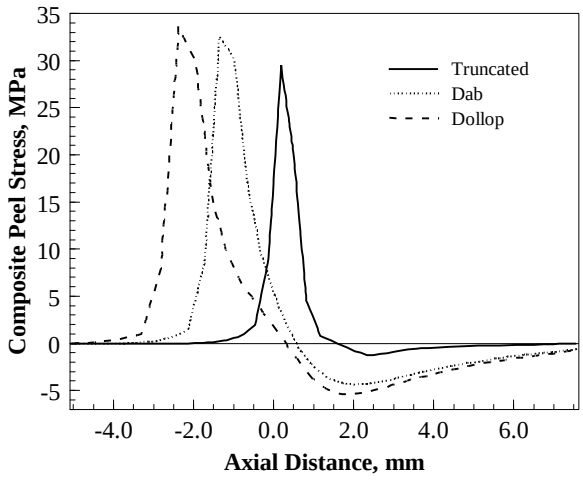

Figure 53. Composite Peel Stress Distribution Along the Top of the Joint (0° Circumferential Position).

found at the 0° and the 180° positions. A typical set of distributions for the composite peel stresses (near its surface) the top of the joint (0° circumferential position) is presented in Fig. 53. These distributions are a function of the adhesive geometries shown in Fig. 54. The distributions along the bottom of the joint (at the 180° circumferential position) would be equal in magnitude and opposite in sign from this plot. These analyses indicated that the yield zones and the peel stress riser are moved into the dab or dollop of adhesive, but they remain approximately the same in magnitude and extent, see Fig. 53.

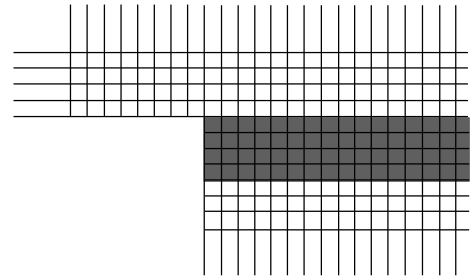

Figure 54a. Truncated Adhesive.

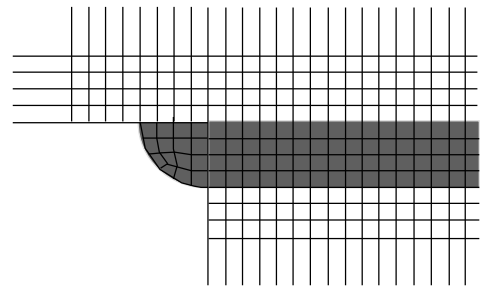

Figure 54b. Dab of Adhesive.

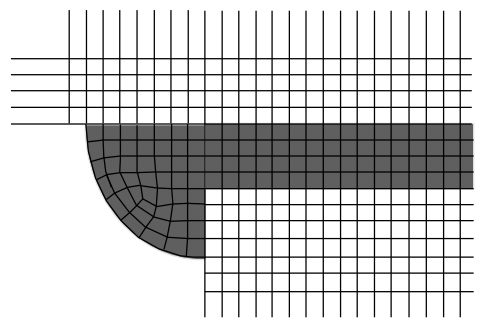

Figure 54c.Dollop of Adhesive.

Figure 54. Partial Finite Element Meshes with Varying Adhesive Geometries.

In addition to locating the areas where failures will probably occur and using the geometry of the adhesive to inhibit failure, Metzinger and Guess [201] did a detailed comparison of the 2D and the 3D FEA predictions. Based on the results shown in Fig. 55, they conclude that a 2D axisymmetric analysis of a joint under axial loads can be used effectively to analyze the shear stress distribution in a circular joint under bending loads. However, if the joint has an elliptical cross section, their results indicated that the 3D model is required. Because the 3D analyses typically require an order of magnitude more degrees of freedom than a 2D analysis, their results provide an effective technique for reducing the cost and computational capacity required to perform an analysis of a bonded joint under bending loads.

8.2.2.3. Geometric Considerations

The magnitude of the plastic zone at the end of the bond line and the sign of the peel stress can be controlled, somewhat, by the geometry of the joint. To investigate how the geometric variables might be manipulated to improve the joint, Metzinger and Guess [201-202] addressed both the geometry of the adhesive and the adherents.

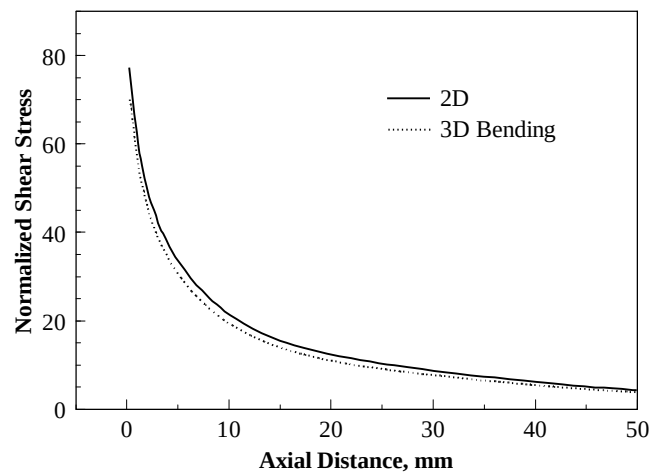

Figure 55. Normalized Shear Stress Distribution Along the Joint.

Tapered Adherents: A common technique for reducing the stress risers at the ends of the bond joint is tapering the adherents to eliminate abrupt changes in the section modulus. This strain matching technique seeks to reduce the size of the singularities at the end of the bond, i.e. the extent of the plastic von Mises stresses in the adhesive, by having smooth transitions between the two adherents and minimizing all changes in section modulus. As noted in section 8.2.2.4 "Contraction of the Adhesive During Cure" on p. 96, this technique can increase the performance of the joint. In the limited studies conducted by Reedy and Guess [198] and Metzinger and Guess [202], the results are inconclusive because of the limited number of specimens tested and because no attempts were made to optimize the taper. However, these first look results do indicate that for this geometry, tapering the adherents will probably be a second order effect to the sign of the peel stresses (see the "Peel Stress" discussion in section 8.2.2.3 "Geometric Considerations" on p. 95).

Excess Adhesive: As discussed above, a common technique used to increase the performance of a bonded joint is to form the shape of the adhesive at the end of the bond. In the results reported by Metzinger and Guess [201], several adhesive geometries were investigated, see Fig. 54. These analyses indicate that for bending loads, the yield zones and the peel stress riser are moved into the dab or dollop of adhesive but they remain approximately the same in magnitude and extent, see Fig. 53.

In another examination of the influence of adhesive geometry on joint performance, Metzinger and Guess [202] examined a geometrically different joint with two additional adhesive geometries, see Fig. 56. In this case, the extra adhesive configuration lowers the maximum tensile peel stress and produces a section of large compressive peel stress, see Fig. 57. As discussed in the next section, the minimization of the tensile peel stresses increases the performance of the joint in both quasi-static strength and fatigue life. *Thus, adding adhesive to the end of the joint may or may not help its performance, depending on the geometric and material considerations.* A FEA of the joint is required to evaluate enhancement to joint efficiency through the use of additional

adhesive, and testing of the joint is required to determine if the excess adhesive is predisposed to the formation of cracks that can fail the joint prematurely.

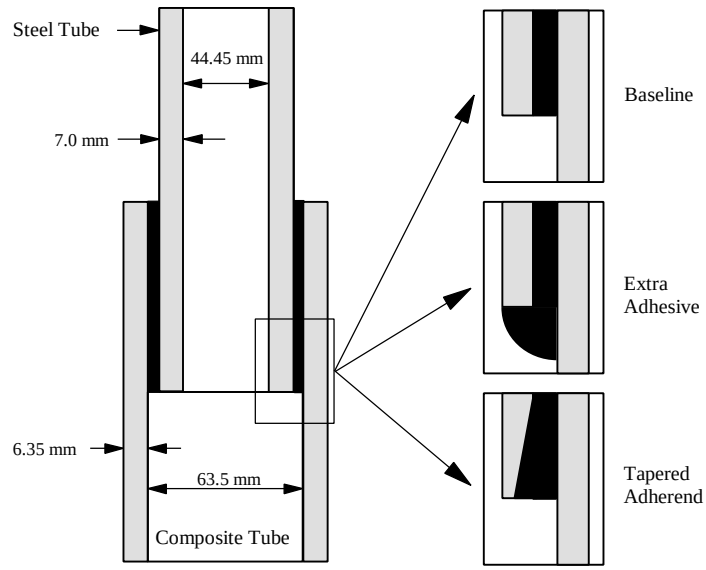

Figure 56. Schematic of the Joint Geometries.

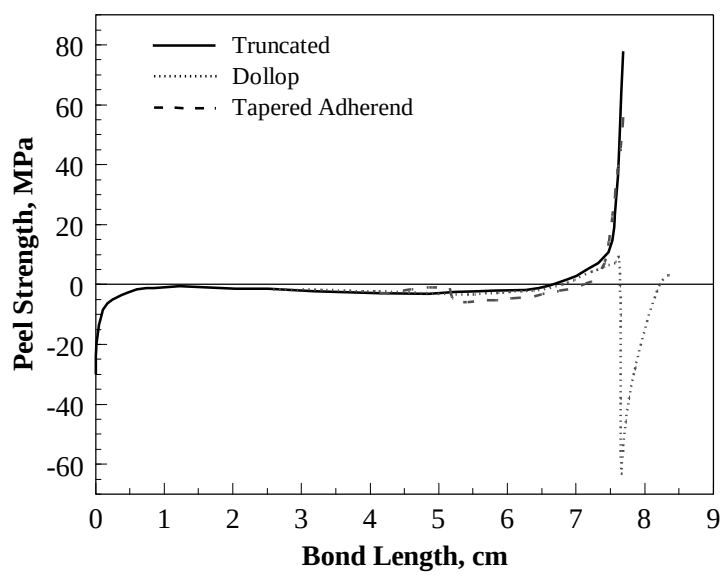

Figure 57. Composite Peel Stress with a Dollop of Adhesive and a Tapered Adherend for an Axial Compressive Load.

<u>Peel Stress</u>: In the initial studies of the bonded joints, the extent of the plastic strain region in the adhesive and the sign of the peel stress were identified as important parameters in the design of the joint. These results are based on the static analyses and the limited number of quasi-static and low-cycle fatigue tests that are cited above. To clarify the relative importance of these two parameters on high-cycle fatigue, Metzinger and Guess [203] began a systematic investigation of the bonded joint structure under axial and bending loads with quasi-static and fatigue applications. In this study and in previous studies, they noted that the plastic strain distribution in the joint would remain essentially constant when the joint was loaded with either a tensile or compressive load of equal magnitude, while the peel stress would reverse sign. To facilitate the fatigue study, a high-speed testing technique (based on resonance techniques) was developed to permit high-cycle fatigue testing of bending specimens.

To date, the results have demonstrated that the initial adhesive failure (debonding of the adhesive at the adhesive/steel interface) occurs where the peel stress is tensile, in both quasi-static tests and in a limited number

of high-cycle fatigue tests (10^7 cycles). Additional tests are on-going to determine consistency of these results in high-cycle fatigue and to enhance the statistical measures of these results.

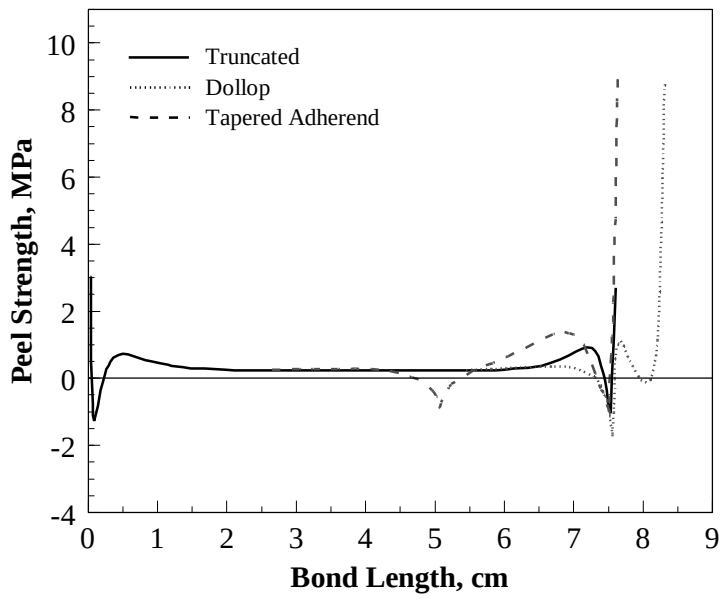

Figure 58. Composite Peel Stress due to Adhesive Contraction.

8.2.2.4. Contraction of the Adhesive During Cure

As adhesives cure, they undergo volumetric contractions. This contraction is relatively small, on the order of a few tenths of a percent, for most adhesives used for industrial applications. And, most of the shrinkage occurs before the adhesive has solidified. However, in the FEA of a tubular lap joint with a tapered adherend, Metzinger and Guess [203] demonstrated that the contraction of the adhesive can produce high tensile residual peel stresses in the adhesive, see Fig. 58, and thereby, reduce its performance.

8.2.3. Bolted Studs

Another class of bonded joints used in wind turbine applications is the bonded stud. In this technique, the stud is bonded directly into a preformed or drilled hole in the cross section of the blade. The connection has found favor in many designs because it provides metallic coupling elements between the root and the hub. The initial application of this jointing technique has been for the root joint of laminated wood structures, but additional applications as root joints in composite blades are also appearing.

A typical stud is shown in Fig. 59, [97, 204]. In this version of the design, the shank of the stud is a linear-tapered tube with a smooth exterior. The shank is bonded into a step-tapered hole in the root of the blade with an epoxy adhesive. The length and angle of the exterior taper and the size of the interior hole are adjusted in a strain-matching scheme to provide the necessary strength requirements and to improve its performance. Although steel is typically the material of choice for the studs, titanium studs have been used in optimal designs because the lower modulus of elasticity of titanium is closer to that of wood. In designs similar to that shown in Fig. 59, the exterior of the shank is threaded with rounded rings (threads with a zero helix angle). The shape of these threads varies between designs, but generally follow a rounded Acme or “Zuteck” thread

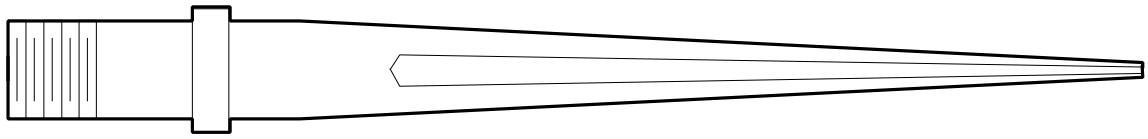

Figure 59. Typical Metal Stud Design.

profile [204]. Other designs have a hollow stud with a tapered internal cavity and a smooth exterior shank [149].

As reported by Pedersen and Clorius [105], the strength of a bonded stud is in general proportional to the square root of the glued-in length and directly proportional to the diameter. A balanced design calls for the quasi-static strength of the studs to be approximately the same as the shear strength of the bond. Faddoul [204] demonstrated that reinforcing the adhesive and the wood laminate can enhance the performance of a bonded stud system in wood laminates. He suggests reinforcing the adhesive with short chopped carbon fibers and the wood laminate with plies of carbon fibers. Chopped asbestos fibers also may be used to reinforce the adhesive, but they are not as effective as the carbon fibers and may create environmental problems. Additional performance gains can be achieved by using a non-linear taper on the shank.

The typical fatigue behavior of a bonded stud system is shown in Fig. 60 [97]. The curve fit to the data takes the form shown in Eq. 32, with a fatigue exponent of approximately 14. As one would anticipate, this joint performs better in compression than in tension. Reverse loading reduces tensile fatigue performance by approximately 25 percent, and, even moderate temperatures of 38°C (100°F) with high relatively humidity, degrades performance by 30 to 50 percent.

In similar experiments on studs that were bonded into a fiberglass laminate with an epoxy, Bach [149] showed shown a fatigue exponent of approximately 9, with most failure occurring at the composite/adhesive interface.

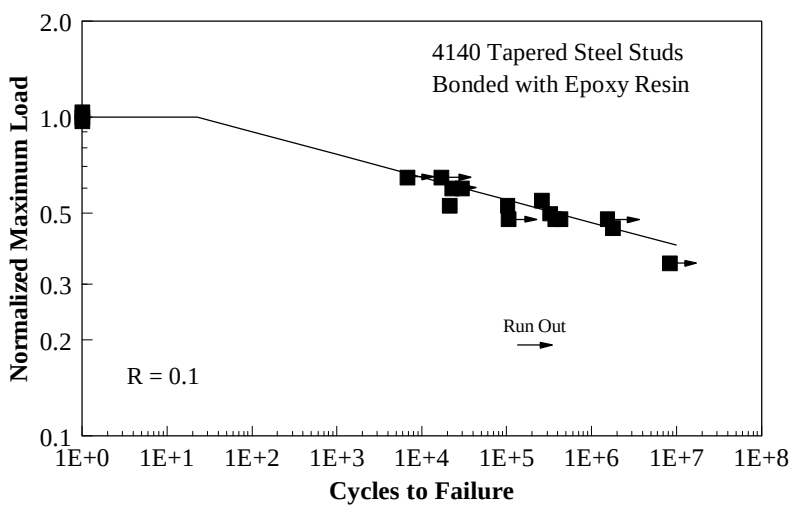

Figure 60. Fatigue Behavior of a Typical Metal Stud Bonded into a Wood Laminate.

In a recent study, Pedersen and Clorius [105] investigated the residual quasi-static strength of hollow, tapered bonded studs. These studs were bonded into a Swedish spruce glulam[17] blade. The 20-m blade was mounted on a wind turbine for 9 years (the turbine was operated only 3 of these 9 years). The authors estimate the studs had endured $5x10^7$ fatigue cycles when the blade was removed from the turbine because it had been struck by lightning. Based on a sample of 11 pull-out tests, the ultimate strength of the stud had been reduced by 5 percent from previously tested studs of this design. Failures were like a cork pulled from a bottle with all failures occurring in the immediate proximity of the wood/adhesive interface. The individual failures were either at the interface or a failure in the wood near that interface, with the former dominating.

8.2.4. Adhesives

The reader may note that this section of the paper does not include a detailed discussion of the material properties of the adhesive. Unfortunately, this is not an oversight. Rather it reflects a lack of material characterizations for typical adhesives that are in the public domain. Although some references are available, e.g. DeLollis [191] and Kinloch [205], only limited properties are available and those are usually limited to a single surface preparation and/or primer.

Typically, the designer is forced to develop the required material characterization as part of the design process, e.g. see Guess et al. [199], or use proprietary information obtained directly from the manufacturer. In most cases, the designer is forced to take a best practice approach and use supplier specifications and recommendations for the design and manufacturing of the complex joint structures. And, finally, component tests must be used to qualify the joint.

8.2.5. Comments

Although not proven conclusively, *the performance of tubular lap joints appears to be directly related to the peel stress that acts across the adhesive*. Because the stresses are singular at each end of the adhesive, the analysis of these joint systems are difficult at best, and even FEA must be used with extreme care because its predictions are mesh dependent. However, the designer can use FEA effectively to investigate the geometry of the joint that minimizes these stresses and, thus, maximizes the performance of the joint.

Unfortunately, *the quasi-static and fatigue strength of joints typically used for wind turbine applications cannot be predicted accurately*. A fracture mechanics approach based on stress intensity factors has had reasonably good success when geometries are relatively simple. And when combined with specialized finite element analyses, more complex joint structures can be analyzed, but failure strength typically cannot be predicted accurately. And as the design process for bonded studs indicates, most bonded joints must be tested to validate design

[17] A wood composite created from sheet veneers and epoxy. See the loads discussion in section 5.2.2 "Laminated Wood" on p. 47.

8.3. Nondestructive Testing

Nondestructive Testing and Evaluation (NDT and NDE) offer proven techniques for the inspection of structural components. General descriptions of techniques and applications exist in the literature [206, 207]. As well as applications of these techniques to wind turbines [208-210].

Two techniques that have proven to be especially useful in wind turbine applications are ultrasonic testing and acoustic emissions. The former uses the propagation characteristics of ultrasonic (acoustic) waves to measure material properties throughout the volume of an object. This technique is especially useful for the detection and characterization of surface and subsurface flaws. Acoustic emissions (AE) are elastic waves generated by the rapid release of energy from localized sources within a material. By monitoring AE events, typically an array of acoustic transducers is used, information concerning the location and structural significance of the detected events can be ascertained.

In the discussion entitled "Tubular Lap Joints" on p. 89, ultrasonic testing techniques [211] are used to detect damage, debonds and cracks in bonded joints that are tested to failure. This technique was extended to the inspection of bonded joints in wind turbine blades [200, 208].

Ultrasonic wave propagation techniques have also been used very successfully to grade veneers, see the discussion entitled "Grading" on p. 47.

Acoustic emissions have shown great promise in detecting the primary failure site of blades, in real time, while they were being tested in laboratory environments [209, 212]. Of primary importance is the ability of this technique to also identify areas of secondary damage. These are areas of high damage that typically do not fail during the test, and, therefore, are difficult or impossible to locate. They are important to designers because they identify weak points in the blade design. These sites will probably be the location of blade failures if the primary failure site is reinforced. Or, if the failure mechanism changes under field loads, these secondary sites may become primary failure sites.

Wei et al. [213] have used acoustic emissions to follow the damage of composite coupons under laboratory testing.

Additional applications of standard and non-standard NDT and NDE techniques to wind turbine components, in both laboratory and field environments, have been explored [209, 210, 214, 215].

8.4. Full Scale Testing

Once the design of a wind turbine blade has been completed and the turbine has been built, there is no guarantee that it will perform as intended. These highly complicated structures are susceptible to size effects, manufacturing variations, and inadequate designs. The only real tests of a blade design are through rigorous testing of the blade in a laboratory environment and on an operating wind turbine.

Musial et al. [81] and Musial and Allread [216] discuss full-blade testing in a laboratory environment. An IEC committee is currently developing a set of recommended practices for the full-scale testing of turbine blades [217]. Their guide identifies commonly accepted practices and provides guidance in establishing blade test criteria. Although outside the scope of this report, these testing techniques should be taken into consideration and used as a very important tool in the design of wind turbine blades.

9. CONCLUDING REMARKS

Wind turbines are fatigue critical structures that require detailed analyses to ensure survival under normal operating conditions in a turbulent environment. While these designs are difficult, they are not impossible. The research of the past few years provides the designer with most of the tools and knowledge to address design problems with a high degree of confidence. Some questions have yet to be answered, but research is ongoing. This paper was intended to guide the wind turbine designer through the issues that affect fatigue performance of turbine components and to describe best practices when appropriate.

10. REFERENCES

1. Righter, R.W., *Wind Energy in America, A History*, University of Oklahoma Press, Norman, 1996.

2. Baker, T.L., *Blades in the Sky*, Texas Tech University Press, Lubbock, 1992.

3. Hunt, V.D., *Windpower: A Handbook on Wind Energy Conversion Systems*, Van Nostrand Reinhold Co., New York, 1981.

4. Eggleston, D.M., and F.S. Stoddard, *Wind Turbine Engineering Design*, Van Nostrand Reinhold, New York, 1987.

5. Freris, L.L., ed., *Wind Energy Conversion Systems*, Prentice Hall, New York, 1990.

6. Spera, D.A., ed., *Wind Turbine Technology*, ASME Press, New York, 1994.

7. Walker, J.F., and N. Jenkins, *Wind Energy Technology*, John Wiley & Sons, Chichester, 1997.

8. Miner, A.A., "Cumulative Damage in Fatigue," *Trans. ASME*, Vol. 67, 1945, p. A159.

9. Rice, R.C., et al., *Fatigue Design Handbook*, SAE, Second Edition, 1988.

10. Osgood, C.C., *Fatigue Design*, Second Edition, Pergamon Press, New York, 1982.

11. Fuchs, H.O., and R.I. Stephens, *Metal Fatigue in Engineering*, Wiley & Sons, New York, 1980.

12. Lampman, S.R., ed., *ASM Handbook, Vol. 19: Fatigue and Fracture*, ASM Int., Materials Park, OH, 1996.

13. Hertzberg, R.W., *Deformation and Fracture Mechanics of Engineering Materials*, Wiley, New York, 1977.

14. Kanninen, M.F., and C.H. Popelar, *Advanced Fracture Mechanics*, Oxford University Press, New York, 1985.

15. Sutherland, H.J., P.S. Veers and T.D. Ashwill, "Fatigue Life Prediction for Wind Turbines: A Case Study on Loading Spectra and Parameter Sensitivity," *Case Studies for Fatigue Education*, ASTM STP 1250, R. I. Stephens, ed., 1994, p. 174.

16. Kensche, C.W., ed., *Fatigue of Materials and Components for Wind Turbine Rotor Blades*, EUR 16684, European Commission, Luxembourg, 1996.

17. *Wind Turbine Generator systems - Part 1: Safety Requirements*, IEC 61400-1, prepared by IEC-TC88, 1998.

18. Veers, P.S., "Simplified Fatigue Damage and Crack Growth Calculations for Wind Turbines," *Eighth ASME Wind Energy Symposium*, D.E. Berg and P.C. Klimas, eds., SED-Vol. 7, ASME, 1989, p. 133.

19. Sutherland, H.J., and L.L. Schluter, "The LIFE2 Computer Code, Numerical Formulation and Input Parameters," *Proceedings of WindPower '89*, SERI/TP-257-3628, September 1989, p. 37.

20. Sutherland, H.J., and L.L. Schluter, "Crack Propagation Analysis of WECS Components using the LIFE2 Computer Code," *Eighth ASME Wind Energy Symposium*, D.E. Berg and P.C. Klimas, eds., SED-Vol. 7, ASME, 1989, p. 141.

21. Sutherland, H.J., "Damage Predictions for Wind Turbine Components Using the LIFE2 Computer Code," *Proceedings of EWEC '89*, Peter Peregrinus Ltd, 1989, p. 384.

22. Butterfield, C.P., C. Stork, W. Holley, P.H. Madsen, and P.H. Jensen, "External Condition Models from the International Electrotechnical Commission Safety of Wind Turbine Standards (1400-1)," *1997 ASME Wind Energy Symposium*, AIAA/ASME, W. Musial and D.E. Berg, eds., 1997, p. 65.

23. Akins, R. E., "Cross-Spectral Measurements in the Testing of Wind Turbines," *Ninth ASME Wind Energy Symposium*, D. E. Berg, ed., SED-Vol. 9, ASME, 1990, p. 155.

24. *European Wind Turbine Standards, Vol. 2: Load Spectra for Wind Turbine Design*, EUREC-Agency, Joule II Programme, contr: JOU2-CT93-0387, Final Draft, 1996.

25. Madsen, P.H., ed., *Recommended Practices for Wind Turbine Testing and Evaluation*, Vol. 3 - Fatigue Loads, 1990, International Energy Agency, 1990.

26. "State of the Art of Aeroelastic Codes for Wind Turbine Calculations," *28th Meeting of Experts*, ISSN 0590-8809, IEA, B.M. Pedersen, ed., Lyngby, Denmark, 1996.

27. Downing, S.D., and D.F. Socie, "Simple Rainflow Counting Algorithms," *International Journal of Fatigue*, Vol. 4, N. 1, 1982, p. 31.

28. Sutherland, H.J. and L.L. Schluter, "Fatigue Analysis of WECS Components Using a Rainflow Counting Algorithm," *Proceedings of Windpower '90*, AWEA, Washington, DC, 1990, p. 85.

29. Wu, K.C., and S. Kammula, "A New On-Line, Real-Time RainFlow Counting Algorithm," *Wind Energy: Energy Week*, ASME/API, 1996, p. 132.

30. Veers, P.S., S.R. Winterstein, D.N. Nelson, and C.A. Cornell, "Variable Amplitude Load Models for Fatigue Damage and Crack Growth," *Development of Fatigue Loading Spectra*, ASTM STP 1006, J.M. Potter and R.T. Watanabe, eds., 1989, p. 172.

31. *Wind Turbine Generator Systems, Part 13: Measurement of Mechanical Loads*, Draft Technical Report, IEC 61400-13, prepared by IEC-TC88, Working Group 11, 1998.

32. Coleman, C., and B. McNiff, *Final Report: Dynamic Response Testing of the Northwind 100 Wind Turbine*, Subcontractor Report, SERI Cooperative Research Agreement #DE-FC02-86CH10311, Solar Energy Research Institute, Golden, CO, 1989.

33. Sutherland, H.J., "Frequency Domain Analysis of the Fatigue Loads on Typical Wind Turbine Blades," *J. of Solar Energy Engineering, Transactions of ASME*, Vol. 118, 1996, p. 204.

34. Sutherland, H.J., "Frequency-Domain Stress Prediction Algorithm for the LIFE2 Fatigue Analysis Code," *Eleventh ASME Wind Energy Symposium*, P.S. Veers and S.M. Hock, eds., SED-Vol. 12, ASME, 1992, p. 107.

35. Bishop, N.W.M. and F. Sherratt, "A Theoretical Solution for the Estimation of 'Rainflow' Ranges from Power Spectral Density Data," *Fatigue and Fracture of Engineering Materials and Structures*, Vol. 13, No. 4, 1990, p. 311.

36. Bishop, N.W.M., "Using Frequency Domain Methods to Predict Structural Fatigue of Wind Turbine Blades," *23rd Meeting of Experts – Fatigue of Wind Turbines*, IEA, M. Pedersen, ed., Golden, Colorado, 1992, p. 89.

37. Akins, R.E., "Rainflow Counting Based on Predicted Stress Spectra," *Eighth ASME Wind Energy Symposium*, D.E. Berg and P.C. Klimas, eds., SED-Vol. 7, ASME, 1989, p. 131.

38. Akins, R.E., "Rainflow Counting Based on Predicted Stress Spectra," *Seventh ASME Wind Energy Symposium*, A.H.P. Swift and R.W. Thresher, eds., SED-Vol. 5, ASME, 1988, p. 159.

39. Ashwill, T.D., D.E. Berg, L.R. Gallo, R.D. Grover, P.C. Klimas, M.E. Ralph, M.A. Rumsey, W.A. Stephenson, and H.J. Sutherland, "The Sandia 34-Meter VAWT Test Bed," *Proceedings of Wind Power '87*, American Wind Energy Association, SERI/CP-217-3315, 1987, p. 298.

40. Sutherland, H.J., and R.M. Osgood, "Frequency-Domain Synthesis of the Fatigue Load Spectrum for the NPS 100-kW Wind Turbine," *Proceedings of WindPower '92*, American Wind Energy Association, Washington, DC, 1992, p. 321.

41. Malcolm, D.J., *Fatigue Life Assessment of VAWT Components*, Indal Technologies, Mississauga, 1985.

42. Malcolm, D.J., "Predictions of Peak Fatigue Stresses in a Darrieus Rotor Wind Turbine Under Turbulence Winds," *Ninth ASME Wind Energy Symposium*, D. E. Berg, ed., SED-Vol. 9, ASME, 1990, p. 125.

43. Veers, P.S., *An Approach to the Fatigue Analysis of Vertical Axis Wind Turbine Blades*, SAND81-2130, Sandia National Labs, Albuquerque, NM, 1981.

44. Veers, P.S., "Blade Fatigue Life Assessment with Application to VAWTs," *J. Solar Engineering*, Vol. 104, 1982, p. 106.

45. Veers, P.S., *A General Method for Fatigue Analysis of Vertical Axis Wind Turbine Blades*, SAND82-2543, Sandia National Laboratories, Albuquerque, NM, 1983.

46. Akins, R.E., "Wind Turbine Fatigue Measurement Techniques," *Sixth ASME Wind Energy Symposium*, R.W. Thresher, ed., SED-Vol. 3, ASME, 1987, p. 147.

47. Jackson, K.L., "Deriving Fatigue Design Loads from Field Test Data," *Wind Power '92*, AWEA, 1992, p. 313.

48. Jackson, K.L., "A Method of Fatigue Life Assessment of Wind Turbine Structures," *Wind Energy - 1993*, S. Hock, ed., SED-Vol. 14, ASME, 1993, p. 179.

49. Kelley, N.D. "The Identification of Inflow Fluid Dynamics Parameters That Can be Used to Scale Fatigue Loading Spectra of Wind Turbine Structural Components," *Wind Energy - 1994*, W.D. Musial, S.M. Hock, and D.E. Berg, eds., SED-Vol. 15, ASME, 1994, p. 181.

50. Kelley, N.D., *Turbulence Descriptors for Scaling Fatigue Loading Spectra of Wind Turbine Structural Components*, NREL/TP-442-7035, NREL, Golden, 1994.

51. Kelley, N.D., and H.E. McKenna, "The Evaluation of a Turbulent Loads Characterization System," *Wind Energy: Energy Week*, ASME/API, 1996, p. 69.

52. Winterstein, S.R., and C.H. Lange, "Load Models for Fatigue Reliability from Limited Data," *Wind Energy - 1995*, W.D. Musial, S.M. Hock and D.E. Berg, eds., SED-Vol. 16, ASME, 1995, p. 73.

53. Winterstein, S.R., C.H. Lange, and S. Kumar, *FITTING: A Subroutine to Fit Four Moment Probability Distributions to Data*, Rept. RMS-14, Rel. Marine Struc. Prog., Civil Eng. Dept., Stanford University, Stanford, CA, 1995.

54. Winterstein, S.R., and T. Kashef, "Moment-Based Load and Response Models with Wind Engineering Applications," *1999 Wind Energy Symposium*, AIAA/ASME, 1999, p. 346.

55. Sutherland, H.J., and C.P. Butterfield, "A Summary of the Workshop on Fatigue Life Methodologies for Wind Turbines," *Proceedings of WindPower '94*, AWEA, Washington, DC, 1994, p. 279.

56. Ashwill, T.D., and P.S. Veers, "Structural Response Measurements and Predictions for the Sandia 34-Meter Test Bed," *Ninth ASME Wind Energy Symposium*, D. E. Berg, ed., SED-Vol. 9, ASME, 1990, p. 137.

57. Ashwill, T.D., H.J. Sutherland, and P.S. Veers, "Fatigue Analysis of the Sandia 34-Meter Vertical Axis Wind Turbine," *Ninth ASME Wind Energy Symposium*, D. E. Berg, ed., SED-Vol. 9, ASME, 1990, p. 145.

58. Lange, C.H., and S.R. Winterstein, "Fatigue Design of Wind Turbine Blades*:* Load and Resistance Factors from Limited Data," *Wind Energy: Energy Week*, ASME/API, 1996, p. 93.

59. Kashef, T., and S.R. Winterstein, "Relating Turbulence to Wind Turbine Blade Loads*:* Parametric Study with Multiple Regression Analysis," *1998 ASME Wind Energy Symposium*, W. Musial and D.E. Berg, eds., AIAA/ASME, 1998, p. 273.

60. Veers, P.S., and S.R. Winterstein, "Application of Measured Loads to Wind Turbine Fatigue and Reliability Analysis," *Journal of Solar Energy Engineering*, ASME, Vol. 120, 1998, p. 233.

61. Sutherland, H.J., and P.S. Veers, "Effects of Cyclic Stress Distribution Models on Fatigue Life Predictions," *Wind Energy - 1995*, W.D. Musial, S.M. Hock and D.E. Berg, eds., SED-Vol. 16, ASME, 1995, p. 83.

62. Kelley, N.D., and H.J. Sutherland, "Damage Estimates from Long-Term Structural Analysis of a Wind Turbine in a U.S. Wind Farm Environment," *1997 ASME Wind Energy Symposium*, AIAA/ASME, W. Musial and D.E. Berg, eds., 1997, p. 170.

63. Veers, P.S., "Three-Dimensional Wind Simulation," *Eighth ASME Wind Energy Symposium*, D.E. Berg and P.C. Klimas, eds., SED-Vol. 7, ASME, 1989, p. 23.

64. Veers, P.S., *Modeling Stochastic Winds on Vertical Axis Wind Turbines*, SAND88-0152, Sandia National Laboratories, Albuquerque, NM, 1988.

65. Kelley, N.D., "Full Vector (3-D) Inflow Simulation in Natural and Wind Farm Environments Using an Expanded Version of the SNLWIND (Veers) Turbulence Code," *Wind Energy - 1993*, S. Hock, ed., SED-Vol. 14, ASME, 1993, p. 77.

66. Cuerva-Tejero, A., S. López-Díez, and D. Bercebal-Weber, "Higher Level Descriptors of Sites and Wind Turbines by Means of Principal Components Analysis," *Proceedings of 1999 EWEC*, 1999, in publication.

67. Thresher, R.W., S.M. Hock, and R.M. Osgood, "Data Record Length Effects on Rainflow Analysis," *Eleventh ASME Wind Energy Symposium*, P.S. Veers and S.M. Hock, eds., SED-Vol. 12, ASME, 1992, pp. 117.

68. Jackson, K.L., "Scaling Wind Turbine Fatigue Design Loads," *Wind Energy - 1994*, W.D. Musial, S.M. Hock, and D.E. Berg, eds., SED-Vol. 15, ASME, 1994, p. 189.

69. Spera, D.A., "A Model of Rotationally-Sampled Wind Turbulence for Predicting Fatigue Loads in Wind Turbines of the Scale and Type of the NASA/DOE Mod-2 HAWT," *Wind Energy: Energy Week*, ASME/API, 1996, p. 59.

70. Barnard, J.C., and L.L. Wendell, "A Simple Method of Estimating Wind Turbine Blade Fatigue at Potential Wind Turbine Sites," *J. of Solar Energy Engineering, Transactions of ASME*, Vol. 119, ASME, 1997, p. 174.

71. Mann, J., "Wind Field Simulation," *Probabilistic Engineering Mechanics*, Elsevier Science LTD, Vol. 13, No. 4, 1998, p. 269.

72. Wilson, R.E., S.N. Walker, C.E. Smith and L.N. Freeman, "Advanced Dynamics Code," *Wind Energy - 1993*, S. Hock, ed., SED-Vol. 14, ASME, 1993, p. 119.

73. Hansen, A.C., *Yaw Dynamics of Horizontal Axis Wind Turbines: Final Report*, TP 442-4822, NREL, Golden, 1992.

74. Elliott, A.S., and A.D. Wright, "ADAMS/WT: An Industry-Specific Interactive Modeling Interface for Wind Turbine Analysis," *Wind Energy - 1995*, W.D. Musial, S.M. Hock and D.E. Berg, eds., SED-Vol. 16, ASME, 1995, p. 111.

75. Quarton, D.C., "The Evolution of Wind Turbine Design Analysis – A Twenty Year Progress Review," *Wind Energy*, Vol. 1, Spring 1998, p. 5.

76. Wilson, R.E., T.L. Weber and S.N. Walker, "Prediction of Fatigue Loads on a Free-Yaw HAWT," *Eleventh ASME Wind Energy Symposium*, P.S. Veers and S.M. Hock, eds., SED-Vol. 12, ASME, 1992, pp. 71.

77. Laino, D.J., and A.C. Hansen, "A Fatigue Analysis Interface for YawDyn and ADAMS," *Wind Energy: Energy Week*, ASME/API, 1996, p. 23.

78. Hansen, A.C., and D.J. Laino, "Validation Study for AeroDyn and YawDyn Using Phase III Combined Experiment Data," *1997 ASME Wind Energy Symposium*, AIAA/ASME, W. Musial and D.E. Berg, eds., 1997, p. 109.

79. Laino, D.J., and A.C. Hansen, "Sources of Fatigue Damage to Wind Turbine Blades," *1998 ASME Wind Energy Symposium*, AIAA/ASME, W. Musial and D.E. Berg, eds., 1998, p. 304.

80. Mouzakis, F., and E. Morfiadakis, "Identification of Low Cycle Effects on Wind Turbine Component Lifetime Estimation," *BWEA '97*.

81. Musial, W., M. Clark, N. Egging and M. Zuteck, "A Comparison of Strength and Load-Based Methods for Testing Wind Turbine Blades," *1997 ASME Wind Energy Symposium*, AIAA/ASME, W. Musial and D.E. Berg, eds., 1997, p. 228.

82. Wu, K.C., and R. De La Guardia, "The Effects of Controls on Fatigue Loads in Two-Bladed Teetered Rotor Wind Turbines," *Wind Energy: Energy Week*, ASME/API, 1996, p. 102.

83. McNiff, B.P., W.D. Musial, and R. Errichello, "Variations in Gear Fatigue Life for Different Wind Turbine Braking Strategies," *Proceedings of Windpower '90*, AWEA, Washington, DC, 1990, p. 131.

84. Larsen, G. and Thomsen, K., "A Simple Approximative Procedure for Talking into Account Low Cycle Fatigue Loads," *Proc. IEA 4th Symposium of Wind Turbine Fatigue*, IEA, 1996.

85. Sutherland, H.J., "Effect of the Flap and Edgewise Bending Moment Phase Relationships on the Fatigue Loads of a Typical HAWT," *Wind Energy - 1993*, S. Hock, ed., SED-Vol. 14, ASME, 1993, p. 181.

86. Zuteck, M.D., "A Methodology for Combined Loading Fatigue Calculations," *Wind Energy - 1994*, W.D. Musial, S.M. Hock, and D.E. Berg, eds., SED-Vol. 15, ASME, 1994, p. 205.

87. Timoshenko, S., *Strength of Materials*, C. Van Nostrand Co., Princeton, 1955.

88. Ten Have, A.A., *WISPER and WISPERX: Final Definition of Two Standardized Fatigue Loading Sequences for Wind Turbine Blades*, NLR-TP-91476U, National Aerospace Laboratory NLR, Amsterdam, the Netherlands, 1992.

89. Ten Have, A.A., "WISPER and WISPERX: A Summary Paper Describing Their Backgrounds, Derivation and Statistics," *Wind Energy - 1993*, S. Hock, ed., SED-Vol. 14, ASME, 1993, p. 169.

90. Kelley, N.D., "A Comparison of Measured Wind Park Load Histories With The WISPER and WISPERX Load Spectra," *Wind Energy 1995*, Musial, Hock and Berg, eds., SED-Vol. 16, ASME, 1995, p. 107.

91. Tangler, J., B. Smith, D. Jager, and T. Olsen, *Atmospheric Performance of the SERI Thin-Airfoil Family*, SERI/TP-257-3939, Solar Energy Research Institute, Golden, CO, 1990.

92. Tangler, J., N.D. Kelley, D. Jager and B. Smith, "Measured Structural Loads for the Micon 65/13," *Wind Energy - 1994*, W.D. Musial, S.M. Hock, and D.E. Berg, eds., SED-Vol. 15, ASME, 1994, p. 197.

93. Sutherland, H.J., and N.D. Kelley, "Fatigue Damage Estimate Comparisons for Northern European and U.S. Wind Farm Loading Environments," *Proceedings of WindPower '95*, AWEA, Washington, DC, 1995, pp. 177.

94. Thomsen, K. and S.M. Petersen, *Experimental Investigation of Gear Box Duration Loadings on Stall and Pitch Controlled Wind Turbines*, Riso-R-653(EN), RISO, Roskilde, Denmark, 1992.

95. Sutherland, H.J. and D.P. Burwinkle, "The Spectral Content of the Torque Loads on a Turbine Gear Tooth," *Wind Energy - 1995*, W.D. Musial, S.M. Hock and D.E. Berg, eds., SED-Vol. 16, ASME, 1995, p. 91.

96. AGMA/AWEA 921-A97, *Recommended Practices for Design and Specification of Gearboxes for Wind Turbine Generator Systems*, American Gear Manufacturers Association, Alexandria, VA, 1997.

97. Spera, D.A., J.B. Esgar, M. Gougeon, and M.D. Zuteck, *Structural Properties of Laminated Douglas Fir/Epoxy Composite Material*, DOE/NASA Reference Publication 1236, DOE/NASA/20320-76, Cleveland, 1990.

98. *Handbook of Fatigue Testing*, S.R. Swanson, ed., ASTM STP 566, Philadelphia, 1974.

99. Forman, R.G., V. Shivakumar and J.C. Newman, *Fatigue Crack Growth Computer Program: "NASA/FLAGRO,"* NASA, JSC-22267, Houston, 1986.

100. Forman, R.G., *Derivation of Crack Growth Properties of Materials for NASA/FLAGRO*, NASA, Materials Branch Report 86-ES5-1, Houston, 1986.

101. *Wood Handbook: Wood as an Engineering Material*, Forest Product Laboratory, U.S. Dept. of Agriculture, Agriculture Handbook 72, Washington, 1987.

102. Jung, J., *Stress Wave Grading Techniques on Veneer Sheets*, Forest Products Laboratory, General Technical Report FPL-27, Madison, 1979.

103. Jung, J., "Properties of Parallel-Laminated Veneer From Stress-Wave-Tested Veneers," *Forest Products Journal*, vol. 32, no. 7, 1982, pp. 30.

104. Jamieson, P., "The Design of Wood Epoxy Wind Turbine Blades," *Eighth ASME Wind Energy Symposium*, D.E. Berg and P.C. Klimas, eds., SED-Vol. 7, ASME, 1989, p. 147.

105. Pedersen, M.U., and C.O. Clorius, *The Strength of Glued-in Bolts after 9 Years In Situ Loading*, Technical University of Denmark, DK9601314, NEI-DK-2303, 1995.

106. Stipe, C., W. Musial, M. Jenks, and S. Hughes, *Static Ramp and Compression-Compression Fatigue Testing of Sitka Spruce Specimens*, National Renewable Energy Laboratory, Golden, 1999.

107. Bonfield, P.W. I.P. Bond, C.L. Hacker and M.P. Ansell, "Fatigue Testing of Wood Composites for Aerogenerator Blades. Part VII, Alternative Wood Species and Joints", *Wind Energy Conversion*, B.R. Clayton, ed., Mechanical Engineering Publications Ltd., 1992, p. 243.

108. Boyer, H.E., and T.L. Gall, eds., *Metals Handbook*, Desk Edition, American Society for Metals, Metals Park, Ohio, 1985.

109. *Aluminum Standard and Data, 1984*, Eighth Edition, The Aluminum Association, Washington, DC, 1984.

110. Boyer, H.E., ed., *Atlas of Stress-Strain Curves*, American Society for Metals, Metals Park, Ohio, 1985.

111. Boyer, H.E., ed., *Atlas of Fatigue Curves*, American Society for Metals, Metals Park, Ohio, 1985.

112. Peterson, R.E., *Stress Concentration Factors, Charts and Relations Useful in Making Strength Calculations for Machine Parts and Structural Elements*, Wiley Interscience Publication, New York, 1974.

113. Hoeppner, D.W., ed., *Fatigue Testing of Weldments, STP 648*, American Society for Testing and Materials, Philadelphia, 1977.

114. Alcoa Industries working with SNL engineers in mid 1970s: see, Kadlec, E.G., *Characteristics of Future Vertical Axis Wind Turbines*, SAND79-1068, Sandia National Laboratories, Albuquerque, NM, 1982.

115. Berg, D.E., P.C. Klimas, and W.A. Stephenson, "Aerodynamic Design and Initial Performance Measurements for the Sandia 34-m Diameter Vertical-Axis Wind Turbine," *Ninth ASME Wind Energy Symposium*, D. E. Berg, ed., SED-Vol. 9, ASME, 1990, p. 85.

116. Van Den Avyle, J.A., and H.J. Sutherland, "Fatigue Characterization of a VAWT Blade Material," *Eighth ASME Wind Energy Symposium*, D.E. Berg and P.C. Klimas, eds., SED-Vol. 7, ASME, 1989, p. 125.

117. Mitchell, M. R., "Fundamentals of Modern Fatigue Analysis," *Fatigue and Microstructure*, ASM Material Science Seminar, St. Louis, MO, 1978, American Society for Metals, 1979.

118. Rolfe, S.T., and J.M. Barsom, "Fracture and Fatigue Control in Structures," *Applications of Fracture Mechanics*, Prentice-Hall, 1977, p. 244.

119. Hatch, P.W., J.A. Van Den Avyle and J. Laing, *Fatigue Crack Growth Automated Testing Method*, SAND89-0778 Sandia National Laboratories, Albuquerque, 1989.

120. Warren, A.S. and R.M. Pelloux, *Fatigue Behavior of 6063 Aluminum Alloy Extrusions for Wind Turbine Applications*, Final Report, SNL Contract No. 33-7708, MIT, Cambridge, 1990.

121. Veers, P.S., and J.A. Van Den Avyle, "Fatigue Crack Growth from Narrow-Band Gaussian Spectrum Loading in 6063 Aluminum Alloy," *Advances in Fatigue Lifetime Predictive Techniques*, ASTM STP 1122, M.R. Mitchell and R.W. Landgraf, eds., ASTM, Philadelphia, 1992, p. 191.

122. AGMA Standard, *Standard - Design Guide for Vehicle Spur and Helical Gears*, AGMA 170.01-1976, American Gear Manufacturers Association, Alexandria, VA, 1976.

123. AGMA Information Sheet, *Geometry Factors for Determining the Pitting Resistance and Bending Strength of Spur, Helical and Herringbone Gear Teeth*, AGMA 908-B89, American Gear Manufacturers Association, Alexandria, VA, 1989.

124. *Composites, Engineered Materials Handbook*, Vol. 1, ASM, T.J. Reinhart, Tech. Chair., Materials Park, OH, 1998.

125. Tsai, S.W., and H.T. Hahn, *Introduction to Composite Materials*, Technomic Publishing Co., Inc., 1980.

126. Mayer, R.M., ed., *Design of Composite Structures Against Fatigue: Applications to Wind Turbine Blades*, Mechanical Engineering Publications, United Kingdom, 1996.

127. Mandell, J.F. and D.D. Samborsky, *DOE/MSU Composite Materials Fatigue Database: Test Methods, Materials, and Analysis*, SAND97-3002, Sandia National Laboratories, Albuquerque, 1997.

128. De Smet, B.J., and P.W. Bach, *Database FACT: Fatigue of Composite for wind Turbines*, ECN-C-94-045, ECN, Petten, 1994.

129. Mandell, J.F., R.M. Reed Jr., and D.D. Samborsky, *Fatigue of Fiberglass Wind Turbine Blade Materials*, Contractor Report SAND92-7005, Sandia National Laboratories, Albuquerque, NM, 1992.

130. Mandell, R.M., J.F. Reed Jr., D.D. Samborsky and Q. Pan, "Fatigue Performance of Wind Turbine Blade Materials," *Wind Energy - 1993*, S. Hock, ed., SED-Vol. 14, ASME, 1993, p. 191.

131. Mandell, J.F., R.M. Creed Jr., Q. Pan, D. W. Combs and M. Shrinivas, "Fatigue of Fiberglass Generic Materials and Substructures," *Wind Energy - 1994*, W.D. Musial, S.M. Hock, and D.E. Berg, eds., SED-Vol. 15, ASME, 1994, p. 207.

132. Mandell, J.F., D.W. Combs and D.D. Samborsky, "Fatigue of Fiberglass Beam Substructures," *Wind Energy - 1995*, W.D. Musial, S.M. Hock and D.E. Berg, eds., SED-Vol. 16, ASME, 1995, p. 99.

133. Samborsky, D.D. and J. F. Mandell, "Fatigue Resistant Fiberglass Laminates for Wind Turbine Blades," *Wind Energy: Energy Week*, ASME/API, 1996, p. 46.

134. Cairns, D.S., J.F. Mandell, M.E. Scott, and J.Z. Macagnano, "Design Considerations for Ply Drops in Composite Wind Turbine Blades," *1997 ASME Wind Energy Symposium*, AIAA/ASME, W. Musial and D.E. Berg, eds., 1997, p. 197.

135. Shrinivas, M., *Three Dimensional Finite Element Analysis of Matrix Cracks in Multidirectional Composite Laminates*, M.S. Thesis, Dept. of Chem. Engr., Montana State University, 1993.

136. Samborsky, D.D., J.F. Mandell and D.S. Cairns, "Selection of Reinforcing Fabrics for Wind Turbine Blades," *1999 Wind Energy Symposium*, AIAA/ASME, 1999, p. 32.

137. Mandell, J.F., D.D. Samborsky and H.J. Sutherland, "Effects of Materials Parameters and Design Details on the Fatigue of Composite Materials for Wind Turbine Blades," *Proceedings of 1999 EWEC*, 1999, in publication.

138. Van Delft, D.R.V., G.D. de Winkel, and P.A. Josses, "Fatigue Behavior of Fibreglass Wind Turbine Blade Material Under Variable Amplitude Loading," *1997 ASME Wind Energy Symposium*, AIAA/ASME, W. Musial and D.E. Berg, eds., 1997, p. 180.

139. Mandell, J.F., "Fatigue Behavior of Short Fiber Composite Materials," *The Fatigue Behavior of Composite Materials*, K.L. Reifsnider, ed., Elsevier, 1991, p. 232.

140. Mohamadian, H.P., and I.J. Graham, "Stiffness Degradation In Unidirectional + Chopped Mat E-Glass Fiber/Polyester and Vinylester Composite Laminates," *Tenth ASME Wind Energy Symposium*, D.E. Berg and P.S. Veers, eds., SED-Vol. 11, ASME, 1991, p. 55.

141. Sutherland, H.J., and J.F. Mandell, "Application of the U.S. High Cycle Fatigue Data Base to Wind Turbine Blade Lifetime Predictions," *Wind Energy: Energy Week*, ASME/API, 1996, p. 85.

142. Van Delft, D.R.V., P.A. Joosse and H.D. Rink, "Fatigue Behavior of Fibreglass Wind Turbine Blade Material at the Very High Cycle Range," *Proceedings of EWEC '94*, 1994, p. 379.

143. De Winkel, G.D., and D.R.V. Van Delft, *Fatigue Behavior of Glass Fibre Reinforced Polyester for Wind Turbine Blades; Part 2: Fatigue Behavior under the WISPER and WISPERX Variable Amplitude Loading*, Stevin Report 6-96-20, Delft University of Technology, Delft, The Netherlands, 1996.

144. Echtermeyer, A.T., C. Kensche, P. Bach, M. Poppen, H. Lilholt, S.I. Andersen and P. Brøndsted, "Method to Predict Fatigue Lifetimes of GRP Wind Turbine Blades and Comparison with Experiments," *Proceedings of the European Union Wind Energy Conference*, Göteborg, Sweden, 1996, p. 907.

145. Mandell, J., D. Samborsky and D. Cairns, "Advanced Wind Turbine Blade Structure Development Program at Montana State University," *1997 ASME Wind Energy Symposium*, AIAA/ASME, W. Musial and D.E. Berg, eds., 1997, p. 189.

146. Mandell, J., D. Samborsky, M. Scott and D. Cairns, "Effects of Structural Details on Delamination and Fatigue Life of Fiberglass Laminates," *1998 ASME Wind Energy Symposium*, AIAA/ASME, W. Musial and D.E. Berg, eds., 1998, p. 323.

147. Cairns, D., D. Haugen, J. Mandell and D. Samborsky, "Fracture of Skin/Stiffener Intersections in Composite Wind Turbine Structures," *1998 ASME Wind Energy Symposium*, AIAA/ASME, W. Musial and D.E. Berg, eds., 1998, p. 334.

148. Mandell, J.F., D.D. Samborsky, D.W. Combs, M.E. Scott and D.S. Cairns, *Fatigue of Composite Material Beam Elements Representative of Wind Turbine Blade Substructure*, NREL/SR-500-24379, National Renewable Energy Laboratory, Golden, CO, 1998.

149. Bach, P.W., *Fatigue of Stud Joints for GFRP Wind Turbine Blades*, ECN-C95-117, ECN, Petten, the Netherlands, 1995.

150. De Bruijn, J.C.M., J.A. ter Laak and C.A.M. van den ENDE, "EN-WISPER," *Proceedings of the IEA Third Symposium of Wind Turbine Fatigue*, IEA, Implementing Agreement for a Programme of Research and Development on Wind Energy Conversion Systems - Annex XI, 1994, pp. 55.

151. De Bruijn, J.C.M., *EN-WISPER: Environmental Influence on the Fatigue Behavior of Wind Turbine Rotor Blades*, 50950-KIM 95-9313, KEMA, Arnhem, 1995.

152. Mandell, J.F., Montana State University, Bozeman, personal communication to the author.

153. Joosse, P.A., "EN-WISPER: Research Overview and Consequences," *Proceedings of the IEA Third Symposium of Wind Turbine Fatigue*, IEA, Implementing Agreement for a Programme of Research and Development on Wind Energy Conversion Systems - Annex XI, 1996, p. 87.

154. Joose, P.A. and D.R.V. van Delft, "Has Fatigue Become a Wearisome Subject?," *Proceeding of the European Union Wind Energy Conference*, Göteborg, Sweden, 1996, p. 902.

155. Rohatgi, J.S., and V. Nelson, *Wind Characteristics: An Analysis for the Generation of Wind Power*, Alternative Energy Institute, West Texas A&M University, Canyon, TX, 1994.

156. Elliott, D.L., et al., *Wind Energy Resource Atlas of the United States*, DOE/CH 10093-4, SERI, Golden, CO, 1987.

157. Schwartz, M.N. and D.L. Elliott, "Mexico Wind Resource Assessment Project," *Proceedings of Windpower '95*, AWEA, Washington, DC, 1995, p. 56.

158. Mouzakis, F., E. Morfiadakis and P. Dellaportas, "Fatigue Loading Parameters Identification of a Wind Turbine Operating in Complex Terrain," submitted for publication.

159. Mouzakis, F., E. Morfiadakis and A. Fragoulis, *Mounturb Final Report*, Contract No. JOU2-CT93-0378, Center for Renewable Energy Sources, Pikermi, Greece, 1996.

160. Fragoulis, A.N., “The Complex Terrain Wind Environment and Its Effects on the Power Output and Loading of Wind Turbines,” *1997 ASME Wind Energy Symposium*, AIAA/ASME, W. Musial and D.E. Berg, eds., 1997, p. 33.

161. Voutsinas, S., V. Riziotis and P. Chaviaropoulos, “Non-Linear Aerodynamics and Fatigue Loading on Wind Turbines,” *1997 ASME Wind Energy Symposium*, AIAA/ASME, W. Musial and D.E. Berg, eds., 1997, p. 41.

162. Veers, P.S., C.H. Lange and S.R. Winterstein, “FAROW*:* A Tool for Fatigue and Reliability of Wind Turbines,” *Proceedings of Windpower ’93*, AWEA, Washington, DC, 1993, p. 342.

163. Veers, P.S., S.R. Winterstein, C.H. Lange and T.A. Wilson, *FAROW: Fatigue and Reliability of Wind Turbine Components*, SAND94-2460, Sandia National Laboratories, Albuquerque, NM, 1994.

164. Ashwill, T.D., and N. Slack, “Fatigue Life Prediction for Vertical Axis Wind Turbine Blades Using the LIFE Computer Program,” Internal Memorandum, Sandia National Laboratories, Albuquerque, NM, 1986.

165. Akins, R.E., *Initial Analysis of Structural Data: DAF 6400 Rotor*, Washington and Lee University, Lexington, 1985.

166. Malcolm, D.J., *Fatigue Life Assessment of VAWT Components*, Indal Technologies, Mississauga, 1985.

167. Sutherland, H.J., T.D. Ashwill and N. Slack, *The LIFE Computer Code Fatigue Life Prediction for Vertical Axis Wind Turbine Components*, SAND87-0792, Sandia National Laboratories, Albuquerque, NM, 1987.

168. Sutherland, H.J., and T. D. Ashwill, “Fatigue Life Prediction for VAWT Components Using the LIFE Codes,” *Sixth ASME Wind Energy Symposium*, R.W. Thresher, ed., SED-Vol. 3, ASME, 1987, p. 193.

169. Sutherland, H. J., T. D. Ashwill, and K. A. Naassan, “Fatigue Analysis Codes for WECS Components,” *Proceedings of Wind Power '87*, SERI/CP-217-3315, AWEA, Washington, DC, 1987, p. 74.

170. Schluter, L.L., and H.J. Sutherland, *Reference Manual for the LIFE2 Computer Code*, SAND89-1396, Sandia National Laboratories, Albuquerque, NM, 1989.

171. Sutherland, H.J., *Analytical Framework for the LIFE2 Computer Code*, SAND89-1397, Sandia National Laboratories, Albuquerque, NM, 1989.

172. Schluter, L.L., and H.J. Sutherland, *User's Guide for LIFE2's Rainflow Counting Algorithm*, SAND90-2259, Sandia National Laboratories, Albuquerque, NM, 1991.

173. Schluter, L.L., *Programmer's Guide for LIFE2's Rainflow Counting Algorithm*, SAND90-2260, Sandia National Laboratories, Albuquerque, NM, 1991.

174. Sutherland, H.J., and R.L. Linker, *User's Guide for the Frequency Domain Algorithms in the LIFE2 Fatigue Analysis Code*, SAND93-1900, Sandia National Laboratories, Albuquerque, NM, 1993.

175. Sutherland, H.J., and T. Wilson, *A Generalized Curve Fitting Technique for the LIFE2 Fatigue Analysis Code*, Sandia National Laboratories, Albuquerque, NM, SAND96-1992, 1996.

176. McNerney, G.M., *Vertical-Axis Wind Turbine Control Strategies*, SAND81-1156, Sandia National Laboratories, Albuquerque, NM, 1981.

177. Vachon, W.A., *A Design Code to Study Vertical-Axis Wind Turbine Control Strategies*, SAND87-7012, Sandia National Laboratories, Albuquerque, NM, 1987.

178. Vachon, W.A., "The Effects of Control Algorithms on Fatigue Life and Energy Production of Vertical Axis Wind Turbines," *Seventh ASME Wind Energy Symposium*, A.H.P. Swift and R.W. Thresher, eds., SED-Vol. 5, ASME, 1988, p. 149.

179. Vachon, W.A., *Control Algorithms for Effective Operation of Variable-Speed Wind Turbines*, SAND90-7112, Sandia National Laboratories, Albuquerque, NM, 1993.

180. Vachon, W.A., "The Effect of Controls on Life and Energy Production of the 34-m VAWT Test Bed," *Eighth ASME Wind Energy Symposium*, D.E. Berg and P.C. Klimas, eds., SED-Vol. 7, ASME, 1989, p. 209.

181. Vachon, W.A. "Smart Control Algorithms for Operation of Variable-Speed Wind Turbines," *Ninth ASME Wind Energy Symposium*, D. E. Berg, ed., SED-Vol. 9, ASME, 1990, p. 191.

182. Vachon, W.A., "Control of Variable-Speed Wind Turbines," *Tenth ASME Wind Energy Symposium*, D.E. Berg and P.S. Veers, eds., SED-Vol. 11, ASME, 1991, p. 73.

183. McNerney, G.M. and P.S. Veers, *A Markov Method for Simulating Non-Gaussian Wind Speed Time Series*, SAND84-1227, Sandia National Laboratories, Albuquerque, NM, 1985.

184. Seebregts, A. J., L.W.M.M. Rademakers, and B.A. Van Den Horn, *Reliability Analysis in Wind Turbine Engineering*, ECN-RX--93-103, Netherlands Energy Research Foundation (ECN), Petten, 1993.

185. Rademakers, L.W.M.M., B.A. Blok, B.A. Van Den Horn, J.N.T. Jehee, A.J. Seebregts and R.W. Van Otterloo, *Reliability Analysis Methods for Wind Turbines, Task 1 of the project: Probabilistic Safety Assessment for Wind Turbines*, ECN-C--92-018, Netherlands Energy Research Foundation (ECN), Petten, 1992.

186. Ronald, K.O., J. Wedel-Heinen, C.J. Christensen and E. Jorgensen, "Reliability-Based Calibration of Partial Safety Factors for Design of Wind-Turbine Rotor Blades Against Fatigue," *Proc. of the 5th European Wind Energy Conf.*, Vol II, DNV and Risoe, 1994, pp. 927.

187. Braam, H., *PRODETO Computer Program, User's Manual*, ECN-C-97-096, Netherlands Energy Research Foundation (ECN), Petten, 1997.

188. Veers, P.S., "Fatigue Reliability of Wind Turbine Fleets: The Effect of Uncertainty on Projected Costs," *Journal of Solar Engineering*, Vol. 118, 1996, p.222.

189. *Adhesives and Sealants, Engineered Materials Handbook*, Vol. 3, ASM, H.F. Brinson, Tech. Chair., Materials Park, OH, 1990.

190. Adams, R.D. and W.C. Wake, *Structural Adhesive Joints in Engineering*, Elsevier, London, 1984.

191. DeLollis, N.J., *Adhesives, Adherends, Adhesion*, Robert E. Krieger, Florida, 1985.

192. Kinloch, A.J., ed., *Developments in Adhesives - 2*, Applied Science Publishers, London, 1981.

193. Schwartz, M.M., *Joining of Composite Matrix Materials*, ASM, Materials Park, OH, 1995.

194. Goland, M., and Reissner, E., "The Stresses in Cemented Joints", *J. Applied Mechanics, Trans. ASME*, 1944, A17.

195. Carpenter, W.C., and G.C. Patton, "Comparison of the Maximum Stress and the Stress Intensity Approaches in the Analysis of Bonded Joints," *Advances in Adhesively Bonded Joints*, ASME, Mall, Liechti, and Vinson, eds., 1988, p. 23.

196. Habib, M., S. Aivazzadeh and G. Verchery, "Analysis of Adhesively Bonded Composite Tubes Under Different Loading Conditions Using Axisymmetric Interface Finite Elements," *Advances in Adhesively Bonded Joints*, ASME, Mall, Liechti, and Vinson, eds., 1988, p. 33.

197. Reedy, E.D., Jr. and T.R. Guess, "Tubular Lap Joints for Wind Turbine Applications: Test and Analysis," *Tenth ASME Wind Energy Symposium*, D.E. Berg and P.S. Veers, eds., SED-Vol. 11, ASME, 1991, p. 47.

198. Reedy, E.D., Jr. and T.R. Guess, "Composite-to-Metal Tubular Lap Joints*:* Strength and Fatigue Resistance," *Int. J. of Fracture*, Vol. 63, 1993, p. 351.

199. Guess, T.R., E.D. Reedy, Jr. And M.E. Stavig, *Mechanical Properties of Hysol EA-9394 Structural Adhesive*, SAND95-0229, Sandia National Laboratories, Albuquerque, 1995.

200. Guess, T,R,, E.D. Reedy, Jr. And A.M. Salvin, "Testing Composite-to-Metal Tubular Lap Joints," *Journal of Composites Technology & Research*, Vol. 17, No. 2, 1995, p. 117.

201. Metzinger, K.E., and T.R. Guess, "Analysis and Testing of Adhesively Bonded Lap Joints," *Wind Energy: Energy Week*, ASME/API, 1996, p. 52.

202. Metzinger, K.E., and T.R. Guess, "How Geometric Details Can Affect the Strength of Adhesive Lap Joints," *1997 ASME Wind Energy Symposium*, W. Musial and D.E. Berg, eds., AIAA/ASME, 1997, p. 209.

203. Metzinger, K.E., and T.R. Guess, "Single-Cycle and Fatigue Strengths of Adhesively Bonded Lap Joints," *1998 ASME Wind Energy Symposium*, AIAA/ASME, W. Musial and D.E. Berg, eds., 1998, p. 344.

204. Faddoul, J.R., *Improved Stud Configurations for Attaching Laminated Wood Wind Turbine Blades*, DOE/NASA/20320-66, NASA TM 87109, 1985.

205. Kinloch, A.J., *Developments in Adhesives – 2*, Applied Science Publishers, 1981.

206. Lamble, J.H., *Principles and Practice of Non-destructive Testing*, Wiley, 1963.

207. McGonnagle, W.J., *Nondestructive Testing*, Second Edition, Gordon and Breach, 1969.

208. Gieske, J.H., and M.A. Rumsey, "Nondestructive Evaluation (NDE) of Composite/Metal Bond Interface of a Wind Turbine Blade Using an Acousto-Ultrasonic Technique," 1997 ASME Wind Energy Symposium, W. Musial and D.E. Berg, eds., AIAA/ASME, 1997, p. 249.

209. Sutherland, H.J., and W. Musial, "The Application of Nondestructive Techniques to the Testing of a Wind Turbine Blade," *Proceedings of WindPower '93*, AWEA, Washington, DC, 1993, pp. 350.

210. Beattie, A.G., "Acoustic Emission Monitoring of a Wind Turbine Blade during a Fatigue Test," *1997 ASME Wind Energy Symposium*, W. Musial and D.E. Berg, eds., AIAA/ASME, 1997, p. 239.

211. *Nondestructive Testing Handbook*, Vol. 7: Ultrasonic Testing, 2nt ed., A.S. Birks, and R.E. Green, Jr., eds., American Society of NonDestructive Testing, 1991.

212. H. J. Sutherland, A. Beattie, B. Hansche, W. Musial, J. Allread, J. Johnson and M. Summers, *The Application of Non-Destructive Techniques to the Testing of a Wind Turbine Blade*, SAND93-1380, Sandia National Laboratories, Albuquerque, NM, June 1994.

213. Wei, J., C. Dou, and F. Stoddard, "Fatigue Damage and Failure Modes Detection of Composite Material by Using Acoustic Emission," *Wind Energy - 1993*, S. Hock, ed., SED-Vol. 14, ASME, 1993, p. 207.

214. Gieske, J., and R. Rumsey, "Nondestructive Evaluation (NDE) of Composite/Metal Bond Interface of a Wind Turbine Blade Using an Acousto-Ultrasonic Technique," *1997 ASME Wind Energy Symposium*, AIAA/ASME, W. Musial and D.E. Berg, eds., 1997, p. 249.

215. Rumsey, M., J. Hurtado, B. Hansche, T. Simmermacher, T. Carne and E. Gross, "In-Field Use of Laser Doppler Vibrometer on a Wind Turbine Blade," *1998 ASME Wind Energy Symposium*, AIAA/ASME, W. Musial and D.E. Berg, eds., 1998, p. 212.

216. Musial, W., and J. Allread, "Test Methodology and Control of Full-Scale Fatigue Tests on Wind Turbine Blades," *Wind Energy - 1993*, S. Hock, ed., SED-Vol. 14, ASME, 1993, p. 199.

217. *Full-Scale Structural Testing of Rotor Blades for WTGS's*, IEC-61400-23, prepared by IEC-TC88-WG8, Revision 11.1, 1998.

218. Wirsching, P.H., "Reliability Methods in Mechanical and Structural Design," University of Arizona, Tucson, 1983.

219. Ashwill, T.D. and P.S. Veers, "Structural Response Measurements and Predictions for the Sandia 34-Meter Test Bed," *Ninth ASME Wind Energy Symposium*, SED-Vol. 9, ASME, 1990, pp. 137.

220. *Selected Papers on Wind Energy Technology, January 1989-January 1990*, P. S. Veers, ed., SAND90-1615, Sandia National Laboratories, Albuquerque, NM, 1990.

11. APPENDICES

Appendix A The Weibull Distribution

The Weibull distribution, see Ref. [218], has been used extensively in this report to describe various physical phenomenologies. A discussion of this distribution is included here for completeness.

A.1. Generalized Distribution

The generalized Weibull distribution is given by:

$$p_x = \left[\frac{a}{b}\right]\left[\frac{x}{b}\right]^{a-1} \exp\left\{-\left[\frac{x}{b}\right]^{a}\right\} \quad , \quad (a > 0,\ b > 0,\ x > 0) \quad , \tag{A-1}$$

where p_X is the probability density function for the variable x, and α and β are the shape factor and the amplitude factor of the distribution, respectively. The equivalent expression for the cumulative density function, CDF, of the Weibull distribution is given by:

$$CDF = 1 - \exp\left[-\left(\frac{x}{b}\right)^{a}\right] \quad . \tag{A-2}$$

In this formulation, the average value of x, $\bar{x}$, is given in terms of the Weibull parameters by:

$$\bar{x} = b\ \Gamma\left[1 + \frac{1}{a}\right] \quad , \tag{A-3}$$

where $\Gamma[\bullet]$ is the gamma function. The standard deviation $\sigma(x)$ of this distribution, cited in Eq. 22, is related to β through the relationship:

$$s(x) = \bar{x}\left[\frac{\Gamma\left(\frac{2}{a} + 1\right)}{\Gamma^2\left(\frac{1}{a} + 1\right)} - 1\right]^{1/2} \quad . \tag{A-4}$$

And, the coefficient-of-variation (COV) is given by:

$$\begin{aligned} COV &= \frac{\sigma(x)}{\bar{x}} \\ &\cong \frac{1}{\alpha} \quad \text{for } \frac{1}{2} < \alpha < 2 \end{aligned} \quad . \tag{A-5}$$

The shape of these distributions for various values of α are given in Fig. 43. In this figure, the x parameter has been replaced with a wind speed parameter and β has been normalized to a value of one.

A.2. Special Distributions

The generalized Weibull distribution contains several named distributions. Of particular importance to this discussion are the Rayleigh and the exponential distributions.

A.2.1. Rayleigh

For the special case of a Rayleigh distribution, the shape factor α equals two. Thus, Eq. 1 takes the form:

$$p_x = \left[\frac{2\,x}{b^2}\right] \exp\left\{-\left[\frac{x}{b}\right]^2\right\} \quad , \quad (b > 0,\ x > 0) \quad , \tag{A-6}$$

and Eq. 2 becomes:

$$CDF = 1 - \exp\left[-\left(\frac{x}{b}\right)^2\right] \quad . \tag{A-7}$$

The average value of x reduces to:

$$\bar{x} = b\ \Gamma\left[\frac{3}{2}\right] = (0.8862...)\ b \quad , \tag{A-8}$$

and the standard deviation reduces to:

$$s(x) = \bar{x}\left[\frac{\Gamma(2)}{\Gamma^2\left(\frac{3}{2}\right)} - 1\right]^{1/2} = (0.4632...)b \quad , \tag{A-9}$$

and the COV becomes a constant:

$$\begin{aligned} COV &= \frac{\sigma(x)}{\bar{x}} = \frac{(0.4632\ ...)\ \beta}{(0.8862\ ...)\ \beta} = 0.522... \\ &\cong \frac{1}{\alpha} = \frac{1}{2} \end{aligned} \quad . \tag{A-10}$$

As noted in this equation, the approximation for the COV given in Eq. 5 holds even at the end of the defined range.

A.2.2. Exponential

For the special case of an exponential distribution, the shape factor α equals one. And, in common notation, the parameter $(1/\beta)$ is called λ. Thus, Eq. 1 takes the form:

$$p_x = \left[\frac{1}{b}\right] \exp\left\{-\left[\frac{x}{b}\right]\right\} = l \exp\{-lx\} \quad , \quad (b > 0,\ x > 0) \quad , \tag{A-11}$$

and Eq. 2 becomes:

$$CDF = 1 - \exp\left[-\left(\frac{x}{b}\right)\right] = 1 - \exp[-lx] \quad . \tag{A-12}$$

The average value of x reduces to:

$$\bar{x} = b\ \Gamma[2] = b = 1/l \quad , \tag{A-13}$$

the standard deviation to:

$$s(x) = \bar{x}\left[\frac{\Gamma(3)}{\Gamma^2(2)} - 1\right]^{1/2} = \bar{x} = b = 1/l \quad , \tag{A-14}$$

and the COV to:

$$\text{COV} = \frac{1}{\alpha} = 1 \quad .$$

A.3. Time Series Relationships

As used in section 4.3.1 “Narrow-Band Gaussian Formulation” on p. 19, the Weibull distribution is used to represent the distribution of the peaks and valleys in a time series. The standard deviation σ of the time series, easily deduced from the time series, is not equal to the standard deviation of the distribution $\sigma(x)$. Unfortunately, a direct relationship between the two for the generalized Weibull distribution does not exist. However, this relationship can be approximated for the standard Weibull distribution.

For a Weibull distribution, β can be approximately by:

$$b = \sqrt{2}\ s \quad , \tag{A-15}$$

$$\bar{x} = (0.8862...)\, b = (0.8862...)\left(\sqrt{2}\, s\right) = (1.2533...)\, s \quad , \tag{A-16}$$

and

$$s(x) = (0.4632...)\, b = (0.4632...)\left(\sqrt{2}\, s\right) = (0.6551...)\, s \quad . \tag{A-17}$$

Appendix B Turbine Data

The data and analysis of several turbines are reported throughout this report. Rather than describe each turbine within the report, a thumbnail description and appropriate references are provided here.

B.1. Sandia/DOE 34-m VAWT Test Bed

The Test Bed (see Fig. 61) is a 34-meter diameter VAWT erected by Sandia National Laboratories near Bushland, Texas (just west of Amarillo) for research purposes. The turbine has a nominal power rating of 500 kW electric with a peak power rating of 625 kW. The generator's torque, and thus speed, is controlled by a load-commutated-inverter (LCI) variable speed motor drive. The LCI connects the turbine to the utility system by converting the variable voltage and frequency of the generator to the constant voltage and frequency of the utility system. The turbine is operated over a speed range from 18 to 39 rpm. The turbine's two blades incorporate variable chord and variable section profiles, including the first VAWT-specific, natural laminar flow airfoil sections. Each is step-tapered with five sections. They are constructed from extruded 6063-T6 aluminum.

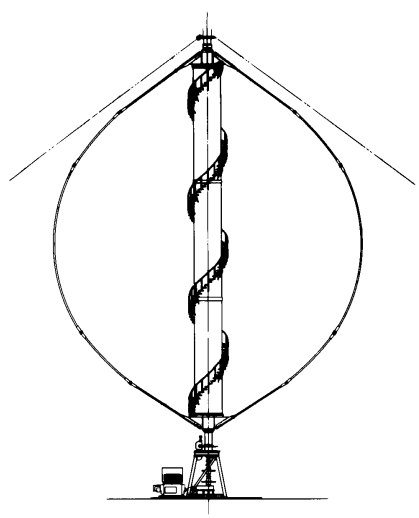

Figure 61. The Sandia 34-m Test Bed Turbine.

The turbine and site have been equipped with a large array of sensors that permit the characterization of the turbine under field conditions [39, 56, 219, 220]. The extensive experimental database allows us to illustrate the fatigue analysis of a wind turbine component and to examine the sensitivity of lifetime predictions to various estimates of the input data.

B.2. Northern Power Systems 100kW Turbine

The Northern Power Systems (NPS) 100-kW turbine is a horizontal-axis turbine, see Figure 62. The turbine is a two-bladed, upwind, teetering hub design utilizing full-span hydraulic passive pitch control. The fiberglass blades, including the elastomeric teetering hub, span 17.8 meters (rotor diameter). The rotor's low speed shaft turns a two-stage, two-speed gearbox. The high-

speed shaft of the gearbox is connected to one of two fully enclosed induction generators. Its 100-kW generator is rated at full power when rotating at 71.8 rpm in a 14 m/s wind.

Several of these turbines were erected and tested, under the auspices of the NREL Cooperative Research Program, in Altamont Pass, California in 1988 [32]. The test program produced an extensive data set for this turbine. Several turbine configurations were tested. For the data set discussed above, the turbine configuration was "locked yaw" (stiff spring) and "free teeter" with damping and stiffness elements. During this data collection period, the turbine was operated continuously at approximately 71.6 rpm.

B.3. Micon

The Micon 65/13 turbine is a horizontal axis turbine. It is a three-bladed, up-wind fixed-pitch turbine. Its rotor diameter is 16 m with a hub height of 23 m. The blades turn a parallel shaft, 3-stage gearbox with a 25:1 gear ratio. The turbine has two generators: a 65 kW generator and a 13 kW generator. The 65 kW generator is the main generator. It reaches full power in a 15 m/s wind. Rotor speed is 48 rpm. The 13 kW generator is only used for low wind-speed operation.

The data sets for this turbine were obtained from two turbines located in a wind farm in San Gorgonio, CA [91, 92]. Both turbines were located in Row 37 of the wind farm. The first turbine was fitted with standard 7.4 m blades (Aerostar) and the second was fitted with special 7.9 m blades. The former design used conventional airfoils while the latter used SERI thin airfoils specially designed for this turbine.

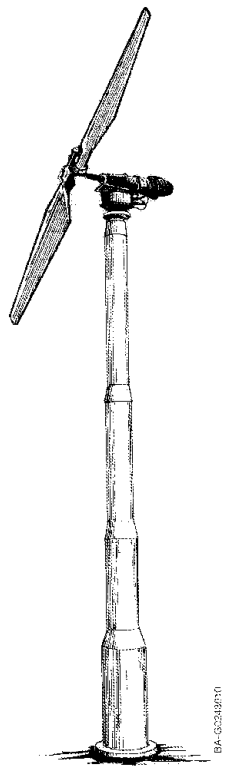

Figure 62. The Northern Power Systems 100 kW Turbine.

DISTRIBUTION:

R. E. Akins
Washington & Lee University
P.O. Box 735
Lexington, VA 24450

H. Ashley
Dept. of Aeronautics and
Astronautics Mechanical Engr.
Stanford University
Stanford, CA 94305

B. Bell
Zond Energy Systems, Inc.
13681 Chantico Rd.
Tehachapi, CA 93561

K. Bergey
University of Oklahoma
Aero Engineering Department
Norman, OK 73069

G. Bir
NREL/NWTC
1617 Cole Boulevard
Golden, CO 80401

M. Buhl
NREL/NWTC
1617 Cole Boulevard
Golden, CO 80401

C. P. Butterfield
NREL/NWTC
1617 Cole Boulevard
Golden, CO 80401

G. Bywaters
Northern Power Technology Co.
Box 999
Waitsfield, VT 05673

J. Cadogan
Office of Photovoltaic & Wind
Technologies, EE-11
U.S. Dept. of Energy
1000 Independence Avenue, SW
Washington, DC 20585

D. Cairns
Montana State University
Dept. of Mechanical & Industrial Engr.
Roberts Hall
Boseman, MT 59717

Stan Calvert
Office of Photovoltaic & Wind
Technologies, EE-11
U.S. Dept. of Energy
1000 Independence Avenue, SW
Washington, DC 20585

P. Carlin
NREL/NWTC
1617 Cole Boulevard
Golden, CO 80401

J. Chapman
OEM Development Corp.
840 Summer St.
Boston, MA 02127-1533

M.C. Chaney
PS Enterprises
Box 837
Glastonbury, CT 06033

R.N. Clark
USDA
Agricultural Research Service
P.O. Drawer 10
Bushland, TX 79012

J. Cohen
Princeton Economic Research
1700 Rockville Pike
Suite 550
Rockville, MD 20852

C. Coleman
Northern Power Technology Co.
Box 999
Waitsfield, VT 05673

K. J. Deering
The Wind Turbine Company
515 116th Avenue NE
No. 263
Bellevue, WA 98004

A.J. Eggers, Jr.
RANN, Inc.
Suite 26
744 San Antonio Rd.
Palo Alto, CA 94303

D. M. Eggleston
DME Engineering
1605 W. Tennessee Ave.
Midland, TX 79701-6083

E. Eggleston
USDA
Agricultural Research Service
P.O. Drawer 10
Bushland, TX 79012

P. R. Goldman
Acting Deputy Director
Office of Photovoltaic & Wind Technologies, EE-11
U.S. Dept. of Energy
1000 Independence Avenue, SW
Washington, DC 20585

G. Gregorek
Aeronautical & Astronautical Dept.
Ohio State University
2300 West Case Road
Columbus, OH 43220

C. Hansen
University of Utah
Department of Mechanical Engineering
Salt Lake City, UT 84112

L. Helling
Librarian
National Atomic Museum
Albuquerque, NM 87185

S. Hock
Wind Energy Program
NREL/NWTC
1617 Cole Boulevard
Golden, CO 80401

W. E. Holley
3731 Oak Brook Court
Pleasanton, CA 94588

K. Jackson
Dynamic Design
123 C Street
Davis, CA 95616

G. James
Mechanical Engineering Department
University of Houston
4800 Calhoun
Houston, TX 77204-4792

J. Johnson
NREL/NWTC
1617 Cole Boulevard
Golden, CO 80401

N. Kelley
NREL/NWTC
1617 Cole Boulevard
Golden, CO 80401

D. Laino
University of Utah
Dept. of Mechanical Engineering
50 S. Central Campus Dr., Rm 2202
Salt Lake City, UT 84112

R. Lynette
Springtyme Co.
212 Jamestown Beach Lane
Sequim, WA 98382

D. Malcolm
Kamzin Technology Inc.
425 Pontius Avenue North
Suite 150
Seattle, WA 98109

J. F. Mandell (5)
Montana State University
302 Cableigh Hall
Bozeman, MT 59717

J.F. Manwell
University of Massachusetts
Renewable Energy Research Laboratory
E Lab Bldg., Dept. of Mechanical Engr.
Amherst, MA 01003

R. N. Meroney
Dept. of Civil Engineering
Colorado State University
Fort Collins, CO 80521

P. Migliore
NREL/NWTC
1617 Cole Boulevard
Golden, CO 80401

A. Mikhail
Zond Energy Systems, Inc.
13681 Chantico Rd.
Tehachapi, CA 93561

L. Miles
The Wind Turbine Company
515 116th Ave., NE
Suite 263
Bellevue, WA 98004

R. H. Monroe
Gougeon Brothers
100 Patterson Avenue
Bay City, MI 48706

W. Musial
NREL/NWTC
1617 Cole Boulevard
Golden, CO 80401

NWTC Library
NREL/NWTC
1617 Cole Boulevard
Golden, CO 80401

V. Nelson
Department of Physics
West Texas A&M University
WT Box 60248
Canyon, TX 79016

G. Nix
NREL/NWTC
1617 Cole Boulevard
Golden, CO 80401

J. W. Oler
Mechanical Engineering Dept.
Texas Tech University
P.O. Box 4289
Lubbock, TX 79409

Tim Olsen
Tim Olsen Consulting
1428 S. Humboldt St.
Denver, CO 80210

D. Ong
Dept. of Aeronautics & Astronautics
Stanford University
98D Escondido Village
Palo Alto, CA 94305

R. Osgood
NREL/NWTC
1617 Cole Boulevard
Golden, CO 80401

R. Poore
Kamzin Technology Inc.
425 Pontius Avenue North
Suite 150
Seattle, WA 98109

R. G. Rajagopalan
Aerospace Engineering Department
Iowa State University
404 Town Engineering Bldg.
Ames, IA 50011

J. Richmond
3368 Mountain Trail Ave.
Newbury Park, CA 91320

M. Robinson
NREL/NWTC
1617 Cole Boulevard
Golden, CO 80401

D.D. Samborsky
Montana State University
c/o Dr. John Mandell
302 Cableigh Hall
Bozeman, MT 59717

W. Sass
Second Wind Inc.
366 Summer St.
Somerville, MA 02144

L. Schienbein
CWT Power
4006 S. Morain Loop
Kennewick, WA 99337

D. Simms
NREL/NWTC
1617 Cole Boulevard
Golden, CO 80401

K. Starcher
AEI
West Texas A&M University
WT Box 60248
Canyon, TX 79016

F. S. Stoddard
P.O. Box 1373
Amherst, MA 01004

R. W. Thresher
NREL/NWTC
1617 Cole Boulevard
Golden, CO 80401

S. Tsai
Stanford University
Dept. of Aeronautics and Astronautics
Durand Bldg.
Stanford, CA 94305-4035

W. A. Vachon
W. A. Vachon & Associates
P.O. Box 149
Manchester, MA 01944

B. Vick
USDA, Agricultural Research Service
P.O. Drawer 10
Bushland, TX 79012

J. Westergaard
Boreal Enterprises
5902 Seward Park Ave., South
Seattle, WA 98118

R. E. Wilson
Mechanical Engineering Dept.
Oregon State University
Corvallis, OR 97331

S. R. Winterstein
Civil Engineering Department
Stanford University
Stanford, CA 94305

B. Wolff
Renewable Energy Program Manager
Conservation and Renewable Energy System
6918 NE Fourth Plain Boulevard
Suite B
Vancouver, WA 98661

R. Zadoks
University of Texas at El Paso
500 W. University Ave.
Mechanical & Industrial Engr.
El Paso, TX 79968-0521

M. Zuteck
MDZ Consulting
931 Grove Street
Kemah, TX 77565

M. Anderson
Renewable Energy Systems, Ltd.
Beaufort House
23 Grovesnor Road
St. Albans, AL1 3AW
UK

M. P. Ansell
School of Material Science
University of Bath
Claverton Down
Bath BA2 7AY
Avon
ENGLAND

P. W. Bach
Netherlands Energy Research Foundation, ECN
P.O. Box 1
NL-1755 ZG Petten
THE NETHERLANDS

J. Beurskens
Programme Manager for Renewable Energies
Netherlands Energy Research Foundation, ECN
P.O. Box 1
1755 ZG Petten (NH)
THE NETHERLANDS

B. Bulder
Netherlands Energy Research Foundation, ECN
P.O. Box 1
NL-1755 ZG Petten
THE NETHERLANDS

D.R.V. van Delft
Delft University of Technology
Stevin Lab
PO Box 5048
260094 Delft
THE NETHERLANDS

J. B. Dragt
Institute for Wind Energy
Faculty of Civil Engineering
Delft University of Technology
Stevinweg 1
2628 CN Delft
THE NETHERLANDS

R. A. Galbraith
Dept. of Aerospace Engineering
James Watt Building
University of Glasgow
Glasgow G12 8QG
SCOTLAND

A. D. Garrad
Garrad Hassan
9-11 Saint Stephen Street
Bristol BS1 1EE
ENGLAND

P. Joose
Delft University of Technology
Stevin Lab
PO Box 5048
260094 Delft
THE NETHERLANDS

C. Kensche
DLR –Institute of Structures and Design
German Aerosoace Research Establishment
Pfaffenwaldring 38-40
70569 Stuttgart
GERMANY

D. I. Page
Energy Technology Support Unit
B 156.7 Harwell Laboratory
Oxfordshire, OX11 ORA
ENGLAND

T. F. Pedersen
Riso National Laboratory
Postbox 49
DK-4000 Roskilde
DENMARK

M. Pedersen
Technical University of Denmark
Fluid Mechanics Dept.
Building 404
Lundtoftevej 100
DK 2800 Lyngby
DENMARK

H. Petersen
Riso National Laboratory
Postbox 49
DK-4000 Roskilde
DENMARK

P. H. Madsen
Riso National Laboratory
Postbox 49
DK-4000 Roskilde
DENMARK

M. G. Real, President
Alpha Real Ag
Feldeggstrasse 89
CH 8008 Zurich
SWITZERLAND

D. Sharpe
Dept. of Aeronautical Engineering
Queen Mary College
Mile End Road
London, E1 4NS
ENGLAND

D. Taylor
Alternative Energy Group
Walton Hall
Open University
Milton Keynes MK7 6AA
ENGLAND

O. de Vries
National Aerospace Laboratory
Anthony Fokkerweg 2
Amsterdam 1017
THE NETHERLANDS

MS 0437	K. E. Metzinger, 09117
MS 0437	E. D. Reedy, 09117
MS 0439	C. R. Dohrmann, 09234
MS 0439	D. W. Lobitz, 09234
MS 0439	D. R. Martinez, 09234
MS 0443	J. G. Arguello, 09117
MS 0443	H. S. Morgan, 09117
MS 0555	B. Hansche, 09133
MS 0557	T. J. Baca, 09119
MS 0557	T. G. Carne, 09119
MS 0557	J. P. Lauffer, 09119
MS 0557	T. W. Simmermacher, 09119
MS 0615	J. H. Gieske, 09133
MS 0708	H. M. Dodd, 06214 (50)
MS 0708	T. D. Ashwill, 06214
MS 0708	D. E. Berg, 06214
MS 0708	P. L. Jones, 06214
MS 0708	D. L. Laird, 06214
MS 0708	M. A. Rumsey, 06214
MS 0708	H. J. Sutherland, 06214
MS 0708	P. S. Veers, 06214
MS 0708	J. R. Zayas, 06214
MS 0836	G. F. Homicz, 09116
MS 0836	J. H. Strickland, 09116
MS 0836	W. P. Wolfe, 09116
MS 0619	Review & Approval Desk, 00111 For DOE/OSTI
MS 0899	Technical Library, 04916 (2)
MS 9018	Central Technical Files, 08940-2